Modelling Repair Techniques for Reinforced Concrete Bridge Barriers using Glass Fibre Reinforced Polymer Bars

by

Abdullah Al-Jaaidi

A thesis submitted in partial fulfillment of the requirements for the degree of

Master of Science

in

STRUCTURAL ENGINEERING

Department of Civil and Environmental Engineering

University of Alberta

ABSTRACT

In an era where bridge deterioration due to corrosion has become evident and a pressing concern for future reinforced concrete bridge construction, glass fibre reinforced polymer (GFRP) reinforcement has emerged as a feasible alternative to steel due to its superior corrosion resistance. Research on reinforcing bridge decks and barriers with GFRP bars is well established, and design provisions have been incorporated in the latest versions of the Canadian Highway Bridge Design Code (CHBDC). However, the CHBDC does not provide specifications on repairing GFRP reinforced concrete (GFRP-RC) bridge barriers in case of damage caused by vehicle impact. The absence of specifications on GFRP-RC barriers is attributed to lack of research on the topic. Therefore, this thesis aims to assess the feasibility and efficiency of three repair techniques on damaged GFRP-RC bridge barriers to provide guidelines on the subject. To fulfil this objective, this research was divided into two parts, an analytical part and an experimental part. The experimental part presented five full-scale, 1.5-m-wide, single-slope Alberta Transportation (AT) Test Level-4 (TL-4) RC bridge barriers (used in moderate to high traffic volume highways) and consists of five 2.4 x 1.5-metre concrete decks reinforced either with steel or GFRP bars, or hybrid reinforcement of steel and GFRP. Two specimens represent reference barriers to justify the replacement of steel reinforcement with GFRP and to evaluate the repair techniques' efficiency. Three barrier specimens were meant to reflect three scenarios of repairing damaged bridge barriers with GFRP using the doweling repair technique. This thesis summarized the procedure of static testing of bridge barriers under a monotonic load simulating vehicle impact, as specified by the CHBDC, and presented the accomplished groundwork to prepare and construct the barrier specimens and test them in the future. The analytical part of this research presented simulations of different repair techniques and simulations of the five proposed specimens, that are to be tested in

the future, using VecTor2, a finite-element analysis (FEA) software. The analysis results were studied and compared in terms of barrier wall strength, mode of failure, deflections, and rebar strains to evaluate the performance of GFRP-RC barriers and the efficiency of the proposed repair techniques. Reinforcing single-slope AT TL-4 bridge barriers with a GFRP reinforcement ratio equivalent to its steel-reinforced counterpart achieved 70% of the steel counterpart's ultimate load capacity and exceeded the S6:19 strength limit by a ratio of 1.14. Using 20M (#6) GFRP bars instead of 15M (#5) GFRP bars could increase the barrier's restored ultimate load capacity to 92% of its steel counterpart's ultimate load capacity. All repair techniques and scenarios for GFRP reinforced barrier overhangs effectively restored most of the original designs' capacity. Two of the proposed doweling repair techniques for GFRP-RC barriers, namely single-headed GFRP-FRC repair and single-headed GFRP-RC repair, proved to be effective in restoring the barrier ultimate load capacity, and they achieved ultimate load capacities of 101.8% and 96.4%, respectively, of the as-designed barrier strength. Repairing barrier overhangs by doweling regular GFRP reinforcement is also a viable option. In the case of repairing a damaged barrier wall, the restored capacity was 97% of the original, and in the case of repairing damage that extends to the deck slab, full capacity was restored. In addition, a parametric study using VecTor2 was conducted to assess the influence of some parameters (e.g. deck thickness, overhang length, dowelled bar spacing) on the proposed barrier designs and repairs to find optimal design values. The data generated from this parametric study were compared and discussed, and it was concluded that, in general, the proposed designs and repairs were sufficient to resist design loads.

PREFACE

Chapter 3 of this thesis has been published as Aljaaidi, A. and Tomlinson, D. “Assessment of Repair Techniques for GFRP Reinforced Barriers using VecTor2” in the proceedings of the 2019 Canadian Society for Civil Engineering Conference in Laval, Quebec. I was responsible for the model development and analysis as well as the manuscript composition. D. Tomlinson was the supervisory author and was involved with concept formation and manuscript composition.

ACKNOWLEDGEMENTS

The author is tremendously grateful to **GOD ALMIGHTY**, the author of knowledge, wisdom, and all that is good, for without his graces and countless blessings, the author and his work would not have existed.

Sincere appreciation and deepest gratitude for the help, support and guidance are extended to many people who, in one way or another, have contributed in making this thesis possible.

First and foremost, I would like to acknowledge **my parents, my heroes, Gaafar and Jawhara,** whose countless sacrifices and prayers, continuous encouragement, and unconditional love paved the way for me to realize opportunities that may have never otherwise presented themselves. They raised nine bright individuals who became Doctors, Dentists, Engineers, Architects, or Computer Technicians, and upright godly people. They made me the person I am today, and I am forever in their debt and can never repay them.

To **my siblings, Hasan, Husam, Mieshael, Rasha, Muhammad, Ahmed, Omar, and Razan,** I am grateful for your love, encouragement, and belief in me. You are my blood and support system.

To **my niece Reema, the apple of our eyes,** even though you were not near me but indeed, watching videos of you growing up has always lifted my spirits.

To **Sheikh Abdullah Ahmed Bugshan**, the man whose father and himself supported my family and me for decades, thank you from the bottom of my heart. Your debt is one that I might never be able to repay except with prayers. As the Arabic saying goes: "*Do good to people, and you'll enslave their hearts*," and mine is undoubtedly yours.

To **my relatives, cousins, friends, and colleagues,** thank you for your advice, help, and valuable comments. I am grateful to each and every one of you. Thank you for the memories. I do not forget, and like a true Arab, I always pay my debts.

I am grateful to **Hadhramout Establishment for Human Development** for awarding me a full-ride scholarship for my master's Program.

The experimental component of this thesis was funded by the **NSERC Engage program** (EGP 530967-18, "Evaluating Repair Processes for Concrete Bridge Decks and Barriers Reinforced with Glass Fibre Reinforced Polymer Bars") with the in-kind donation of GFRP bars and technical support from **Tuf-Bar** being greatly appreciated. I would also like to thank **Alberta Transportation** for providing feedback on the design of the barriers to better contextualize the

work. My work in the lab could not have been possible without **Greg Miller and Cam West's** help.

Last but not least, to **my supervisor and advisor, Dr. Tomlinson,** thank you for taking a chance on a fresh civil engineering graduate from overseas, from the middle of the Arabian Desert. I am genuinely grateful for your invaluable guidance and mentorship throughout my master's studies. One look at the first research document I shared with you reminds me of how far I have come, and one look at my thesis reminds me of how grateful I am to you.

TABLE OF CONTENTS

LIST OF TABLES

LIST OF FIGURES

1 INTRODUCTION

1.1 BACKGROUND

Corrosion of steel reinforcement is a serious concern that adversely affects the infrastructure in Canada and around the world. A 2005 study estimated the direct cost of corrosion of highway bridges in Canada for that year to be $1.243 billion (Canadian dollars) with $300 million of that attributed to rehabilitating reinforced concrete (RC) bridge decks. The indirect cost (e.g. traffic delays) to users can be ten times that of direct corrosion costs (Shipilov 2009). Corrosion damage is exacerbated in areas exposed to aggressive environmental conditions, such as bridge decks and barriers (El-Salakawy et al. 2004). Not only does corrosion pose financial concerns, but it also poses safety concerns. The structural integrity of infrastructures is compromised by corrosion which leads in some cases to catastrophic failures and fatalities (Shipilov 2009).

Fibre reinforced polymer (FRP) reinforcement, especially Glass Fibre Reinforced Polymer (GFRP) reinforcement, has emerged as an effective solution to the corrosion problem. FRP's superior corrosion resistance lends itself well to infrastructure applications (Ahmed et al. 2011); the validity of replacing conventional steel reinforcement with FRP reinforcement in concrete structures has been established by many researchers (Nanni 1993, Banthia et al. 1995, Seible 1996, Benmokrane et al. 1996). Further laboratory testing and field implementations have demonstrated the feasibility and practicality of using GFRP reinforcement in bridge construction, particularly in bridge decks and barriers (Trejo et al. 2000, Buth et al. 2003, El-Salakawy et al. 2003, El-Salakawy et al. 2004, Matta et al. 2007, Benmokrane et al. 2007). GFRP reinforced concrete (GFRP-RC) performed well in aggressive environments under service conditions where corrosion and durability were major concerns (Mufti et al. 2007). Replacing steel with GFRP rebar has been shown to be a cost-effective solution in the long term (El-Salakawy and Islam 2014).

Bridge barriers are a critical safety feature in highway bridges. In addition to their roles of defining the superstructure edge and reducing the consequences of vehicles leaving the roadway, they protect occupants of colliding vehicles, occupants of other nearby vehicles, and people and property underneath bridges (Mitchell et al. 2006, Buth et al. 2003, AASTHO LRFD 2007). To fulfil this function, barriers must be strong and stiff enough to redirect errant vehicles in the event of a vehicular accident without rollover or excessive rebound across traffic lanes. Thus, bridge barriers are susceptible to both impact damage as well as damage from aggressive environmental conditions.

To validate the replacement of steel rebar with GFRP bars in Canadian barrier designs, El-Salakawy et al. (2003) investigated the response of entirely GFRP-RC bridge barriers. Furthermore, they introduced connection detailing to connect GFRP-RC barrier walls to GFRP-RC bridge deck slabs. This reinforcement configurations for GFRP-RC barriers were later approved by the Ministry of Transportation of Québec (MTQ) and adopted by the Canadian Highway Bridge Design Code (CHBDC) (CSA 2014a). These approved GFRP-RC barrier designs are only applicable to double-slope MTQ barriers, and do not transfer to other barrier shapes used in Canada, such as the single-slope Alberta Transportation (AT) barrier shape. Ahmed et al. (2010) explored using GFRP in single-slope Alberta RC bridge barrier walls with epoxy-coated steel in the deck slab; however, justifying the total replacement of steel with GFRP in such barrier-deck overhangs needs further investigations.

Though steel-RC barriers are subject to both impact and corrosion damage, transportation ministries have well established processes for their repair. These processes are not well established for GFRP-RC barriers. Although GFRP-RC members have superior corrosion resistance compared to steel reinforced ones, they are not immune to localized damage and excessive cracking caused by factors such as vehicle impact. El-Salakawy et al. (2010) and El-Salakawy et al. (2014) explored different options to repair damaged GFRP-RC slabs and barriers. Two repair techniques were conceived from this research. Although these repair techniques are feasible and efficient for GFRP-RC barriers, further testing is required to investigate the efficacy of those repair techniques on different barrier configurations and reinforcement schemes. Moreover, applying these repair techniques in practice on long bridge segments requires considerable time and effort. To address these research gaps, this thesis investigates the replacement of steel with GFRP in single-slope Alberta RC barrier-deck overhangs, the efficiency of using the planting (doweling) repair technique, proposed by El-Salakawy et al. (2014), on single-slope Alberta GFRP-RC barrier-deck overhangs and the feasibility of two new repair techniques for GFRP-RC barriers.

1.2 RESEARCH OBJECTIVE

The objective of this research program is to evaluate the feasibility and structural performance of GFRP-RC bridge barriers, and to investigate the efficiency of different repair techniques on them. To achieve this objective, the following tasks need to be completed:

1. Review literature to understand the current state-of-the-art of GFRP-RC barriers.

2. Assess the structural performance (load capacity, failure mode, etc.) of single-slope test level 4 (TL-4) steel-RC bridge barrier-deck overhangs subjected to equivalent static load simulating vehicle impact.
3. Assess of the structural performance of single-slope test level 4 (TL-4) GFRP-RC bridge barrier-deck overhang subjected to equivalent static load simulating vehicle impact.
4. Compare the performance of GFRP-RC bridge barrier-deck overhangs with their steel counterpart to justify the replacement of steel with GFRP.
5. Assess the efficiency of two repair techniques for single-slope GFRP-RC bridge barriers involving doweled single-headed GFRP bars.
6. Assess the efficiency of applying the planting (doweling) repair technique on single-slope GFRP-RC barrier-deck overhangs.

1.3 RESEARCH SCOPE

A single-slope TL-4 barrier design is considered because of its wide use in bridge construction across Canada. Research outcomes may also be extended to other test levels of barriers with similar designs. Five full-scale 1.5 m wide TL-4 barrier-deck overhang segments were to be constructed as test prototypes. This barrier width does not allow the typical distribution of load in two-way action but is acceptable for evaluating anchorage capacity of barrier reinforcement and for initial tests of barrier-deck overhangs. Prototypes were planned to be tested under monotonic load but instead were modelled and analyzed using VecTor2 (2-D finite element analysis software). Two prototypes address the feasibility of replacing steel with GFRP reinforcement; the other three prototypes investigate the feasibility of the proposed repair technique (doweling technique) in restoring damaged bridge barrier overhangs. Two new repair techniques, focusing on repairs located at the barrier/deck interface using single-headed GFRP bars are presented in this thesis.

1.3.1 COVID-19 impact on the thesis project

Due to the COVID-19 pandemic, all full-scale structural testing facilities at the University of Alberta were shutdown from March to November 2020 which prevented me from completing the experimental program presented in Chapter 4. In lieu of the proposed testing, additional VecTor 2 models were run to simulate the static testing of the five test specimens and complete a parametric study to investigate the effect of design parameters on barrier-deck overhang performance.

1.4 RESEARCH SIGNIFICANCE

Although El-Salakawy et al. (2014)'s work provides a feasible and efficient repair technique, namely the planting (doweling) technique, for GFRP-RC bridge barriers, further testing is required to investigate the efficacy of this repair technique on different barrier configurations and reinforcement schemes, and longer, more realistic overhang lengths (e.g. 1500 mm). Moreover, executing the doweling repair technique in practice for long bridge segments requires considerable time and effort. Therefore, this research aims to address the concerns regarding transferring the doweling repair technique to different barrier designs as well as to propose more efficient repair techniques for GFRP-RC bridge barriers.

1.5 RESEARCH ORGANIZATION

The structure of this research project follows an investigation to assess the replacement of steel rebar with GFRP bars in bridge barrier-deck overhangs, the feasibility of repairing damaged GFRP-RC barrier-deck overhangs using doweling repair techniques, and the feasibility of two new repair techniques for GFRP barrier walls. The contents of the research, by chapter, are listed below:

Chapter 1: Introduction to the research program and outline of objectives and scope.

Chapter 2: A literature review on GFRP-RC bridge barriers/decks, and previous testing done on GFRP-RC bridge barriers and their repair. *Chapter 2 completes Task 1 of the research objective*.

Chapter 3: The first stage of analytical work on the assessment of as-built designs and two new repair techniques for GFRP-RC bridge barriers using finite element analysis in VecTor2. *Chapter 3 addresses part of Task 2, 3, 4 and 5 of the research objective*.

Chapter 4: Two stages of proposed experimental work focusing on the structural performance of steel and GFRP-RC bridge barrier overhangs, and the efficiency of the doweling repair technique with GFRP bars on these designs. Experimental work in this chapter was interrupted by COVID-19, hence a new phase of models were run in Chapter 5 in lieu of testing. *Chapter 4 addresses parts of Task 2, 3, 4 and 6*.

Chapter 5: The second stage of the analytical work on the assessment of as-built designs and doweling repair technique for the bridge barrier overhangs presented in Chapter 4 using VecTor2 software. *Chapter 5 fulfills the analytical part of Tasks 2, 3, 5, and 6 of the research objectives*.

Chapter 6: Conclusions and recommendations from this research program are presented.

2 LITERATURE REVIEW

2.1 CHAPTER INTRODUCTION

Fibre reinforced polymers, especially GFRP, have emerged as an alternative to conventional steel reinforcement in reinforced concrete structures. Due to GFRP's superior corrosion resistance relative to steel, structural performance, and cost effectiveness, it is well-suited for infrastructure applications like bridge decks and barriers (Ahmed et al. 2011, El-Salakawy and Islam 2014). Use of GFRP bars in bridge decks and barriers has significantly increased in Canada in the 21st century (Ahmed et al. 2013). The Canadian Highway Bridge Design Code (CHBDC) (also referred to as CSA S6:19 or CSA S6-14) provides specifications for designing GFRP-RC barriers but does not provide repair or rehabilitation guidelines for GFRP-RC barriers in case of localized damage. This chapter provides a background of research on RC bridge barriers, their testing and repair.

2.2 BRIDGE COMPONENTS

Typically, the superstructure of short to medium span bridges is comprised of decks, barriers, and girders. The deck distributes traffic loads transversely to the girders. The girders then distribute loads longitudinally to the substructure. The substructure consists of elements that support the superstructure (e.g. abutments, piers, bearings, footings and piles) that are outside the scope of this thesis. Components of a typical girder-type bridge are shown in Figure 2.1.

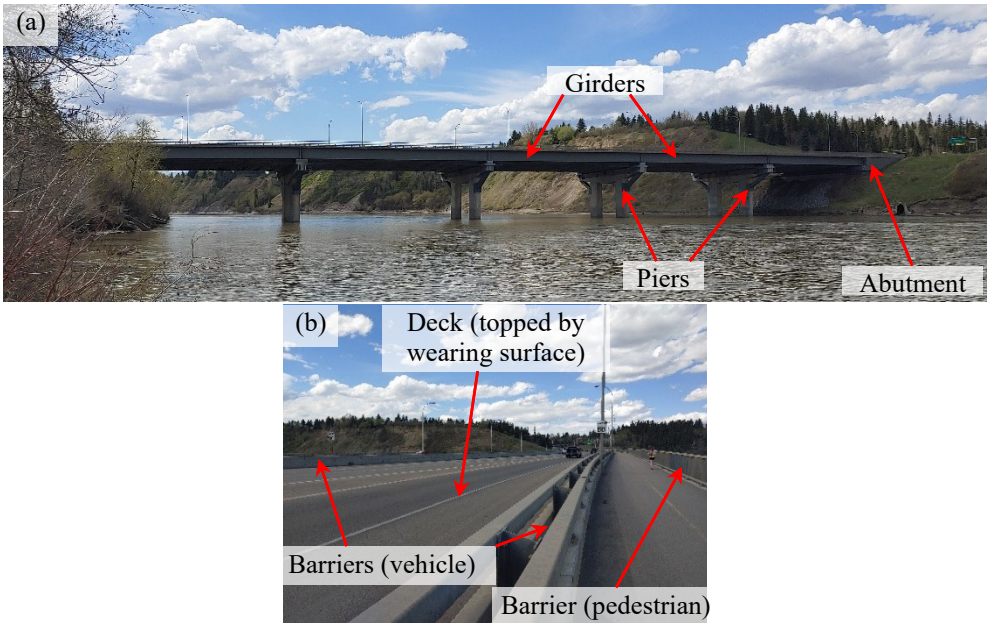

Figure 2.1: Components of a girder-type bridge (Quesnell Bridge, Edmonton, AB) (a) side view and (b) top view showing roadway and shared use path.

Girders in medium span bridges are typically built out of structural steel or prestressed concrete. Girders are usually I-sections such as steel plate girders or prestressed concrete sections (e.g. Nebraska University (NU) girders) or box girders (steel or prestressed concrete) (Figure 2.2). In short (i.e. less than 12 m) span bridges, solid or voided concrete slabs are more economical.

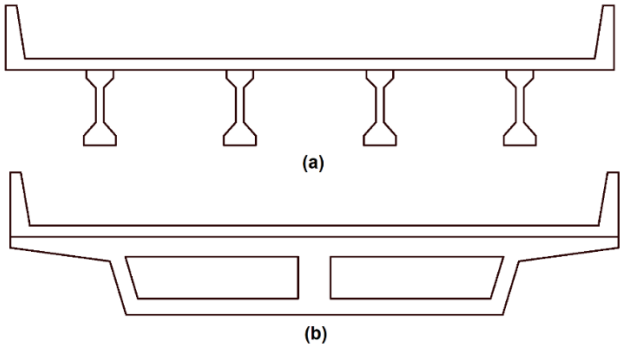

Figure 2.2: Typical reinforced concrete sections in bridge superstructures (a) a slab on I-girder bridge section (b) a slab on two-cell box girder bridge section.

Decks are the structural riding surface of the bridge superstructure that carries and distributes traffic loads (e.g. vehicle wheel loads and barrier impact loads) to the girders. There are many deck types including cast-in-place RC decks, precast concrete deck panels, and steel orthotropic decks. Cast-in-place RC decks are the most common because they are cost effective, have good skid resistance, constructed with readily available materials, and have well-established construction practices (Chen and Duan 2000, CSA 2014a).

The required deck thickness is affected by many factors. Decks and reinforcement must be proportioned to have adequate stiffness to satisfy deflection limits, typically achieved by meeting minimum span/depth ratios for different superstructure systems. In addition, bridge design codes specify minimum concrete cover that ranges from 25 to 100 mm for unprotected reinforcing steel. Cover may be reduced if steel is protected from corrosion or if non-corrosive materials (e.g. stainless steel) are used. The minimum required deck thickness in the CHBDC is controlled by minimum cover requirements (Table 2.1) as well as requirements that the clear distance between the top and bottom transverse reinforcement needs to be at least 55 mm. Decks may be as thin as 170 mm under specific conditions but are typically around 225 mm thick. This thickness is predicated on the assumption of a 90 mm top cover, 15M top and bottom transverse bars, a 55 mm clear distance between them, and a soffit cover of 50 mm (CSA 2014b).

Table 2.1: Minimum concrete covers and tolerances (Reproduced from Table 8.5, CSA 2014a).

Environmental exposure	Component	Reinforcement	Concrete covers and tolerances	
			Cast-in-place concrete, mm	Precast concrete, mm
Deicing chemicals; spray or surface runoff containing deicing chemicals; marine spray	1) Top surface of slab	Steel bars	70 ± 20	55 ± 10
	2) Soffit of slab less than 300 mm thick	Steel bars	50 ± 10	45 ± 10
	3) Soffit of slab 300 mm thick or thicker	Steel bars	60 ± 10	50 ± 10

To take advantage of arching action in suitably confined deck slabs, the CHBDC encourages the use of the empirical design method, which simplifies the design of deck slabs between girders. This method specifies minimum steel reinforcement in two layers, each with an orthogonal pattern of bars with a reinforcement ratio of at least 0.003. Deck slabs designed by the empirical method are not subject to fatigue problems since arching action reduces the stress range in reinforcing bars. This method has is only applicable to portions of the deck bounded by composite girders and does not apply to deck design in bridge overhangs which need to be analyzed for negative transverse moments caused by loads on the barrier/deck overhang. The empirical design method also cannot be used for GFRP-RC decks, mainly because of GFRP's lower elastic modulus.

Traffic barriers define the superstructure edge and reduce the consequences of vehicles leaving the roadway (Mitchell et al. 2006, Buth et al. 2003, AASTHO LRFD 2007). Barriers protect occupants in the colliding vehicle, occupants in other vehicles near the collision location, and people and property underneath the bridge. Barriers are classified based on their function (e.g. traffic, pedestrian, bicycle). Traffic barriers in bridges are the main focus of this thesis.

2.3 TRAFFIC BRIDGE BARRIER TEST LEVELS AND CRASH TESTING GUIDELINES

The main function of traffic barriers is to contain and redirect errant vehicles while preventing rollover and snagging, allowing vehicles to stop relatively close to the impacted section. To achieve this purpose, barriers must be strong and stiff enough to resist impact forces from the vehicle collision. Traffic barriers must be structurally and geometrically crashworthy. A barrier is "crashworthy" if it meets crash test criteria established for that type of barrier (discussed in 2.3.2).

2.3.1 Barrier Shapes

One of the earliest concrete barrier shapes is the GM (General Motors) shape and most concrete barriers in use today were derived from this shape (Rosenbaugh et al. 2007). The GM barrier has

a shallow lower slope and a steep upper slope. During a low angle impact, tires climb the lower slope and redirect the vehicle without any metal contact with the barrier. The upper slope redirects vehicles impacting at higher angles where metal contact is expected.

The GM shape and its descendants, shown in Figure 2.3, are called safety shaped barriers. Through the late 1950's and early 1960's the New Jersey Department of Transportation developed the New Jersey barrier via crash testing (Hellriegel 1968). The lower slope of this barrier allows impact forces to act over the time the vehicle travels over the slope and transversely into the barrier. This extended time results in lower peak impact forces and reduced accelerations for the passengers as opposed to the shorter interval associated with a flat wall (Rosenbaugh et al. 2007). However, tire climb increases the possibility of vehicle rollover at higher impact angles. The F-shape barrier was designed to reduce vehicle climb and rollover as a result of a parametric study on the basic New Jersey shape. Single slope barriers were developed to further increase vehicle stability by eliminating the lower slope of the New Jersey and F-shape barriers. Vehicle stability is greatly improved for single slope barriers compared to two-slope shapes. Single-slope barriers include the California Type 60 barrier and the Texas SSCB. Due to the significant amount of wheel climb and risk of instability problems (i.e. rollover), barriers with vertical faces were developed to improve vehicle stability but these shapes reduce impact time duration leading to larger peak impact forces which lead to increased risk of injury and fatality during impacts (Rosenbaugh et al. 2007).

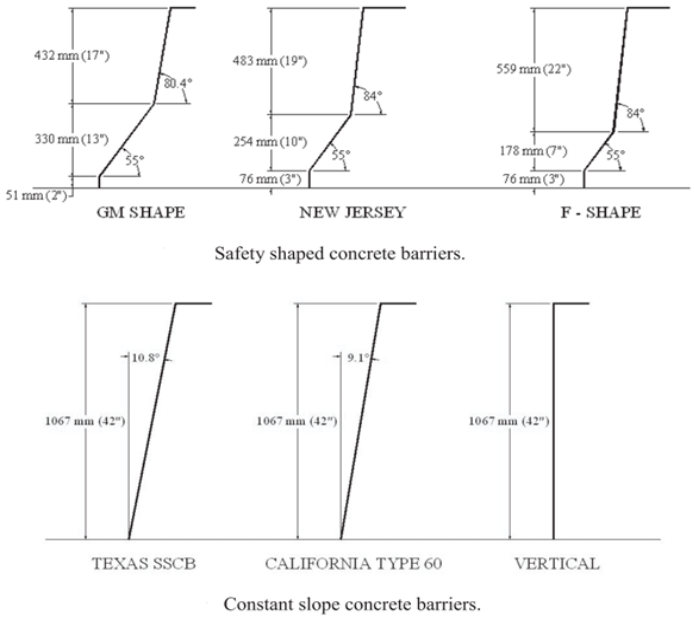

Figure 2.3: Different shapes of concrete barriers (Rosenbaugh et al. 2007).

Each barrier shape has drawbacks. Safety-shaped (i.e. double sloped) barriers and single-sloped barriers induce vehicle climb which leads to vehicle rollover. Vertical barriers prevent vehicle climb but have higher risk of injury and fatality. This thesis considers the single-slope Alberta Transportation Test Level-4 (TL-4) type RC bridge barrier geometry shown in Figure 2.4.

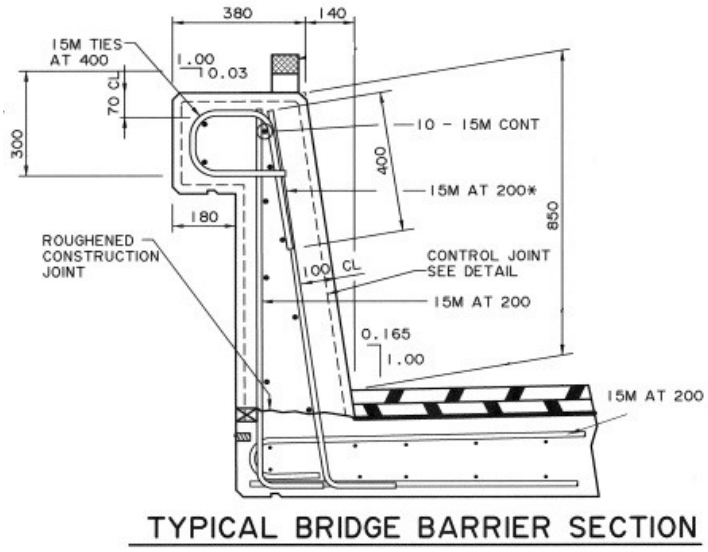

Figure 2.4: Alberta TL-4 design (Alberta Transportation 2017).

2.3.2 Barrier Height

Barriers are built to minimum heights to prevent vehicles from vaulting or rolling over the barrier. The CHBDC height requirements are shown in Table 2.2. Higher performance levels require greater heights due to the higher centre of gravity of test vehicles (CSA 2014a, CSA 2014b).

Table 2.2: Minimum Barrier Height (H) (Reproduced from Table 12.8, CSA 2014a).

Type of barrier	***H*, mm**
Traffic	
TL-1	680
TL-2	680
TL-4	800
TL-5	1050
Combination (pedestrian)	1050
Combination (bicycle)	1370

2.3.3 Barrier test/performance level

The CHBDC uses a procedure based on the AASHTO Guide Specifications for Bridge Railings (AASHTO 1989) to determine barrier requirements. These requirements are based on risk analyses of the frequencies and consequences of vehicle accidents on bridges. These risks are a function of many variables (e.g. traffic lanes, divided or undivided highway, design speed) considered when

evaluating traffic barrier performance. This approach acknowledges that different bridges have different importance and that different performance levels of traffic barriers to match bridge site requirements are needed. For instance, traffic barriers on high-volume highway bridges must be stronger and safer than the ones for low-volume rural bridges. This approach was known as the 'multiple performance level concept' and now called the 'multiple test level concept'. Another aspect involved in this procedure is the required crash-testing of barriers to confirm that they will meet requirements of a specified test level (AASHTO 1989, CSA 2014b).

To aid designers by reducing the potentially infinite numbers of test levels to a manageable amount for practical design, AASHTO (2007) defined six "test levels" presented in the National Cooperative Highway Research Program (NCHRP) Report 350. These levels are based on cost (economic and risk)-benefit analyses of barriers (AASHTO 2007, NCHRP 1993). The six test levels described by AASHTO (2007) range from TL-1 (low speed and traffic volume) to TL-6 (high speed and high centre of mass tanker trucks). CSA S6 (the CHBDC) adopted four of these test levels for traffic barriers in Canada (TL-1, TL-2, TL-4 and TL-5). It is worth mentioning that NCHRP 350 does not provide any guidance on the optimal selection of test level. The optimal level of traffic barrier performance at a bridge site is assumed to be the level giving the least cost (economic as well as the severities of accidents) expected with that traffic barrier (CSA 2014b).

2.3.4 Test Levels and Crash Test Requirements for Barriers

Test levels are defined by criteria including test vehicle's speed, approach angle, and mass. Test levels evaluate crash test performance factors: structural adequacy, occupant risk, and post-impact vehicle behaviour. According to the CHBDC and AASHTO 2007, barriers must meet or exceed crash test requirements of the determined optimum test level along their entire length. (CSA 2014a, AASHTO LRFD 2007); the adequacy of barriers in reducing consequences of vehicle impact is determined from crash tests (CSA 2014b). A barrier is considered to be successfully crash-tested if it protects occupants of the vehicle hitting the barrier, nearby vehicles on the roadway, and people and property under the bridge (NCHRP 1993).

One of two sets of crash test requirements for TL-1, TL-2, TL-4, and TL-5 traffic barriers are required by the CHBDC: the requirements stated in the NCHRP Report 350 (Table 2.3), or similar requirements required by the AASHTO Manual for Assessing Safety Hardware (MASH 2009). The MASH 2009 crash test requirements were developed to modify several test vehicle dimensions and weights to realistically represent traffic mix due to changes in the automobile

industry, and were introduced in the CHBDC as an alternative to the NCHRP 350 crash test requirements rather than a replacement. (MASH 2009, CSA 2014b).

Table 2.3: NCHRP Report 350 crash test requirements (Reproduced from Table C12.1, CSA 2014b).

	Test speeds, km/h			
	NCHRP Report 350 Test vehicle description and impact angles			
	Small automobiles	Pickup truck	Medium single-unit truck	Van-type tractor-trailers
	W = 820 kg	W = 2000 kg	W = 8000 kg	W = 36 000 kg
Performance level	θ = 20°	θ = 25°	θ = 15°	θ = 15°
TL-1	50	50		
TL-2	70	70	80	
TL-4	100	100		80
TL-5	100	100		

Notes:
1) W = mass of impacting vehicle.
2) θ = angle between line of traffic barrier and path of impacting vehicle (impact angle).

The CHBDC allows successfully crash-tested traffic barriers to be changed, given that changes do not adversely affect vehicle-barrier interaction. Hence, the effect of any change on traffic barrier performance should be determined based on a review of the original crash test results as well as on any supporting calculations or component testing required (CSA 2014a, CSA 2014b).

2.3.5 Traffic Barrier Anchorage

Typical barriers are cast-in-place after the deck is constructed. Barriers are connected to deck slabs through anchorage of the reinforcement that passes through the barrier-deck joint. This reinforcement is shown for Alberta Transportation TL-4 barriers in Figure 2.5.

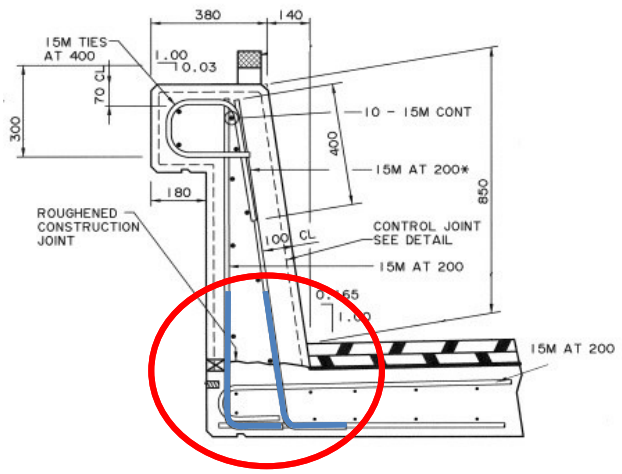

Figure 2.5: Anchorage bars (in blue) used in Alberta TL-4 barrier (Alberta Transportation 2017).

Acceptable anchorage systems must endure crash testing without significant damage to either the anchorage system or deck. In case of the absence of crash testing results of the anchorage, the

anchorage and deck are designed to resist maximum bending, shear, and punching load transmitted to them by the barriers from specified traffic loads. These loads are equivalent static loads applied on the barriers and based on converted vehicular impact load at the specified performance level. These loads are taken from AASHTO LRFD Bridge Specification (AASHTO 1994), and divided by the live load factor of 1.7 and converted into equivalent static loads by a dynamic stress coefficient of 1.4 which reflects the relationship between dynamic and static strength of the components. The equivalent static loads are applied as shown in Figure 2.6, and found in Table 2.4 (CSA 2014a, CSA 2014b).

Table 2.4: Traffic barrier loads (unfactored) (reproduced from Table 3.7, CSA 2014a).

Performance level	Transverse load, kN	Longitudinal load, kN	Vertical load, kN
TL-1	25	10	10
TL-2	50	20	10
TL-4	100	30	30
TL-5	210	70	90

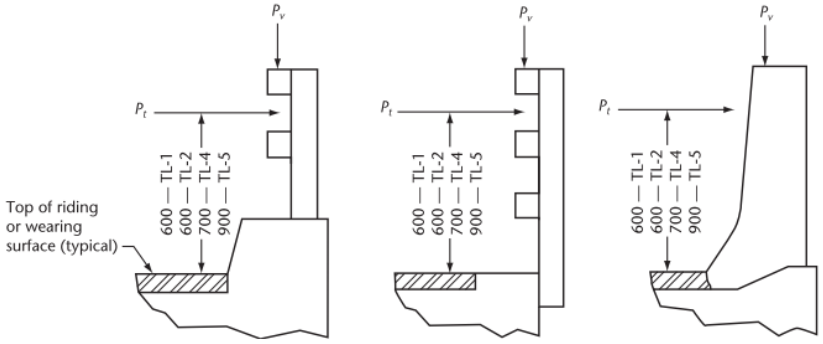

Figure 2.6: Application of traffic design loads to traffic barriers (Reproduced from Figure 12.1, CSA 2014a).

2.4 BRIDGE BARRIER DESIGN METHODOLOGY AND TEST METHODS

Traffic barriers are designed for both geometric and strength requirements. These shapes and barriers were developed then proven by crash testing (Section 2.3.1). Strength requirements depend on anticipated traffic conditions. Test levels are assigned according to the required strength and anticipated traffic condition to design the barrier reinforcement and concrete (Barker and Puckett 2007).

Traffic barriers are usually tested in three ways to determine their ultimate load carrying capacity and failure mode: crash testing, impact pendulum testing, and static (monotonic) testing.

2.4.1 Barrier crash testing

The dynamic performance of new barrier designs in Canada is only verified to be acceptable through full-scale crash tests. In crash testing, a vehicle with characteristics dictated by the required test level (Table 2.4) is driven into a barrier. During this collision, the barrier is subjected to transverse load from front side collision, longitudinal load from vehicle dragging, and vertical load from vehicle override (Alberson et al. 2004). This collision induces impact energy (i.e. load multiplied by displacement) on the barrier over a short period of time, which damages the barrier. The total kinetic energy associated with the velocity normal to the barrier, often called impact severity, must be converted into potential energy as the vehicle raises up the face of the barrier for the test to be successful (Rosenbaugh et al. 2007).

As an example, Alberson et al. (2004) conducted crash tests on three Florida safety shaped barriers to determine their compliance with TL-4 performance requirements. In one test, a 2000 kg pickup truck traveling at 100 km/h impacted a barrier at an impact angle of 25°, which represents crash test requirements for TL-4 barriers according to the NCHRP report. As seen in Figure 2.7, the barrier contained and redirected the truck without being penetrated, under-ridden, or over-ridden which deems it structurally adequate. No penetration or potential for hazard was present to the occupant compartment nor the vehicle was overturned which satisfies the occupant risk article in the safety evaluation. Finally, the vehicle had satisfactory trajectory after the collision. Hence, the Florida barrier performance was deemed crashworthy according to the requirements of NCHRP report for a TL-4 barrier.

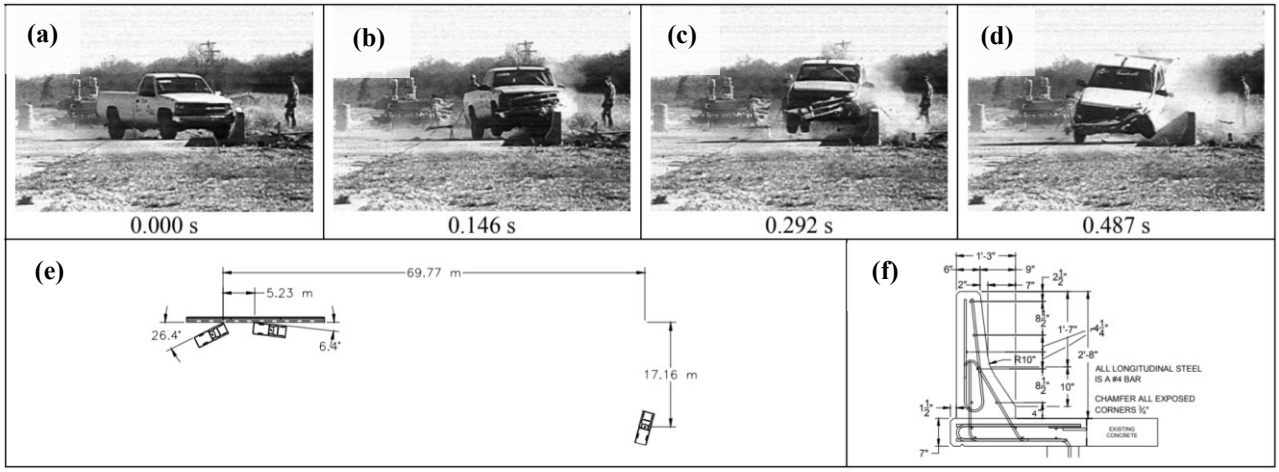

Figure 2.7: Crash test into a TL-4 Florida Jersey safety shaped bridge barrier (a through d) impact in milliseconds (e) impact scheme (f) Florida barrier cross section (Alberson et al. 2004).

2.4.2 Barrier impact testing

In impact (also known as pendulum) testing, a solid mass is swung into barriers to create equivalent impact energy to those produced by vehicles in crash testing. This mass may be a pear-shaped iron ball (El-Salakawy et al. 2004) or a set of steel plates bolted together (Mitchell et al. 2005). This test method is often used in the initial design and refinement of new barrier configurations as it is cost-effective compared to actual crash testing (Mitchell et al. 2006). To simulate vehicle impact, Mitchell et al. (2006) used pendulum masses based on controlled force levels and impact duration by utilizing a steel crush package (bundled steel tubes that simulate vehicle-specific impact characteristics (i.e. crumple zones)) mounted on a pendulum mass (Figure 2.8c). This mass is designed with a specific weight and dropped from a specific height to meet the NCHRP Report 350 TL-3 criteria (Figure 2.8d). Tests were conducted on cast-in-place and retrofitted barriers (using through-anchor and under-cut anchor configurations as shown in Figure 2.8a and Figure 2.8b, respectively) and compared to Finite Element models (FEM) developed with LS-DYNA. The impact test pendulum and FEM give good simulations of an NCHRP TL-3 vehicle impact. Using the pendulum impact test in addition to the analytical models can reduce costs by decreasing the number of required crash tests (Mitchell et al. 2006).

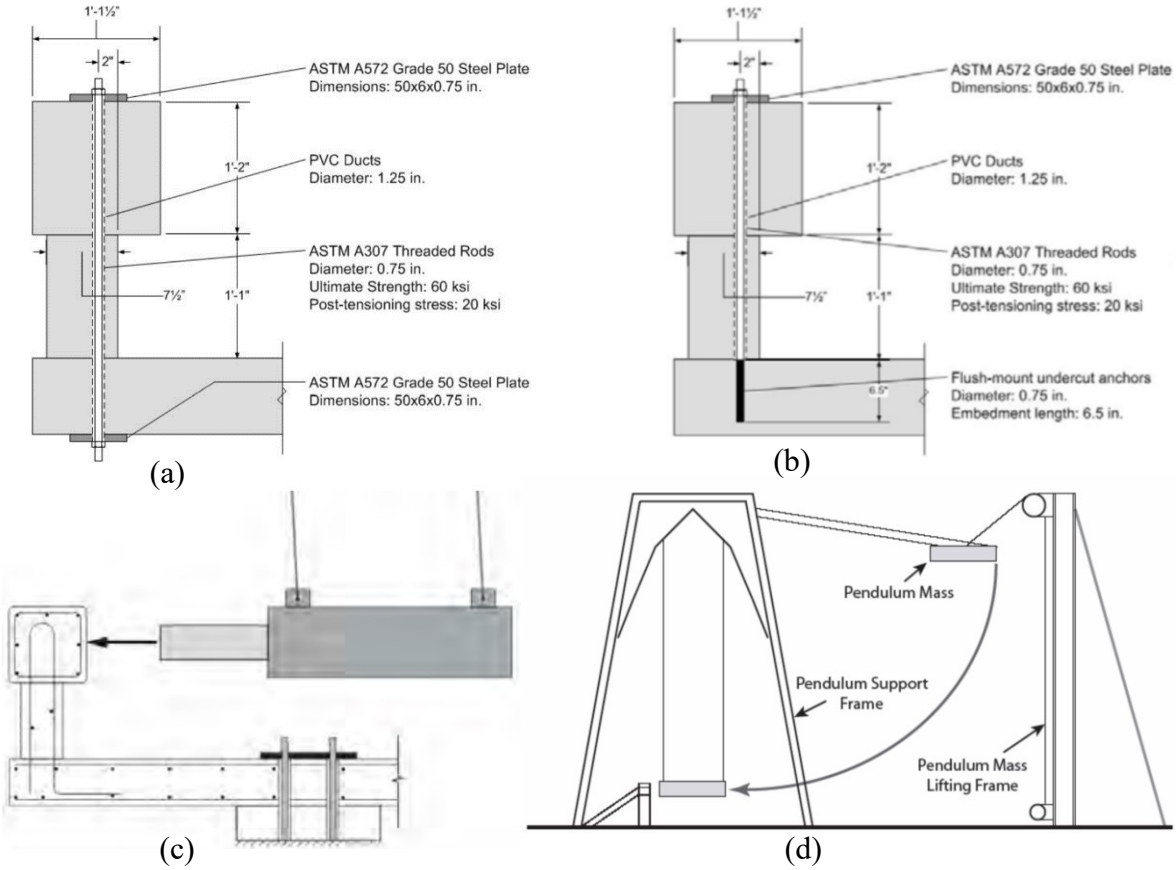

Figure 2.8: (a) Retrofit barrier with through-anchor configuration (b) retrofit barrier with under-cut anchor configuration (c) a bridge barrier-deck specimen and the pendulum mass installed with a crush package (d) impact test pendulum setup (Mitchell et al. 2006)

2.4.3 Barrier static testing

In static testing, barriers are subjected to an increasing monotonic transverse load until failure. This load is distributed over a specific length and at a particular height as per CHBDC requirements (Table 2.4 and Figure 2.6). Static tests are often used for preliminary barrier design and refinement of barriers designs (particularly to study barrier anchorage, barrier reinforcement, and concrete strength) or to justify minor changes to successfully crash-tested traffic barriers (CSA 2014b).

In the barrier design, designers consider transverse load (P_t) is applied over a barrier length of 1200 mm for TL-1 and TL-2 barriers, 1050 mm for TL-4 barriers, and 2400 mm for TL-5 barriers. Longitudinal load (P_l) is applied at the same locations and over the same lengths as the transverse load. Moreover, a vertical load (P_v) is applied over a barrier length of 5500 mm for TL-1, TL-2, and TL-4 barriers and 12000 mm for TL-5 barriers (CSA 2014a). These lengths are based on previous crash tests of traffic barriers of the same test level category and represent the contact

length between the vehicle and barrier (AASHTO LRFD 2007). However, in static testing only the transverse load is considered for static testing of barrier walls and their anchorage since it creates the most critical loading case (Sennah et al. 2010). In static testing, a live load factor of 1.7 is applied to the loads specified in Table 2.4, meaning that a TL-4 barrier would have acceptable static performance if it can resist a 170 kN transverse load without failing.

Crash tests by Alberson et al (2004) were followed by static tests replicating the most critical load used in design (i.e. the transverse load) to verify the analytical capacity of the barrier. As seen in Figure 2.9, a hydraulic ram attached to a braced load frame, pushing on a load cell, and placed against a spreader beam was utilized to apply the static load. It was concluded from static testing of the barrier that the actual capacity exceeded yield line analysis predictions by around 10%. Also, it was inferred that static analysis using yield line theory provides good estimates of failure loads.

Figure 2.9: Test setup for static load testing (Alberson et al. 2004).

Mitchell et al. (2006) state that in a typical cast-in place barrier, half of the static capacity comes from continuity (i.e. two-way load distribution) of the barrier, and the other half comes from the capacity of the stand-alone (i.e. one-way load distribution) barrier. This difference is evident in the difference between the middle (continuous) and end (discontinuous) parts capacities of barriers.

2.4.4 Preliminary Design of bridge barrier-deck overhangs

Both the CHBDC and AASHTO (2007) specify that barriers should be crash-tested to evaluate their performance. However, both codes allow using static loads equivalent to dynamic vehicle impact loads to design reinforcement and anchorage of barrier-deck overhangs. For instance, CSA S6:19 states that transverse, longitudinal, and vertical loads of 100, 30, and 30 kN, respectively, must be applied simultaneously over a barrier width of 1050 mm for the transverse and longitudinal loads and a length of 5500 mm for the vertical load to preliminary design TL-4 barrier-deck overhangs (CSA 2019). AASHTO (2007) specifies a transverse load of 240 kN for a type TL-4 barrier. Since barriers design is based on ultimate limit states, the transverse load is multiplied by

a factor of 1.7 (CSA 2014a) or 1.0 (AASHTO 2007). Hence, the design transverse equivalent static load for a TL-4 barrier is either 170 kN or 240 kN, respectively depending on which standard is followed. This thesis will focus on the S6:19 requirements. This design load is then used to calculate horizontal and vertical reinforcement for barrier walls reinforced with steel and anchorage between barrier walls and deck slabs using yield line analysis.

Yield line analysis is based on conservation of energy, the reinforcement yielding pattern, and the adequate ductility of reinforcement to allow for plastic hinge formation until a plastic collapse mechanism forms. Yield line analysis is used for various RC design applications including two-way slabs (Wight and MacGregor, 2012). Expressions to evaluate barrier capacity using yield line theory were developed decades ago (Hirsch 1978). These expressions assume that yield lines caused by a truck collision produce a force, distributed over a length, as shown in Figure 2.10. This two-way behaviour of load distribution in barriers is realistic and represent failure modes often observed in vehicle crash testing. A 6-metre-long barrier is long enough to evaluate horizontal and vertical (i.e. two-way) load distribution (El-Salakawy and Islam 2014) while segments 2.0 to 2.6-metres wide exhibit one-way behaviour which result in flexural failure (El-Salakawy et al. 2003, Ahmed et al. 2013). One-way behaviour is acceptable for determining the anchorage capacity of barrier walls and as an initial test to evaluate barrier-deck overhang performance in general.

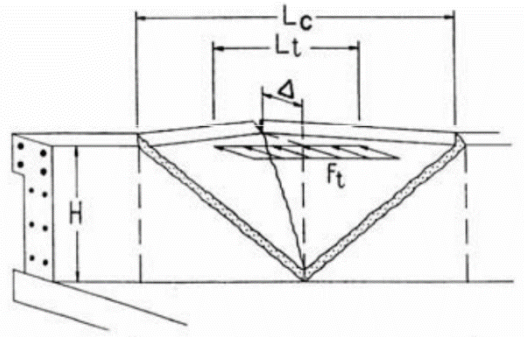

Figure 2.10: Yield line pattern for impact in the middle of a concrete barrier parapet, reproduced from AASHTO LRFD (2007).

2.5 BRIDGE DETERIORATION AND DAMAGE

Relative to other structures, bridges are particularly vulnerable to deterioration and damage. Bridges are essential transportation network links and a bridge going out of service can have significant economic consequence to a region (Shipilov 2009). Bridges are also at risk of being exposed to extreme loads (e.g. vehicle impact) and repeated heavy load cycles more than most

other structures. Lastly, bridges are more exposed to environmental deterioration mechanisms than most other structures. Bridge deterioration and damage is an economical and, more importantly, a life-safety issue. For instance, the collapse of an overpass over Highway 19 in Laval, Quebec in 2006 crushed two vehicles, killed five people, and injured six others (Shipilov 2009).

2.5.1 Vehicle Impact Damage

Bridges are susceptible to damage from vehicle impact over their construction and use. This includes impacts from below (e.g. truck colliding with bridge girders) as well as barrier collisions.

A cursory internet search for news articles about vehicle-bridge collisions includes many examples of these incidents every week with several of these incidents unfortunately involving injury or death. In many incidents, damage to the bridge or vehicle occupants is negligible. For instance, roughly one vehicle (typically an RV or a small moving truck) crashed into the Norfolk Southern-Gregson Street Overpass in North Carolina each month between 2008 and 2019 (when the bridge was raised). Many of these collisions were captured on video and can be found in internet searches for '11-foot-8 Bridge' (name references the bridge's overhead clearance). These collisions happened at relatively low speeds, involved weak parts of the colliding vehicles, and usually were against a specially designed 'crash beam' so damage to the bridge was minimized and injuries were rare and minor.

However, in other situations the damage is not negligible. In 2014, a dump truck with a raised bed crashed into overhead structural members on the Burlington Skyway (between Burlington and Hamilton) Ontario which caused over one million dollars of damage (i.e. direct cost) and delayed a major transportation route for several days (i.e. indirect cost). Many collisions involve barriers with there being numerous examples of barriers being damaged or failing (either in their function to prevent vehicles from leaving the roadway or by losing structural integrity) in the news each week.

2.5.2 Steel Corrosion

Corrosion of metallic elements (e.g. steel girders, steel reinforcement) is a major concern for existing infrastructure. A 2005 study estimated the direct cost of corrosion of highway bridges in Canada for that year to be $1.243 billion (Canadian dollars) with $300 million of that sum attributed to maintaining and rehabilitating RC bridge decks. Furthermore, the indirect cost to users (e.g. traffic delay, lost productivity) can be ten times that of direct corrosion costs (Shipilov 2009).

The iron in steel has a natural tendency to return to its natural state as iron ore. The rate of this process depends on the availability of water, oxygen, and aggressive ions (i.e. chlorides), the pH and temperature of the surrounding environment, and internal properties of the steel (e.g. composition, grain structure, and residual stresses) (Virmani and Clemena 1998). Due to the high pH (about 13) of the concrete pore water solution, a passive oxide layer is formed on the surface of reinforcing steel that protects steel against electrochemical corrosion (Bentur et al. 1997). The corrosion rate remains low if the passive layer remains intact. However, once this layer is broken, oxygen reacts with steel which leads to corrosion (Chess 1998, Polder 1998). Steel in concrete that is either very dry or continuously saturated is not susceptible to significant corrosion due to the lack of necessary air and water to initiate corrosion (Jones 1996). However, use of deicing salts on bridges in winter causes dissolved chloride ions to permeate concrete and enhance oxidation through the formation of an iron chloride complex as well as the disrupt the passive film on the reinforcement by lowering the concrete's pH. Corroded steel has a volume three to six times the original steel and expansion caused by corrosion induces tensile stresses on the surrounding concrete that leads to concrete cracking, delamination, and spalling (Jones 1996, Van Dyke et al. 2017). Once concrete cracks or spalls, new pathways are presented for chloride ions to reach reinforcing steel. These cracks are further expanded from repeated freeze-thaw cycles acting on concrete. This process aggravates the intensity of corrosion through a positive feedback loop.

Carbonation is the degradation of concrete due to its porous structure and natural reactivity which allows the penetration of CO_2 into the concrete layer and subsequent neutralization of alkalis in the pore fluid in concrete. Carbonation reduces concrete's pH to around 9 where the passive layer formed around steel becomes unstable and corrosion may occur (Aperador et al. 2015). This type of corrosion induced by carbonation can corrode the entire surface of steel bars due to the complete dissolution of the passive layer around the steel (Broomfield et al. 2006).

The first means of protecting against corrosion of reinforcing steel is high quality (i.e. low permeability) concrete. However, even high-quality concrete cracks over time and permits chlorides to reach the reinforcement. Therefore, measures to protect RC against corrosion should include the reinforcement itself.

2.6 BRIDGE REINFORCEMENT TYPES

Bridge decks and barriers are often reinforced with one of six types of reinforcement: mild steel, epoxy-coated steel, galvanized steel, stainless steel, microcomposite steel, and fibre reinforced polymer bars. General material properties for these materials are given in Table 2.5.

Table 2.5: Typical tensile material properties of reinforcement used in bridge decks.

Bar Type	Yield Strength, MPa	Peak Strength, MPa	Elastic Modulus, GPa	Rupture Strain, %	Bond Strength, MPa
Mild Steel (Grade 400)	400	650	200	10.0	10.0
Epoxy-Coated Steel	420	620	200	10.0	8.0
Galvanized Steel[c]	470	720	200	10.0	--
Stainless Steel 304[a]	515-690[b]	650-860	200	12-25	--
Stainless Steel 316[a]	515-690[b]	650-860	200	12-25	--
Titanium 6Al 4V[d]	965	1100	114	10.0	--
Glass FRP Bar[e]	N/A	800-1200	40-60	2.0	15
Carbon FRP Bar[e]	N/A	1648	140	1.18	16.3

[a]ASTM A276/A276M-17 (2017)
[b]Measured by the offset method (0.2% offset) described in ASTM A370.
[c]Frosch et al. (2014).
[d]Platt and Harries (2019).
[e]Nominal properties given by FRP manufacturers.

2.6.1 Mild Steel

Mild steel is a type of low carbon steel used to reinforce the majority of RC structures in use today because of its compatibility with concrete, low cost, and advantageous material properties. Compared to high carbon and alloy steels, mild steel is more ductile and weldable but has lower tensile strength. Corrosion of mild steel occurs if it is not properly protected. Application of coatings on mild steel reinforcement tends to be more economical than using reinforcement made of corrosion-resistant materials. Reinforcement coatings are divided into two basic categories: organic and metallic.

2.6.2 Epoxy-coated steel reinforcement

Epoxy-coated steel was introduced in the 1970s as a method adapted from one used for coating pipes in the petroleum (Manning 1996). Epoxy's protection is based on its ability to act as a physical (prevents harmful ions from reaching the steel) and electrical (increases electrical resistance between steel elements) barrier (Virmani et al. 1983).

The first bridge reinforced with epoxy-coated steel was built in 1973. (Virmani and Clemena 1998). However, problems with epoxy were discovered in 1986, only six years after a set of bridges in the Florida Keys reinforced with epoxy-coated steel were constructed. After inspecting these bridges, it was found that epoxy had debonded (Manning 1996). Following this observation,

investigations were carried out (Sagues et al. 1994) and new specifications were developed (Virmani and Clemena 1998). Though these measures improved epoxy-coated bar performance, researchers still questioned the use of epoxy-coated reinforcement at preventing corrosion in RC structures (Clear et al. 1995, Manning 1996).

Pyc et al (2000) studied epoxy-coated reinforcement taken from 18 bridge decks, constructed between 1977 and 1995 in Virginia. This study revealed that debonded coatings allow chlorides, moisture, and oxygen to reach the steel. This initiated corrosion mechanisms similar to that of bare mild steel bars in acidic environments (i.e. faster than corrosion of mild steel in concrete). In addition, 94% of samples showed evidence of adhesion reduction, including some with complete debonding. Based on these studies, Florida's DOT banned epoxy-coated steel as reinforcement in substructures in 1988 and in all construction in 1992 (Manning 1996, Smith and Virmani 1996).

Similarly, the Ministry of Transportation of Ontario (MTO) discontinued use of epoxy-coated steel for future bridge construction based on findings from field studies that included a significant number of MTO bridges documented with poor performance of epoxy-coated steel bars (Schell et al. 2005, Masoudi 2013). Pour-Ali et al. (2015) reported a severe decrease in the bond strength between epoxy-coated steel rebar and concrete after one year of immersion in a sodium chloride solution, which simulates chloride-laden concrete environment, attributed to expansive corrosion of the steel. Moreover, epoxy-coated steel is inefficient for long-term corrosion protection due to their porous and hydrophilic nature. As a result, Pyc et al. (2000) suggest that epoxy coated steel provides little or no additional service life for concrete bridge decks compared to mild steel in a moist environment due to the debonding of the epoxy coating from the steel surface.

2.6.3 Galvanized steel

Protecting steel against corrosion with metallic coatings was proven in many applications before its introduction in reinforcing bars. Metallic coatings are classified as either sacrificial or non-sacrificial (noble). Sacrificial coatings (e.g. zinc) protect steel by slowly sacrificing themselves (i.e. zinc's higher reactivity causes it to corrode first while protecting the underlying steel) while noble coatings (e.g. copper, nickel) do not corrode but protect the underlying steel by forming a passive layer on top of it (Virmani and Clemena 1998).

Hot-dipped zinc (galvanized) coatings have been used to protect steel against corrosion since the 1920's (ASTM A123-28T, 1928). In 1935 a deteriorating bridge spanning salt water was

demolished. This bridge was built in the early 1900's. Upon demolishing, it was revealed that the deck was built using both mild and galvanized steel reinforcement. The mild reinforcement had corroded enough to cause concrete cracking, while the galvanized reinforcement had not (McCrum and Arnold 1993). In 1968, Michigan State researchers worked with the Federal Highway Administration (FHWA) to compare galvanized and mild reinforcement (McCrum and Arnold 1993). Bridge deck specimens were constructed using galvanized, epoxy-coated, and mild steel. Specimens were placed outdoors and exposed to natural weather plus weekly application of salt during cold weather (December through March) to simulate the use of deicing salts. Periodic observation and measurements were made over 17-years then the slabs were demolished and inspected for corrosion. The improved corrosion performance of slabs reinforced with galvanized steel justified the modest increase in cost but the exact extent of superiority of galvanized steel over mild steel was difficult to judge due to some shortcomings in their design and testing process.

2.6.4 Solid Stainless-Steel bars

Stainless steel refers to steels that contain a minimum of 12% chromium which makes the alloy considerably more corrosion resistant than mild steel. However, stainless steel reinforcement is often not feasible for many applications due to its high cost (Nürnberger 1996). There are three common types of stainless-steel reinforcement: 304, 316, and 316LN. (Smith and Tullmin 1999).

The corrosion resistance of two types of solid stainless-steel reinforcement (304 and 316) in concrete slabs was investigated by McDonald et al. (1998). These slabs contained either stainless steel in both the top and bottom mats of reinforcement, or stainless steel in the top mat and mild steel in the bottom mat and were subjected to severe environmental conditions (wet-dry cycles with concentrated sodium chloride) for around two years. Slabs reinforced with Type 304 stainless steel bars in both mats did not show any signs of corrosion while the other slabs reinforced with Type 316 stainless steel bars exhibited good corrosion performance regardless of which steel was utilized as a cathode (mild steel or stainless steel).

2.6.5 Microcomposite Steel bars

Microcomposite steel (MMFX2) is a type of steel comparable to stainless-steel in terms of corrosion performance. MMFX2 is a low carbon, chromium alloy steel that is modified at the nano scale to minimize the formation of microgalvanic cells (the driving force behind corrosion). The microstructure of MMFX2 steel is attributed to its chemical composition and the controlled-rolling production process (MMFX steel 2011). Relative to the earlier presented steel types, MMFX2 was

found to have the lowest life-cycle cost (56% that of mild steel, 41% that of stainless steel, and 77% that of galvanized steel) for a sample bridge deck in a structure that spans the Ohio River (Berke 2012). MMFX and stainless steel are also shown to have estimated times to corrosion onset exceeding 100 years, compared to 59 years for galvanized steel and 19 years for mild and epoxy coated steel (Berke 2012).

2.6.6 Fibre Reinforced Polymers (FRP)

FRPs were introduced in the 1940s for the aerospace and defense industries due to its high strength and low density (ACI 2015). FRP composites are made of a polymer matrix reinforced with fibres to add stiffness and strength along the fibre directions. Unlike steel, FRPs are anisotropic (have varying properties in different directions).

FRP applications extended to various commercial uses as consumers demanded inexpensive, strong, lightweight materials. It was not until the late 1970s when FRP bars became available commercially and considered for structural use (ACI 2015). In construction, FRP reinforcing bars are mainly used in applications where their properties are needed. For instance, their noncorrosive nature makes them useful in bridge decks exposed to deicing salts as well as in structures in highly corrosive environments such as seawalls. Their nonconductive behaviour makes them useful for Magnetic Resonance Imaging (MRI) units or other equipment sensitive to electromagnetic fields (ACI 2015).

2.6.6.1 Tensile behaviour of FRP reinforcement

FRP bars have a linear-elastic tensile response and fail with little warning (i.e. brittle). The mechanical properties (e.g. tensile strength, stiffness) of FRP bars are affected by factors such as fibre material, volume fraction (how much of the bar is fibre and how much is resin), type of resin matrix, and the manufacturing process (ACI 2015). Fibres are the main load carrying component in the composite, and provide strength and stiffness in the direction along their length. Fibres may be natural (e.g. flax, jute, basalt) or synthetic (e.g. glass, carbon). Synthetic fibres are more commonly used in construction due to their chemical compatibility with the polymer matrix which leads to a better fibre-matrix interfacial adhesion (Xie 2010) as well as their typically higher strength and stiffness. Glass is the most common fibre used in FRP bars due to its significant strength and economical cost compared to other types of fibres. Generally, Carbon Fibre Reinforced Polymer (CFRP) bars have higher tensile strength and modulus of elasticity than GFRP bars but are considerably more expensive.

Unlike steel, bar diameter affects the tensile response of FRP bars due to shear lag between fibre layers. This causes fibres near the outer surface of the bar to be subjected to higher stress compared to fibres located near the centre of the bar (Faza 1991), resulting in reduced effective tensile strength as bar diameter increases. For instance, GFRP bars were shown to lose ~40% of their tensile strength when their diameter was increased from 9.5 mm to 27.4 mm (Ehsani et al. 1995) but advances in FRP bar manufacturing processes since then have led to lower strength losses, only 15% of the tensile capacity lost for typical bars when their diameter increases from 10 mm to 25 mm, as reported by the manufacturer (TUF-BAR 2020).

Unlike steel, FRP bars cannot be bent in the field. Therefore, FRP bars (e.g. stirrups) are pre-bent by manufacturers before resin cures. The tensile capacity of the bend is significantly reduced due to stress concentrations at the bend. Tensile strength loss may be as high as 50% in the bent portion of the bars compared to the straight portion (Nanni et al. 1998). Just as with straight bars, recent advancements in production and understanding of these stress concentrations have led to more consistent and less severe capacity reductions.

2.6.6.2 Compressive Behaviour of FRP reinforcement

FRP bars have different properties in tension and compression. The compressive strength of GFRP and CFRP bars have been reported to be 55% and 78% of their tensile strength, respectively (Mallick 1988, Wu 1990). Likewise, the compressive moduli of elasticity of GFRP and CFRP bars are reported to be 80% and 85% of their tensile modulus of elasticity, respectively (Mallick 1988, Ehsani 1993). This, coupled with the fact that the modular ratio of GFRP to concrete is similar to 1.0, led to guidelines for designers to neglect the contribution of GFRP bars' compressive strength and allowed designers to replace GFRP areas with concrete in design (ACI 440.1R 2015, CAN/CSA S806 2012).

However, recent research on more modern GFRP bars has shown that GFRP has a comparable modulus of elasticity in both tension and compression. The compressive modulus of elasticity was observed to be 97% to 120% of the tensile modulus of elasticity. Therefore, assuming equal moduli of elasticity in tension and compression is justified but the same cannot be said about the compressive and tensile strength of GFRP bars since the average compressive strength was between 55% to 99% of the tensile strength (Khorramian and Sadeghian 2019).

2.6.6.3 Shear Behaviour of FRP Bars

In general, FRPs are weak under interlaminar and transverse shear since layers of unreinforced resin lie between fibre layers. The interlaminar and transverse shear strengths of FRP bars are dictated by the strength of the relatively weak polymer matrix. This shortcoming can be overcome by orienting the FRP fibres in off-axis direction across the layers such that they will resist the applied loads through axial tension in fibres and increase the shear strength. (ACI 440R-07, Singh 2015). ACI requires that the shear strength of FRP bars exceed 124 MPa (ACI 440.6-08) which is one reason why some bar manufacturers weave spiral reinforcement around the core longitudinal fibres. Despite this limitation, large GFRP pavement dowels are used in various applications.

2.6.6.4 FRP-Concrete Bond behaviour

Bond stress between FRP bars and surrounding concrete is transferred to fibres via the resin. Factors that influence the bond performance of FRP rebar are its manufacturing process, mechanical properties, and environmental exposure. The bond mechanisms between concrete and FRP bars is similar to those for steel bars and attributed to chemical adhesion of the interface, friction caused by the roughness of the interface against slip, and mechanical interlock due to irregularity (typically from sand coatings for GFRP bars) of the bar texture (ACI 440.1R-15). These contributions form a resultant force that is resolved as a radial splitting component perpendicular to the bar and a shear component parallel to the bar. These two forces apply normal and shear stresses on the surrounding concrete that cause tensile stresses to develop in the concrete that may result in cracking in planes perpendicular and parallel to the reinforcement. To ensure these stresses do not exceed the concrete tensile strength and cause bond failure, adequate anchorage length of the rebar and sufficient confinement (provided by concrete cover and/or transverse reinforcement) in the concrete is provided. This allows bond forces at the material interface to be transferred efficiently under load (ACI 408R-03).

There are two types of bond failure: splitting failure and pullout failure. In splitting failure, concrete surrounding the bar splits before the rebar ruptures (Figure 2.11a) while pullout failure happens when the rebar pulls out of the surrounding concrete before it ruptures or the concrete splits (Figure 2.11b) (ACI 408R-03). Unlike steel bars, the bond strength of FRP bars to concrete appears not to be significantly dependent on concrete compressive strength provided that sufficient concrete cover is provided to prevent splitting failure (Nanni et al. 1995, Benmokrane et al. 1996,

Kachlakev and Lundy 1998). Sufficient cover was found to be at least twice the bar diameter which led to pullout failure or bar rupture instead of concrete splitting (Ehsani et al. 1996).

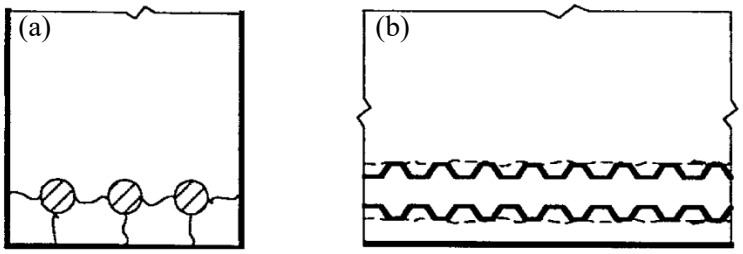

Figure 2.11: Cracking and damage mechanism of bond (a) splitting cracks between rebar and through concrete cover (b) shear crack and/or concrete crushing due to bar pullout (ACI 408R-03).

Based on experimental tests on FRP bars, the bond performance of FRP bars depends on factors including bar diameter, surface conditions (e.g. deformed, sand-coated), Poisson's ratio, concrete strength, and confinement stresses (e.g. clamping forces from supports, stirrups) (Al-Dulaijan et al. 1996, Nanni et al. 1997, ACI 440R-07). Many test methods have been used to evaluate the bond strength of FRP bars. These include pullout tests, beam end tests, beam anchorage tests, and beam splice tests (ACI 408R-03).

A pullout test is a comparative bond evaluation test method for FRP bars in which a bar is embedded at a depth equal to five times the bar diameter in a concrete block. The bar is then pulled to obtain the average bond stress and bond stress versus slip at the loaded end. Although pullout tests were popular, they do not represent realistic situations and are not a valid test to determine the development length needed in the design of flexural members (ACI 440R-07). They are not realistic since splitting of concrete is prevented due to the absence of local bending on the bar, concrete covers are higher than typical applications, and confining action of the reaction plate on the concrete specimen is higher than in realistic cases. These factors are not present in more representative beam tests where concrete surrounding the bars is in tension, leading to concrete cracking under lower stresses which in turn yields reduction in bond strength (Tighiouart et al. 1998). Therefore, beam tests are preferred and more reliable in providing realistic measures of bond strength and determining design development length in actual structures (ACI 408R-03).

A minimum embedment length is required to develop the full capacity of a bar. In the CHBDC, a minimum embedment length of $36d_b$ is required to develop the maximum tensile capacity of a #5 GFRP bar (Ahmed et al. 2008), though (similarly to steel rebar) larger bars tend to have reduced bond strength with increased bar diameter (Ehsani 1996, Ahmed et al. 2008).

2.7 DEVELOPMENT OF FRP REINFORCED BRIDGE COMPONENTS FOR NEW CONSTRUCTION

Since their introduction, FRPs have been used in many different applications in bridge construction and rehabilitation. The Beddington Trail Bridge in Calgary, Alberta was completed in 1993 and is the first Canadian bridge to contain girders internally reinforced with FRP. This bridge contained bulb-tee precast girders pre-tensioned with CFRP tendons. Later that decade, Taylor Bridge in Manitoba was constructed and it was one of the world's largest highway bridges reinforced with FRP. This bridge contained four concrete AASHTO type girders prestressed with two different types of CFRP tendons. These girders were also reinforced with CFRP stirrups protruding from the girders to act in composite action with the bridge deck. Both bridges girders performed as designed under traffic loads (Rizkalla and Tadros 2003) and are still in service today.

Bridge columns, particularly those in marine environments and cold regions, are susceptible to corrosion and consequently loss of structural integrity (Seible 1996). To address this issue, concrete filled GFRP tubes were introduced as a durable, corrosion resistant, cost effective system. These types of systems also benefit the structure by significantly improving the axial strength and ductility of concrete columns through confinement pressure (Fam and Rizkalla 2001).

Slabs are typically the most vulnerable bridge element to corrosion since deicing salts deposited on the bridge (either directly by maintenance vehicles or indirectly by traffic that carries salts in from elsewhere) can reach deck reinforcement first. FRP reinforcement is a viable alternative to traditional steel in slabs due to its superior corrosion resistance. The ultimate load carrying capacities of slabs reinforced with FRP are equal to or higher than that of slabs reinforced with conventional steel but slabs reinforced with FRP grids adsorb less energy than ones reinforced with steel due to the brittle nature of fracture in the FRP (Banthia et al. 1995). To satisfy serviceability and ultimate capacity requirements for GFRP-RC decks with span-to-depth ratios ranging between 9 and 15, reinforcement ratios of 1.2% for bottom reinforcement and 0.6% for top reinforcement in the transverse direction, as well as 0.6% for top and bottom reinforcement in the longitudinal direction have been found to be sufficient. These percentages are influenced by the FRP's elastic modulus with higher modulus bars requiring lower reinforcement ratios to satisfy these limits. At ultimate limits states, punching shear is the likely failure mode of typical GFRP-RC decks with the punching shear resistance being most affected by the stiffness of the bottom transverse reinforcement (Hassan et al. 2000). In essence, FRP-RC decks are designed based

providing stiffness equivalence to a steel-RC deck for the bottom transverse bars and strength equivalence to a steel-RC deck the other bars (Khanna et al. 2000).

In 2003, a 70-year-old deteriorated slab-on-girder superstructure was replaced with a prefabricated GFRP reinforcement system in Missouri, as shown in Figure 2.12 (Matta et al. 2007). The re-decking was completed in only five days with a reduction in construction time of over 70% compared to similar bridges where conventional steel reinforcement is used. The system concept, detailing and construction procedure were designed to improve constructability and to allow ease of walking over the three-dimensional assembly.

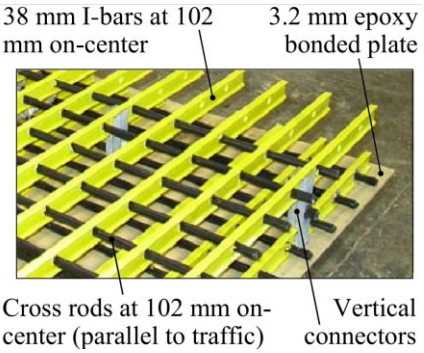

Figure 2.12: Prefabricated GFRP SIP deck panel (Matta et al. 2007).

The CHBDC introduced Section 16, which discusses using FRP in bridges, in 2000. Clause 16.8.8 of the CHBDC addresses the design of cast-in-place FRP-RC deck slabs. The diameter of GFRP bars must not be less than 15 mm, the longitudinal bars in the bottom assembly and the transverse and longitudinal bars in the top assembly must have reinforcement ratios exceeding 0.0035, and the minimum cross-sectional area (mm^2/mm) for transverse GFRP bars in the bottom assembly must be $500d_s/E_{FRP}$, where d_s is the distance from the top of the slab to the centroid of the bottom transverse bars and E_{FRP} is the bar's elastic modulus. This requirement represents the fact that axial stiffness, not strength, of the bottom transverse bars governs the load-carrying capacity of deck slabs (Khanna et al. 2000). The minimum clear cover and its construction tolerance for FRP bars and grids must be 35 ± 10 mm (CSA 2014b).

2.7.1 FRP's use in Bridge Barriers

Provisions and design requirements for steel-RC bridge barriers are found in Section 12 of the CHBDC while §16.10 of the code and C16.10 of the commentary present details and specifications for FRP-RC barriers. The main difference required for the design of FRP-RC barriers is the linear elastic behaviour of FRP bars. Unlike steel-RC barriers, moment redistribution required for plastic

hinging assumptions of the yield line analysis of barriers is invalid for FRP-RC. Though codes do not provide guidance on methods analogous to yield line analysis for FRP-RC, El-Salakawy et al. (2004) and Sennah et al. (2011) suggest modifying yield line approaches for GFRP-RC barriers by replacing yield strength with rupture strength of GFRP bars because of their brittle behavior.

One of the earliest GFRP-RC barriers was the open post-railing system shown in Figure 2.13 (Buth et al. 2003). GFRP bars were used to reinforce concrete bridge rails supported by concrete posts. Transverse reinforcement in the top and bottom layers of reinforcement in the deck overhang consisted of #6 (20 mm diameter) GFRP bars spaced 140 mm apart and the longitudinal reinforcement in the top of the deck cantilever consisted of #5 (16 mm diameter) GFRP bars spaced 229 mm apart. Vertical reinforcement on the front face of each post consisted of #6 "L" shaped GFRP bars at 90 mm spacing. This open post-railing system was crash tested and performed satisfactorily except that there was an occupant risk due to vehicle rollover. This issue was fixed in a modified version of this barrier that included a metal rail on top (Buth et al. 2003).

Figure 2.13: Open post-railing reinforced with GFRP and test vehicle (Buth et al. 2003).

The response of entirely GFRP-RC barriers resembling shapes used in Canada and their connection to the bridge deck was investigated by El-Salakawy et al. (2003) via experimental tests on continuous PL-2 and PL-3 barriers subjected either to out-of-plane static load or pendulum impact loads. In addition, they introduced detailing to connect the barrier wall to the deck by extending the main barrier reinforcement through the deck. Full-scale GFRP-RC deck-barrier overhangs, with 2 m widths for static testing and 10 metres for pendulum testing were designed with similar reinforcement schemes. These GFRP-RC barriers were comparable to identical (same geometry and reinforcement ratio) steel-RC counterparts based on cracking, deflections, strains, energy absorption, integrity, and ultimate strength. The length over which cracks spread due to the impact load, was 2.9 to 3.3 m at the top of the wall, diminishing to 0.9 to 1.2 m at the base of the wall for PL-2 barriers at the middle section which is in agreement with the values predicted by the yield

line, analysis which predicted this affected critical length to be 2.77 m (El-Salakawy et al. 2004). Based on this work, proposed reinforcement configurations for GFRP-RC barriers were later approved by the Ministry of Transportation of Québec (MTQ) and adopted by the CHBDC (CSA 2014b). As a result, a research bridge (Val-Alain Bridge) was constructed with GFRP-RC decks and PL-2 GFRP-RC barriers in Québec on Highway 20 in 2004 (Benmokrane et al. 2007). The bridge is a slab-on-girder type with a skew angle of 20° over a 50 m single span and a total width of 12.6 m. The bridge has four simply supported steel girders spaced at 3145 mm, a 225 mm thick concrete deck, and overhangs of 1570 mm on each side. The bridge deck was tested for service performance using two four-axle calibrated trucks in different path and location scenarios, and it performed satisfactorily.

Five other research bridges that utilize FRP reinforcement were constructed and instrumented with fibre optic sensors in North America, namely Wotton, Magog, Cookshire-Eaton, and Melbourne in Quebec, and Morristown bridge in Vermont. All these bridges are slab-on-girder bridges with main girders spanning between 26.6 to 50 metres and decks ranging from 200-230 mm thick. The bridges were tested for service performance using calibrated truckloads. This study showed that analytical predictions and field results under real service conditions, in terms of deflections, cracking, and strains in reinforcement and concrete, were comparable to steel-RC bridge decks (Benmokrane et al. 2011).

2.8 TESTING OF RETROFITTED BARRIERS

2.8.1 Retrofitting Vehicular Barrier using Mechanical Anchors

Mitchell et al. (2006) developed preliminary patterns and spacing of steel mechanical anchors for retrofitted bridge barriers, tested this system using both pendulum and quasi-static testing, then compared its performance to cast-in-place barriers. They used two types of anchors to retrofit TL-3 barriers: undercut anchors configuration and through-anchor configuration (Figure 2.8). Barriers retrofitted with undercut anchors performed poorly so this system was rejected and considered an invalid retrofitting technique. However, retrofitting barriers with through-anchors was found to be a potential design based on its performance compared to cast-in-place barriers (Mitchell et al. 2006).

2.8.2 Repair of GFRP-reinforced bridge decks and barriers

El-Salakawy et al. (2010) investigated concrete demolition techniques for GFRP-RC decks. Conventional concrete demolition methods (e.g. jackhammering and water blasting) severely damaged GFRP reinforcement. They recommended that damaged GFRP-RC be saw-cut and that interrupted reinforcement should be replaced by new FRP bars. They also investigated repair techniques for GFRP-RC bridge deck slabs and presented two techniques effective for repairing these slabs. One technique is doweling (planting) reinforcement which is widely used and well established for repairing steel-RC slabs, while the other technique is the near-surface mounting (NSM) of reinforcement which has been used effectively for strengthening RC elements.

2.8.2.1 Doweling (Planting) Technique

Doweling consists of drilling holes in existing concrete, partially filling the holes with an adhesive bonding agent (epoxy or cementitious), then inserting (i.e. planting) new FRP bars (El-Salakawy et al. 2010). The design detailing for the doweling technique is affected by factors such as: embedment length, splicing spacing, and bonding agent.

Inadequate embedment length means doweled bars will pull out of the concrete before achieving their tensile strength. Based on pull-out tests, embedment lengths of $30d_b$ are enough to develop the tensile capacity of GFRP bars ($f_u \approx 700$ MPa) under direct axial tension. However, if the anchorage zone of planted GFRP bars is subjected to flexural stresses, which result in flexural cracks, this anchorage length will need to be more than $30d_b$ (El-Salakawy et al. 2010).

For bar spacing, ACI 355.2-01 (2001) states that hole spacing, which is the centre-to-centre distance between the existing and planted bars, should be between two to three times the bar diameter for doweling bars in steel-RC slabs. El-Salakawy et al. (2010) observed that increasing the spacing between the planted and existing GFRP bars from $2d_b$ to $4d_b$ was effective at increasing the ultimate capacity of the spliced slab.

Doweled FRP bars are bonded to the surrounding concrete through a bonding agent. El-Salakawy et al. (2010) tested two bonding agents, a cement-based material (non-shrink grout) and a polymer based material (epoxy). Using epoxy, which tends to be stronger than grout, as a bonding agent exhibited higher performance in terms of the ultimate capacity of the repaired section than using grout.

El-Salakawy et al. (2014) used the doweling technique to repair GFRP-RC barriers as follows:

1. Damaged portions of the barrier wall and the deck slab underneath the wall base were saw-cut, and damaged concrete was removed.
2. Holes were drilled in the barrier and the overhanging deck (Figure 2.14). After cleaning the holes, Epoxy was mixed and injected into them, and then GFRP bars were doweled into the holes. New GFRP bars were spliced to doweled bars with an overlap length of $40d_b$.
3. Formwork was placed and new concrete was cast in the repaired portion (El-Salakawy et al. 2014)

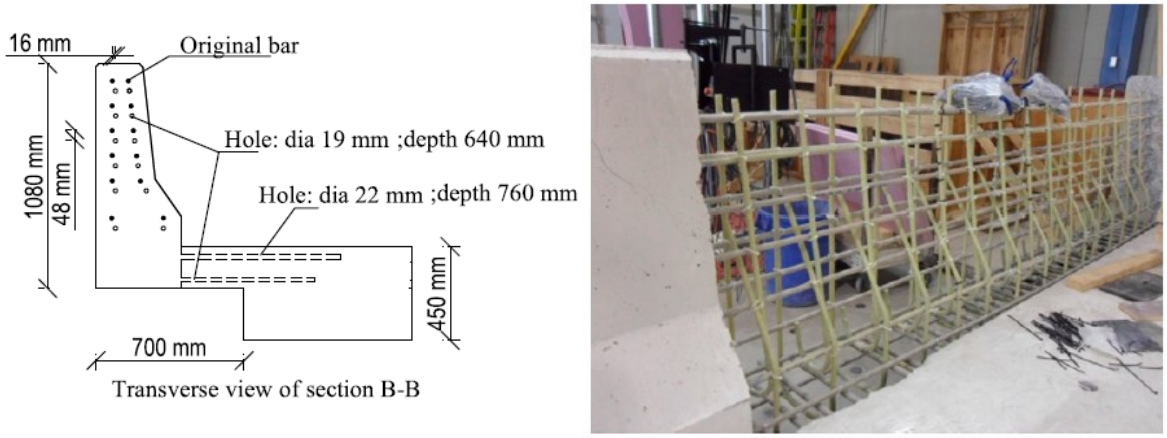

.

Figure** 2.14**: Doweling technique showing hole layout and photograph of planted reinforcement (El-Salakawy et al. 2014).

2.8.2.2 NSM Technique

The near-surface mounting (NSM) of FRP reinforcement has attracted attention from both researchers and practitioners for strengthening and repair. In the NSM method, grooves are cut into the concrete cover of an RC element and then FRP reinforcement is bonded with an appropriate groove filler (typically epoxy paste or cementitious grout). This technique originated in Europe in the 1940's for steel-RC bridge slabs. At that time, mild steel bars were inserted in grooves cut into the concrete cover of RC flexural members and grout was used to bond the bars to concrete (Asplund 1949). However, mild steel utilized as NSM reinforcement was prone to corrosion, so it was later replaced by stainless steel and more recently by FRP bars in more modern applications (Lorenzis and Nanni 2002). El-Salakawy et al. (2010) investigated the NSM technique for repairing damaged GFRP-RC bridge decks and found it to be viable. Like with doweling, NSM in repairing damaged FRP-RC structures is influenced by factors including NSM-FRP bar location, groove size, groove spacing, quality of concrete substrate, embedment length, and bonding agent.

The structural performance (i.e. strength, crack pattern, deflections) of repaired GFRP-RC bridge barriers using either the NSM or doweling techniques was evaluated under static load (El-Salakawy and Islam 2014). The first phase of this project included testing full-scale GFRP-RC, 6.0-m-long PL-2 barriers connected to an overhanging portion of a 200-mm-thick GFRP-RC bridge deck slab. The second phase included repairing the damaged barriers using planting and NSM techniques, and then retesting the barriers under similar loading conditions to evaluate the performance of the two repair techniques. Four parameters associated with the two repair techniques were fixed: bar hole diameter was 3 mm larger than nominal bar diameter, spacing of new bars was $3d_b$ or spacing between original bars, whichever is less, bonding agent for FRP bars was epoxy, and embedment length was $40d_b$.

El-Salakawy et al. (2014) used the NSM technique to repair GFRP RC barriers as follows:

1. Damaged portions of the barrier including the slab beneath were saw-cut and damaged concrete was removed.
2. A diamond-blade, concrete-cutting machine and a jackhammer were used to cut grooves in the deck (30 mm wide and 330 mm long) and the barrier (25 mm wide and 350 mm long). Holes were drilled into the overhanging deck to plant vertical bars. See Figure 2.15 for more details.
3. Grooves were filled with epoxy to a 25 mm depth and GFRP bars were inserted. Epoxy was injected into the holes and vertical GFRP bars were inserted. Damaged concrete near the edge of the overhanging slab was also filled with epoxy.
4. New reinforcement was tied, formwork built, and concrete cast (El-Salakawy et al. 2014).

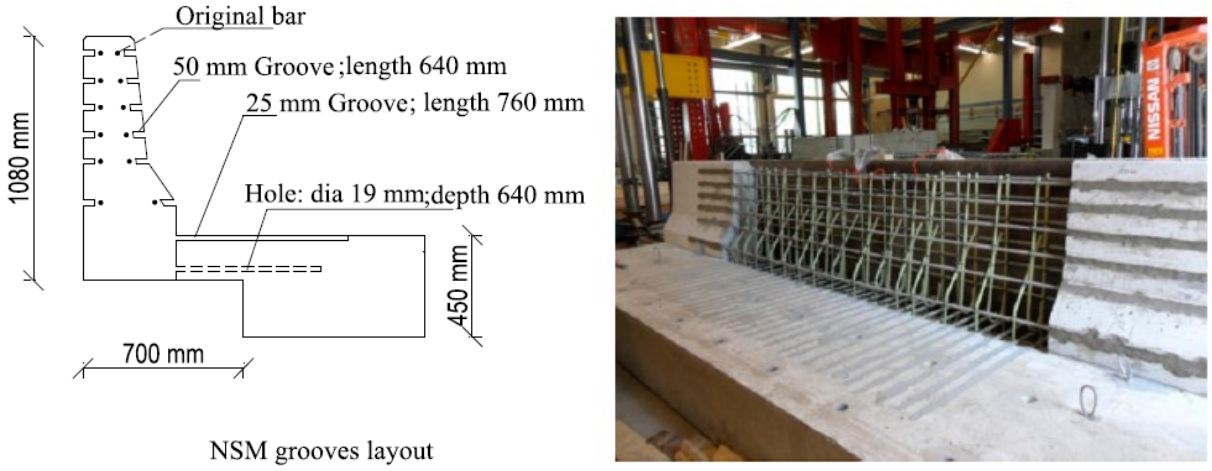

Figure 2.15: NSM technique showing NSM groove layout and photograph of NSM reinforcement (El-Salakawy et al. 2014).

Each repaired barrier, whether by using doweling or NSM techniques, tested by El-Salakawy et al. (2014) exceeded strengths required by the CHBDC and carried loads more than their control counterparts, except one barrier repaired at the edge using the doweling technique. The barriers tested at the middle failed in punching shear which indicates that 6.0-m-long segments are adequate to simulate the behaviour of continuous barriers carrying the applied loads in both the vertical and horizontal directions. Overall, the behavior of repaired barriers was similar to their control counterparts, in terms of measured strains and deflections (El-Salakawy et al. 2014).

2.9 GAPS IN THE RESEARCH

Although the CHBDC provides specifications on designing GFRP-RC barriers, it does not provide specifications on repairing or rehabilitating GFRP-RC barriers in case of damage caused by factors including exposure to freeze-thaw cycles, poor quality construction, inadequate maintenance, changes in level of service, and vehicle collision. Lack of specifications on repair of GFRP bridge barrier/deck overhangs is attributed to lack of research on the topic. This poses concerns regarding the feasibility and economics of repairing bridge elements reinforced with GFRP bars. El-Salakawy et al. (2010) investigated the effectiveness of repairing GFRP-RC slabs and addressed two questions: (1) What is the most suitable concrete demolition technique that causes minimal damage to the GFRP bars? (2) How effective is this technique in terms of the flexural strength and load-transfer efficiency of concrete slabs? They recommended that damaged concrete be saw-cut for the full-depth removal of concrete, and the interrupted reinforcement should be replaced with new GFRP bars using either the planting (doweling) or NSM technique. El-Salakawy et al. (2014) tested these techniques for bridge barriers on double-slope performance level-2 (PL-2) barriers. Both techniques showed satisfactory structural performance. Nevertheless, the efficacy of these techniques on different barrier configurations and reinforcement schemes has yet to be evaluated. Moreover, the tested overhang length of 1000 mm is shorter than the typical overhang lengths seen in real bridges.

To address this research gap, this thesis investigates the efficiency of using the doweling repair technique on single-slope Alberta TL-4 barriers reinforced with GFRP with a more realistic overhang length of 1500 mm. Alberta TL-4 barriers have never been totally (i.e. deck and barrier) reinforced with GFRP. Ahmed et al. (2010) explored using GFRP bars in Alberta TL-4 barrier walls with epoxy-coated steel in the deck; however, justifying the total replacement of steel with

GFRP in barrier-deck overhangs needs further investigations, particularly with respect to the complex behaviour (level of confinement, termination of bars) of the deck-barrier joint.

Therefore, the overarching objective of this thesis is two-fold: justifying the replacement of steel with GFRP in single-slope Alberta TL-4 barriers by evaluating a total GFRP-RC system as well as assessing the efficiency of the doweling repair technique on these barriers.

3 ASSESSMENT OF REPAIR TECHNIQUES FOR GFRP REINFORCED BRIDGE BARRIERS USING VECTOR2[1]

3.1 CHAPTER INTRODUCTION

Glass fibre reinforced polymer (GFRP) bars have emerged as an alternative to traditional steel reinforcement in concrete structures. GFRP reinforcement is particularly useful in infrastructure applications due to its superior corrosion resistance relative to steel (Ahmed et al. 2011). Moreover, GFRP is a feasible and practical replacement for steel rebar in bridge construction, particularly in bridge decks and barriers, based on its structural performance and cost-effectiveness (El-Salakawy and Islam 2014). The use of GFRP bars in reinforced concrete bridge deck slabs and barriers has significantly increased in Canada (Ahmed et al. 2013).

There are six different performance/test levels of barrier walls, namely Test Level 1 (TL-1) to Test Level 6 (TL-6). The design and selection of a bridge barrier is based upon an exposure index that depends on traffic conditions, surrounding environment, the expected frequency and consequences of vehicle accidents, and bridge site. The required minimum test level is selected based on two major factors: the barrier's minimum height and its structural adequacy (impact resistant). Among those types, TL-4 is the most used type on Alberta highways and was investigated in this thesis. In static testing of a TL-4 traffic barriers, CSA S6-14 requires that the barrier wall should be able to resist a transverse load of 100 kN applied over a barrier length of 1050 mm at a height of 700 mm above the deck. Moreover, the minimum height of the barrier wall should be 800 mm (CSA 2014a). Nevertheless, both Canadian Standards Association (CSA) S6-14 (the Canadian Highway Bridge Design Code (CHBDC)) and American Association of State Highway and Transportation Officials (AASHTO) design specifications (2007) specify that bridge barriers should be crash-tested to evaluate their overall performance. However, both codes allow using specified static monotonic loads equivalent to vehicle impact to start the design of reinforcement and anchorage of bridge barrier wall-deck overhang (CSA 2014a) (AASHTO 2007). Although CSA S6-14 provides guidelines on designing concrete bridge barriers reinforced with GFRP bars, it does not provide guidelines on repairing or rehabilitating concrete bridge barriers

[1] Chapter 3 of this thesis has been published, aside from minor formatting edits, as Aljaaidi, A. and Tomlinson, D. "Assesment of Repair Techniques for GFRP Reinforced Barriers using VecTor2" in the proceedings of the 2019 Canadian Society for Civil Engineering Conference in Laval, Quebec. I was responsible for the model development and analysis as well as the manuscript composition. D. Tomlinson was the supervisory author and was involved with concept formation and manuscript composition.

reinforced with GFRP bars in case of damage caused by factors such as: exposure to freeze-thaw or wet-dry cycles, poor quality construction, poor design details, inadequate maintenance, changes in level of service, and vehicle collision. Bridge barriers, due to their primary function to reduce consequences of vehicles leaving the roadway, are susceptible to local damage and excessive cracking caused by vehicle impact. This poses concerns regarding the feasibility and economics of repairing concrete bridge elements reinforced with FRP. El-Salakawy et al. (2010) investigated the feasibility and effectiveness of repairing GFRP reinforced slabs and addressed two major questions: (1) what is the most suitable concrete demolition technique that causes minimal damage to the GFRP bars, and (2) how effective is this technique in terms of the flexural strength and load-transfer efficiency of concrete slabs. It was concluded that traditional concrete demolition techniques such as jackhammering and hydro-demolition resulted in severe damage to the existing GFRP reinforcement which rendered it inadequate to resist tension. Therefore, it was recommended that the damaged concrete be saw-cut for the full-depth removal of concrete, and the interrupted reinforcement should be replaced with new FRP bars using either the planting (splicing) or the Near-Surface Mounting (NSM) technique.

El-Salakawy et al. (2014) then tested two barrier repair techniques (planting and NSM) on double slope performance level two (PL-2) barriers. Both techniques showed satisfactory structural performance. Nevertheless, executing them in practice for long bridge segments requires considerable time and effort due to the drilling involved at tight spacings to splice the original bars to new ones, or saw-cutting grooves on the concrete surface to install NSM bars. The overall objective of this chapter is to investigate the efficiency, practicality, and cost-effectiveness of two new repair techniques for bridge barriers reinforced with GFRP.

Both techniques involve saw-cutting to remove damaged barrier walls, and then drilling holes into the overhang deck slabs to plant single-headed GFRP bars which transfer impact loads from the barrier wall to the overhanging deck slab. GFRP bent bars have been used in the past to provide sufficient anchorage at the barrier wall-deck interface. However, because of the direction and rearrangement of the fibres in the bend the tensile capacity is significantly reduced. For instance, the ultimate tensile strength of GFRP bars with 50 GPa modulus of elasticity decreases from 1000 MPa to 450 MPa (45% reduction) at the bent portion compared with the straight portion of the bars (TUF-BAR Canada 2019). Azimi et al. (2014) studied the anchorage sufficiency of the proposed barrier wall-deck slab connection reinforced with single-headed GFRP bars and

concluded that these bars can be used in bridge barrier walls to resist the applied vehicle impact load specified in the CSA S6-14 at the barrier wall-to-deck slab junction. Nevertheless, they used a different orientation of single-headed GFRP bars than the one proposed in this project with the head of the GFRP bars embedded in the deck. It is worth mentioning that they tested Performance level 2 and 3 (PL-2 and PL-3) types of barriers with single and double sloped barrier walls.

3.2 METHODOLOGY

The modelling presented in this chapter is comprised of two phases. The first phase includes the assessment of the as-built bridge barriers using VecTor2. In this phase, test level 4 (TL-4) single slope bridge barrier prototypes conforming to the detailing scheme (same layout and spacing of bars) of a successfully crash-tested steel reinforced concrete bridge barriers commonly used in Alberta (Figure 3.1(a)) are modeled with steel and GFRP as reinforcement in FormWorks (a pre-processor software for VecTor2) (Figure 3.1(b)). One model is reinforced with steel, to be used as a control model, while the others are reinforced GFRP reinforcement, which are yet to be crash-tested. These models are analyzed by utilizing displacement-controlled loading at a height of 690 mm above the deck slab, which represent an equivalent static load, using VecTor2 software. The results are then analyzed using Augustus (a post-processor software for VecTor2).

The second phase is the assessment of the repair techniques for GFRP reinforced bridge barriers using VecTor2. In this phase, single-headed GFRP bars are used as connections between the deck slab and the barrier wall to transfer the loads. The layers of GFRP bars in the barrier wall are terminated at the interface of barrier wall and the deck slab to reflect the saw-cutting of the previous GFRP bars. The spacing, diameter, and embedment depths of the anchorage systems are the main parameters investigated in the repair technique.

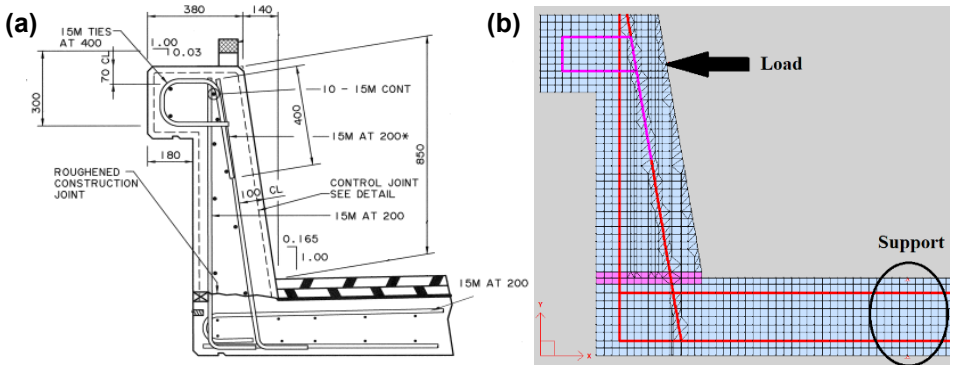

Figure 3.1: Bridge Barriers showing (a) Alberta TL-4 design (Alberta Transportation 2017), (b) Alberta TL-4 (VecTor2 Model).

3.2.1 Repair Techniques

Two techniques were utilized to repair the damaged bridge barrier walls. Both techniques involve saw-cutting to remove the damaged barrier walls, and then drilling holes into the overhang deck slabs to plant single-headed GFRP bars which transfer impact loads from the barrier wall to the overhang deck slab. Epoxy is injected in the drilled holes before the placement of GFRP bars to hold them in place and transfer loads. The difference between these techniques is that in one repair technique a single-assembly of GFRP bars is used on the traffic side of the barrier wall to reinforce Fibre-Reinforced Concrete (FRC) (Figure 3.2(a)). In the other technique, a double-assembly of GFRP bars will be utilized to reinforce plain concrete (Figure 3.2(b)).

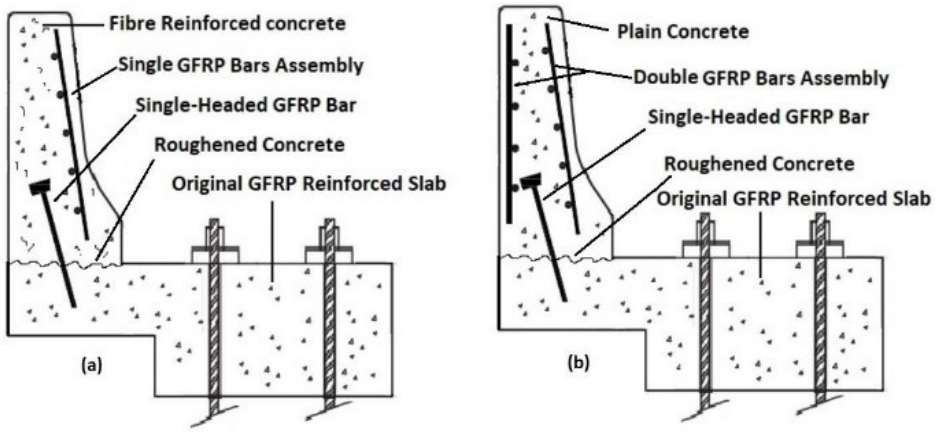

Figure 3.2: Repair techniques (a) FRC with single assembly, (b) Plain concrete with double assembly.

3.2.2 Model Description

3.2.2.1 VecTor2 Overview

VecTor2 is a non-linear finite element program developed at the University of Toronto for the analysis of two-dimensional reinforced concrete membrane structures. VecTor2 can be used to assess the structural performance of reinforced concrete in terms of strength, post-peak behaviour, failure mode, deflections, and cracking using non-linear constitutive models for reinforced concrete and reinforcement. VecTor2 uses the Modified Compression Field Theory and the Disturbed Stress Field Model to predict the response of reinforced concrete elements. It utilizes an incremental total load, iterative secant stiffness algorithm to complete nonlinear analysis (Wong et al. 2013).

FormWorks preprocessing software helps in using VecTor2 by decreasing the potential for input error and expediting the modeling process through a graphical interface for data input and

visualization in the Windows environment. After the analysis is done using VecTor2, Augustus software provides graphical post-processing capabilities for the analysis results.

3.2.2.2 Bridge Barrier Model Details and Material Properties

The barriers and overhangs were modeled using 2-D plane membrane elements (plane stress condition). The maximum mesh sizes were taken as 25 × 25 mm, with an aspect ratio of 1.5. A representative FEA model is illustrated in Figure 3.1. The thickness of the elements was 1000 mm which represents the width of the barrier overhang (i.e. results are provided for a metre unit width of barrier/deck). The models are defined using three regions of concrete: One region represents the deck slab, another represents the barrier wall, and the third one represents the interface between the deck slab and the barrier wall. The support condition was taken as four pin supports in pairs at 1000 mm apart, one pair of them at 500 mm from the end of the deck. This support condition is representative of the support condition expected in the lab. This support condition also represents the expected support conditions provided by girders in actual bridges.

Three models were built with different reinforcement to represent as-built conditions. All models had concrete cover of 40 mm for the slab, 100 mm for the front face of the barrier wall, and 75 mm for the back face of the barrier wall. In addition, they had a bar spacing of 200 mm. One model was totally reinforced with 15M steel bars (area per bar is 200 mm^2), the second one was reinforced with 15M GFRP bars, the third one was reinforced with 20M GFRP bars (area per bar is 300 mm^2).

Concrete was modelled using Hognestad model for pre-peak compression, Modified Park-Kent model for post-peak compression, Vecchio 1992-A model for compression softening, Modified Bentz 2003 model for tension stiffening, and linear tension softening model. The concrete compressive strength is 35 MPa and tensile strength is 1.95 MPa. The concrete is normal density (2400 kg/m^3) with a maximum aggregate size of 10 mm.

For the barrier walls repaired with fibre-reinforced concrete FRC, hooked steel fibres with 1050 MPa tensile strength are used. Their length and diameter are 60 mm and 0.75 mm, respectively. And the fibre volume fraction used is 1%. The Simplified Diverse Embedment Model (SDEM) for monotonic loading conditions is used to consider the contribution of steel fibre reinforcement to concrete tensile strength.

Steel reinforcement was modelled with a 400 MPa yield strength, 600 MPa ultimate strength, and a 200 GPa modulus of elasticity. The ultimate tensile strain is 10% and the strain hardening

strain is 1.2%. GFRP bars was modelled as linear-elastic until failure with a 1200 MPa ultimate strength, 60 GPa modulus of elasticity, and 10% ultimate tensile strain. These GFRP properties are representative of high modulus GFRP bars available from manufacturers. GFRP single-headed bars have the same material properties as straight bars.

3.2.2.3 Analysis

All models were loaded, as described earlier, under an increasing monotonic displacement until a specified displacement of 60 mm. Each model consisted of 61 load (displacement) stages. The first stage started with zero displacement which represented the origin point (0, 0), and then the displacement proportionally increased by a common factor of 1 mm from one load stage to the next. A load step of 1 mm displacement was chosen to allow the solution to properly converge in a fewer number of iterations before the analysis proceeds to the next load step since the improper convergence may overestimate the strength for the imposed displacement which might misrepresent the overall softening response of concrete. To control the quality of the analysis and to ensure that it resembles the experimental testing in the lab, a Static Nonlinear-Load Step analysis is chosen, a maximum number of 60 iterations of was set, and a convergence limit of 1.00001 was applied in the Analysis Parameters Group.

3.2.3 General Considerations

CSA S6-14 and the AASHTO Load and Resistance Factor Design (LRFD) codes do not provide any specific guidance for acceptable horizontal deflection of the barrier wall caused by vehicle impact. Hence, the ultimate load carrying capacity was used as the main parameter to evaluate the structural performance of the barrier overhang and the different repair techniques. However, new designs of bridge barriers should be crash tested. In the case of dynamic testing, greater horizontal deflection of the barrier wall may play a favourable role in absorbing energy of vehicle impact caused by the nonlinearity of concrete (Azimi et al. 2014).

3.3 RESULTS AND DISCUSSION

3.3.1 Comparison between Steel- and GFRP-reinforced as-built bridge barriers

The model of the bridge barrier reinforced with steel exhibited a ductile behaviour with high deflection at the maximum load (Figure 3.3). The ultimate load capacity was 100 kN (all capacities are per metre length of barrier) with a horizontal deflection of 40 mm at the point of load application. However, GFRP-RC models (both 15M and 20M) showed lower deflections at lower

loads. For instance, when 15M bars were used the ultimate load carrying capacity was 79.3 kN with a horizontal deflection of 29.8 mm at the point of load application. In the case of using 20M bars, the ultimate load carrying capacity was 92.1 kN with a horizontal deflection of 24.8 mm. The design of bridge barriers is an extreme event limit state, therefore, using 20M GFRP bars in TL-4 bridge barriers could be a viable option since its model achieved 101% of the ultimate load carrying capacity (at yield) of its counterpart model reinforced with steel.

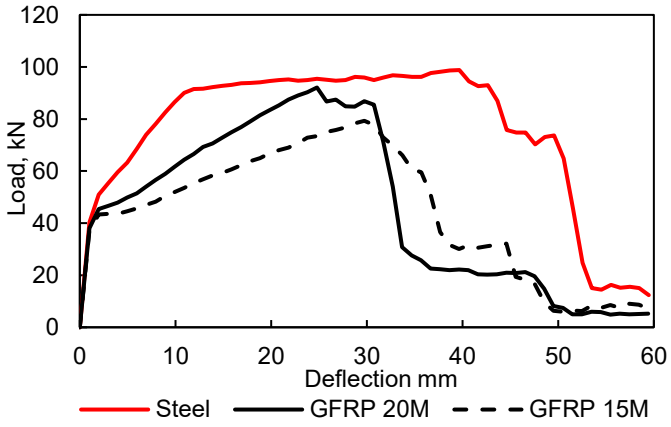

Figure 3.3: Comparison between Steel and GFRP reinforced models.

3.3.2 Comparison between the proposed repair techniques

The models of the repair techniques on GFRP bridge barriers reinforced with 15M bars at a spacing of 200 mm are compared against the as-built model. The model of the repaired barrier using FRC with single assembly of GFRP bars and single-headed GFRP bars resisted a maximum load of 75.9 kN at a horizontal displacement of 26.8 mm when the GFRP single-headed bars were spaced at 200 mm and 81% embedded in the deck slab. On the other hand, the model of the repaired barrier using plain concrete with double assembly of GFRP bars resisted a maximum load of 74.4 kN at a horizontal displacement of 28.2 mm when the GFRP single-headed bars were spaced at 200 mm and 81% embedded in the deck slab. Both repair techniques models had load carrying capacity lower than the model of the as built barrier which resisted a maximum load of 79.3 kN at a horizontal displacement of 29.8 mm (Figure 3.4). However, the difference is fairly small (roughly 5%). The repair technique using FRC achieved a slightly higher capacity due to the presence of steel fibres which help in resisting the tensile stresses in concrete. It is worth mentioning that repairing barriers using FRC with single assembly of GFRP bars requires less time and effort compared to using RC with double assembly of GFRP bars. Table 3.1 shows sample results of the

repaired models, using both techniques with GFRP single-headed bars (15M and 20M) spaced at 200 mm and embedment ratio of 81% for both GFRP reinforcement schemes (15M and 20M).

Table 3.1: Ultimate load carrying capacity and deflection at maximum load of repaired models.

Model	Strength, kN	% of As-built model	Deflection at max load, mm
GFRP 20M (As-built)	92.1	100 (reference)	24.8
GFRP 20M FRC repaired	93.7	101.8	27.8
GFRP 20M RC repaired	88.8	96.4	23
GFRP 15M (As-built)	79.3	100 (reference)	29.8
GFRP 15M FRC repaired	75.9	95.7	26.8
GFRP 15M RC repaired	74.4	93.8	28.2

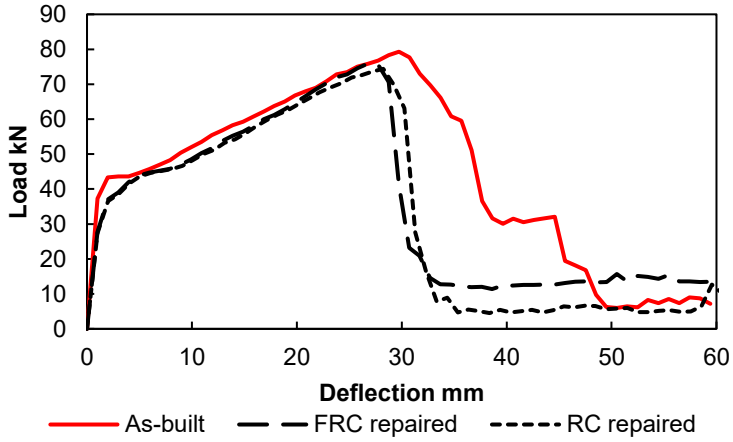

Figure 3.4: Comparison between the proposed repair techniques

3.3.3 Parametric study on one of the repair techniques using VecTor2

A parametric study was carried out to investigate the effect of some parameters on the effectiveness of one of the proposed repair techniques, plain concrete reinforced with double assembly of 15M and 20M GFRP bars spaced at 200 mm and repaired with 15M and 20M GFRP anchorage system at different spacing, on the overall performance of the repaired barriers. The undamaged 20M GFRP bridge barrier model was used as a reference for evaluating the performance of the repaired GFRP bridge barriers models after it had proven a satisfactory behaviour compared to its steel-reinforced counterpart. The spacing, s, diameter, d_b, and embedment depth percentage, $E\%$, of the anchorage system were the main parameters investigated. The associated values for each parameter were taken as: s (100, 150, and 200 mm), d_b (15 mm, and 20 mm), and $E\%$ (50, 81 (embedded to the level of bottom reinforcement of the deck slab), and 100 (full depth embedment) %). FEA models were built to represent single-sloped TL-4 Alberta Transportation RC barriers, which are one of the most common barriers used in Alberta. Thirty 2-D finite element models were

constructed with different parameters and then subjected to a monotonic displacement loading at a height of 690 mm above the deck level (250mm) as shown in Figure 3.1(b).

Representative results obtained from FEA are shown in Figures 3.5 and 3.6, illustrating the effect the spacing, diameter, and embedment depth percentage of the GFRP single-headed bars on the ultimate load capacity *P*. The results of all of the models are shown in Table 3.2, including the corresponding horizontal displacement at the loading level (940 mm). The model ID includes: reinforcement material used, main reinforcement diameter, condition, single-headed GFRP bars diameter, spacing, and embedment ratio, in this order. The as-built GFRP model reinforced with 20M bars as main reinforcement is used as a reference since it exhibited a comparable load carrying capacity to its steel-reinforced counterpart (at yield).

Table 3.2: Ultimate load carrying capacity and deflection at max. load of the models.

Model ID	Strength, kN	% of reference model	Deflection at max load, mm
GFRP 20M (As-built) (Reference)	92.1	100	24.8
GFRP 15M (As-built)	79.3	86	29.8
Steel 15M (As-built)	91.6 (Yield)	99.5	12.9
GFRP 20M (20M - 100% - 100 mm)	126.9	138	38.7
GFRP 20M (20M - 100% - 150 mm)	118.9	129	40.6
GFRP 20M (20M - 100% - 200 mm)	111	120.5	36.7
GFRP 20M (20M - 81% - 100 mm)	94.5	102.6	27
GFRP 20M (20M - 81% - 150 mm)	90.3	98	27
GFRP 20M (20M - 81% - 200 mm)	88.8	96.4	23
GFRP 20M (20M - 50% - 100 mm)	71.5	77.6	16.7
GFRP 20M (20M - 50% - 150 mm)	70.6	76.7	18.7
GFRP 20M (20M - 50% - 200 mm)	70.4	76.4	18.7
GFRP 15M (20M - 100% - 100 mm)	105.2	114	42.6
GFRP 15M (20M - 100% - 150 mm)	94.6	102.7	40.6
GFRP 15M (20M - 100% - 200 mm)	92.9	101	40.6
GFRP 15M (20M - 81% - 100 mm)	83	90	29
GFRP 15M (20M - 81% - 150 mm)	78.3	85	27
GFRP 15M (20M - 81% - 200 mm)	73.6	80	25.2
GFRP 15M (20M - 50% - 100 mm)	63.6	69	18.7
GFRP 15M (20M - 50% - 150 mm)	61.4	66.7	20.6
GFRP 15M (20M - 50% - 200 mm)	58.9	64	18.7
GFRP 15M (15M - 100% - 100 mm)	101	109.7	43.6
GFRP 15M (15M - 100% - 150 mm)	92.7	100.7	40.6
GFRP 15M (15M - 100% - 200 mm)	85.6	93	37.7
GFRP 15M (15M - 81% - 100 mm)	80.2	87	28.2
GFRP 15M (15M - 81% - 150 mm)	76.3	83	27.2
GFRP 15M (15M - 81% - 200 mm)	74.4	80.8	28.2
GFRP 15M (15M - 50% - 100 mm)	63.0	68.4	18.7
GFRP 15M (15M - 50% - 150 mm)	59.4	64.5	19.7
GFRP 15M (15M - 50% - 200 mm)	59.4	64.5	19.7

3.3.3.1 Effect of headed bar spacing

For all the embedment ratios using single-headed 15M GFRP bars, the ultimate load carrying capacity was affected by the spacing. For instance, for the barrier with 15M single-headed bars and 81% embedment ratio, capacity increased by 7.8% from 74.4 kN to 80.2 kN when the spacing decreased from 200 mm to 100 mm. However, the ultimate capacity was unaffected by the change in spacing from 200 mm to 150 mm when the embedment ratio was 50%. Nevertheless, the ultimate capacity was increased when the spacing was decreased from 150 mm to 100 mm.

3.3.3.2 Effect of headed bar diameter

In the case of different diameters of single-headed GFRP anchorage while fixing the spacing, the ultimate load carrying capacities observed were comparable for different diameters at lower embedment ratios, however, the model repaired with the larger diameter (20M) showed higher capacity at higher embedment ratios. Again, this was caused by the failure mode. Since the larger diameter needs a longer depth of embedment to develop its capacity, it showed higher capacity at the higher end of embedment ratio compared to the smaller diameter (Figure 3.6 (a) and (b)).

3.3.3.3 Effect of headed bar embedment depth

For the same diameter of single-headed GFRP anchorage and the same spacing, the ultimate load carrying capacity increased with the increased embedment ratio due to the pull-out failure mode. Moreover, the displacement associated with the maximum load also increased with the increased embedment ratio for the same reason. Unlike the consistent relationship between the spacing and the ultimate load carrying capacity across different embedment ratios, there was no common trend in the change in the displacement at the maximum load capacity at different spacings across different embedment ratios.

3.3.3.4 Comparison between repaired and as-built models

In comparison with the as built capacity, the models of barriers repaired 15M bars planted for the full depth (100%) achieved higher capacities than the model of the as built barrier as shown in Figure 5 (a). On the other hand, the models in which the embedment ratio was 50% achieved lower capacities, for example, the reduction in strength was 20.6% at a spacing of 100mm (Figure 3.5 (a)). However, when the same spacing used with 81% embedment ratio, the capacity achieved was slightly higher than the as built model.

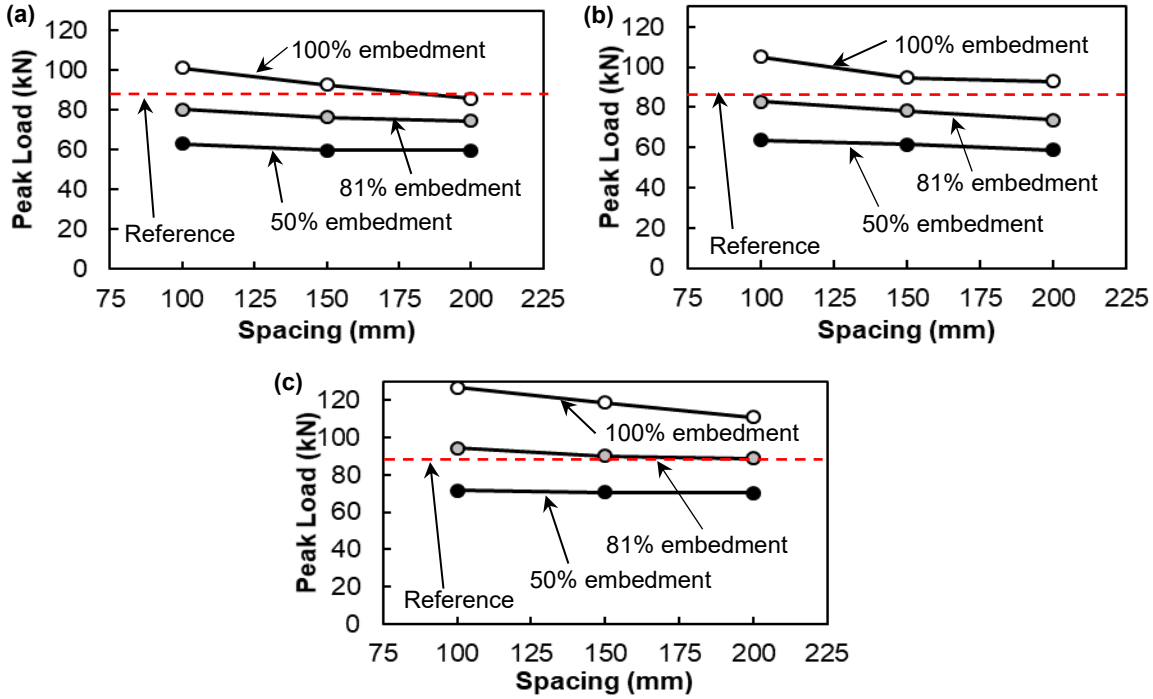

Figure 3.5: Effect of bar spacing on barrier peak load (a) 15 mm GFRP retrofit on 15M reinforced barrier (b) 20 mm GFRP retrofit on 15M reinforced barrier (c) 20 mm GFRP retrofit on 20M reinforced barrier.

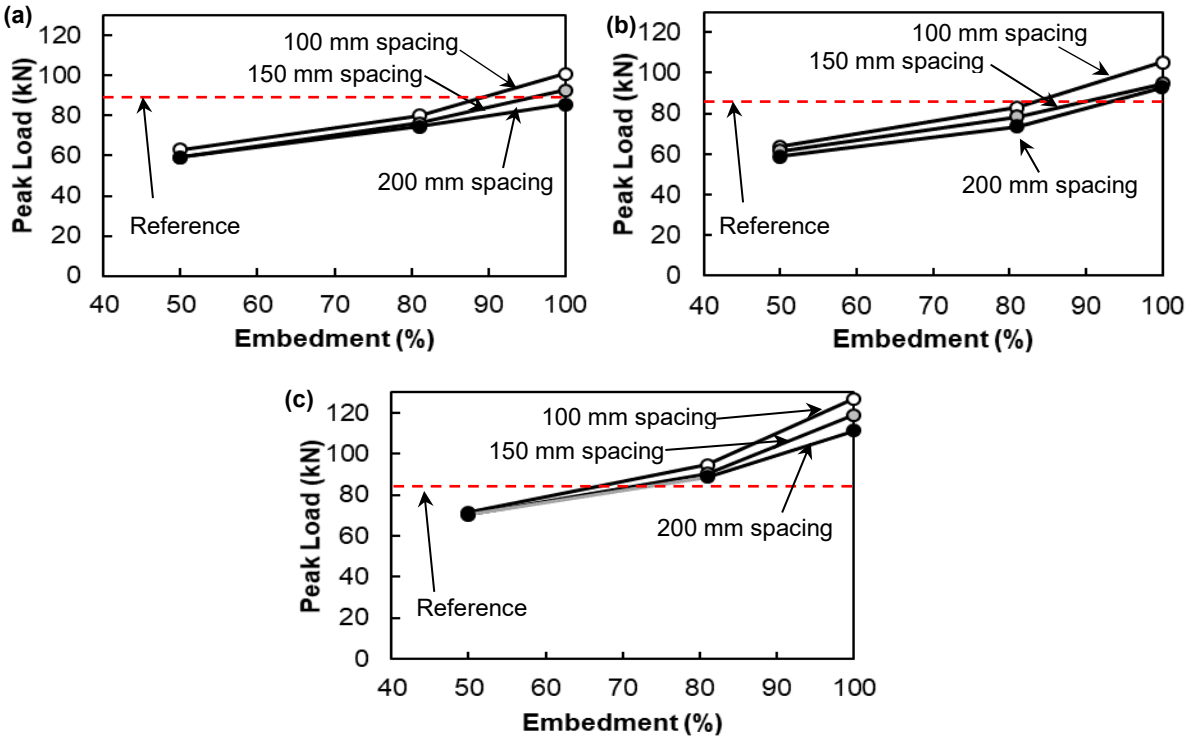

Figure 3.6: Effect of embedment ratio on barrier peak load for (a) 15 mm GFRP retrofit on 15M reinforced barrier (b) 20 mm GFRP retrofit on 15M reinforced barrier (c) 20 mm GFRP retrofit on 20M reinforced barrier.

3.4 CHAPTER CONCLUSIONS

Based on the findings obtained from VecTor2 set of models (32) on the behaviour of the steel-reinforced barriers, GFRP-reinforced barriers, and the barriers with the proposed repair techniques, and after studying the effect of changing some parameters on the design (diameter of GFRP reinforcing bars, and diameter of GFRP anchorage (single-headed bars), their spacing, and embedment ratio), the following conclusions can be drawn:

- Reinforcing barriers with GFRP bars using 20M bars is a viable option since it achieved 92.1% of the ultimate load carrying capacity of its counterpart model reinforced with steel.
- Both repair techniques proved to be effective when the GFRP single-headed bars embedded across the full depth of the deck slab. They achieved an ultimate load carrying capacity higher than the one achieved by the undamaged barrier.
- In general, increasing the embedment ratio of the GFRP headed bars increases the strength of the repaired barriers.
- The effect of decreasing the spacing of GFRP single-headed bars on the strength of the repaired barriers is affected by the embedment ratios. For higher embedment ratios, the effect is maximized. In contrary, when the embedment ratio is low, the effect diminishes.
- The most efficient repair technique is using FRC and a single assembly of GFRP bars which achieved an ultimate load carrying capacity comparable to the one achieved by the as-built GFRP barrier while utilizing only one assembly of bars in the barrier wall. S
- The recommended design to replace the TL-4 Alberta steel-reinforced bridge barrier design is the 20M GFRP reinforced bridge barrier design instead of the equivalent reinforcement ratio design presented in the 15M GFRP reinforced bridge barrier.

4 CHAPTER 4: EXPERIMENTAL PROGRAM[2]

4.1 Chapter Introduction

Proposed barriers are typically tested in three ways to determine their ultimate load capacity and failure mode: crash testing, impact pendulum testing, and static (monotonic) testing. Beyond their initial design and construction, the structural integrity and overall performance of barriers (and bridges in general) is compromised by factors such as environmental deterioration (e.g. de-icing salts) and extreme loads (e.g. impact). Damages due to corrosion related issues in bridges result in significant direct and indirect costs, estimated to be around 13.6 billion dollars in Canada according to a 2005 study (Shipilov 2009). Fatalities caused by catastrophic bridge collapses are even far greater, incalculable cost.

FRP reinforcement, especially GFRP, has emerged as an alternative to traditional steel reinforcement in RC structures. FRP reinforcement's properties make them suitable for specific applications. For instance, their noncorrosive nature makes them useful in structures exposed to corrosive environments and its nonconductive behaviour makes it useful for structures containing equipment sensitive to electromagnetic fields. Although FRP reinforcement has higher strength-to-weight ratio compared to conventional reinforcement, it has a linear-elastic tensile response up to failure (i.e. brittle failure). Over the 21st century, the use of GFRP bars in reinforced concrete bridge deck slabs and barriers has significantly increased in Canada (Ahmed et al. 2013), attributed to GFRP's corrosion resistance, high strength, and reasonable economical cost compared to other types of fibres (Ahmed et al. 2011). GFRP is a feasible and practical replacement for steel in bridge decks and barriers (El-Salakawy and Islam 2014).

Two of the earliest approved GFRP-RC barrier-deck overhang designs in Canada were introduced by El-Salakawy et al. (2003). Those double-slope GFRP-RC PL-2 and PL-3 barrier designs were tested under static load and pendulum impact load. Their behaviour was comparable to steel-RC counterparts in terms of cracking, deflections, strains, energy absorption, integrity, and ultimate strength. Since barriers by nature are susceptible to damage and excessive cracking caused by factors such as vehicle impact,, El-Salakawy et al. (2010) and El-Salakawy et al. (2014)

[2] *As mentioned in Section 1.3.1, all structural testing facilities at the University of Alberta were shutdown for over seven months due to the COVID-19 pandemic. This shutdown prevented me from completing the proposed experimental program presented in this chapter. The presented information is given to provide background and methodology for the testing which will be presented in a future student's thesis.*

explored different options to repair damaged GFRP-RC slabs and barriers. Two repair techniques were conceived from this research, and it was recommended that the damaged concrete be saw-cut for the full-depth removal of concrete, and the interrupted reinforcement be replaced with new FRP bars using either the planting or the NSM technique. Both repair techniques showed satisfactory structural performance under static testing.

Although El-Salakawy et al. (2014)'s work provides feasible and efficient repair techniques for GFRP bridge barriers, further testing is required to investigate the efficacy of those repair techniques on different barrier configurations and reinforcement schemes, and longer, more realistic, overhang lengths. To address this gap in research, this thesis investigates the efficiency of using the planting repair technique on single-slope Alberta TL-4 barriers reinforced with GFRP. This barrier type has never been reinforced totally with GFRP as the main reinforcement. Ahmed et al. (2010) explored using GFRP in the barrier wall with epoxy-coated steel in the deck slab; however, justifying the total replacement of steel with GFRP in barrier-deck overhangs needs further investigations. Therefore, the overarching objective of this thesis is two-fold: justifying the replacement of steel with GFRP in single-slope Alberta TL-4 barriers, and assessing the efficiency of applying the planting repair technique on them, and on single-slope GFRP barriers in general.

4.2 PROPOSED EXPERIMENTAL PROGRAM

4.2.1 Barrier Description

The design and selection of a bridge barrier test level is predicated on an exposure index that depends on traffic conditions and bridge site requirement. A chosen test level implies a required minimum barrier height and impact load capacity. Single-slope Alberta TL-4 barriers (Figure 2.4) are commonly used in Alberta, Canada. These barriers have heights of 840 mm and are designed to resist factored transverse loads 170 kN, applied over a barrier length of 1050 mm at a height of 700 mm above the deck slab. A TL-4 barrier design is chosen in this thesis for its wide use in bridge construction across Canada. Nevertheless, the outcomes of this research may be extended to other test levels of barriers with a similar design (i.e. similar configuration of reinforcement and anchorage to deck slab).

Typical AT single-slope TL-4 barrier parapets have a base depth of 355 mm and a top depth of 200 mm plus a 180 mm protrusion to the back of the parapet which resembles a spandrel beam that is 300 mm in height. This protrusion provides extra stiffness and strength to the barrier, in

two-way action which is beyond the scope of this thesis. Alberta TL-4 RC barriers are typically cast using ready-mixed normal weight concrete with a target compressive strength of 45 MPa.

The proposed length of the tested deck slab is 2400 mm, with an overhang length of 1500 mm, a 600 mm length contained between two HSS steel supports, and a 300 mm of slab extending beyond the support. A 1500 mm overhang length is longer than the 1000 mm length tested in previous barrier test programs and was selected to better reflect common practice in the industry and to provide a more realistic behaviour and results.

4.2.2 Test Specimens

The first stage of the proposed testing addresses the feasibility of replacing steel with GFRP reinforcement while the second stage investigates the efficiency of proposed repair techniques in restoring repaired bridge barrier overhangs. The evaluation in the first stage is based on the overall behaviour of the barrier-deck overhang (i.e. ultimate load capacity, failure mode, deflections, and reinforcement strains) under static loading. In the second stage, the comparison is based on the difference in the ultimate load capacity between the repaired specimens and a reference specimen, under static loading as well. This thesis project proposes five barrier-deck overhang specimens (two as-designed specimens and three repair specimens), as shown in Table 4.1.

Table 4.1: Test specimens

Specimen	Deck Reinforcement	Parapet Reinforcement	Repair Technique	Repaired Section
DS	Steel*	Steel	N/A	N/A
DG	GFRP	GFRP	N/A	N/A
RG-P	GFRP	GFRP	Doweling	Parapet
RG-D	GFRP	GFRP	Doweling	Deck
RH-P	Steel	GFRP	Doweling	Parapet

* Standard 180°hook (top transverse reinforcement) as per Alberta Transportation requirements.

A baseline barrier-deck overhang designated (DS) complying with the detailing and design of steel-RC Alberta Transportation TL-4 barriers (Figure 4.1a) is used as a reference to assess the performance of GFRP-RC barriers and barriers simulating proposed repair techniques. The deck slab of DS is reinforced with four layers of reinforcement, two transverse and two longitudinal (i.e. traffic direction). The top assembly of reinforcement has 20M steel rebar with 180° hooks placed at the barrier/deck interface at 150 mm spacing as transverse reinforcement, and 15M steel rebar at 200 mm spacing for longitudinal reinforcement. Due to slab thickness limitations, the hooked rebar is tilted along a plane perpendicular to the transverse reinforcement to allow for a

top concrete cover of 50 mm and a bottom concrete cover of 40 mm. The bottom assembly is comprised of 15M transverse steel rebars at 150 mm spacing, and 15M longitudinal steel rebars at 200 mm spacing.

The barrier parapet has two assemblies of rebar, front and back, plus bent rebar in the protruded beam-like block. The front assembly is constructed with vertical 15M bent steel rebar at 150 mm spacing, and five horizontal 15M steel rebars at 150 mm spacing with a concrete cover of 60 mm. The back assembly has a vertical layer of 15M bent steel rebar at a spacing of 300 mm, and a horizontal layer of four horizontal 15M steel rebar at a spacing of 150 mm with a clear concrete cover of 60 mm. The beam-like block at the top of the barrier parapet is reinforced with 15M bent, tie-like steel rebar at 300 mm spacing, supported by two horizontal 15M steel rebar with top and bottom concrete covers of 50 mm, and a back concrete cover of 40 mm.

A second barrier-deck overhang specimen designated (DG) is reinforced with GFRP instead of steel (Figure 4.1b). DG has the same shape and dimensions, and the same reinforcement configuration and spacing as the steel-RC reference barrier (DS) with the exception of the reinforcement in the beam-like protrusion in which two bent pieces of GFRP bars are used instead of one tie-like piece, due to manufacturing difficulties. The pultrusion process for the manufacture of GFRP bars is a continuous process, and therefore it is not feasible to produce closed-shaped GFRP bars in the production line. The same detailing of rebar applies to all GFRP reinforced parapets. This specimen is compared to the reference steel-reinforced barrier (DS) to evaluate the suitability of replacing steel with the same reinforcement ratio of GFRP rebars, and the performance of GFRP as the main, sole reinforcement in AT TL-4 barriers. Moreover, it is used as a reference to assess the performance of the proposed repair techniques and their efficiency in restoring structural strength. In this specimen and other GFRP reinforced ones, 20M steel rebar is replaced with #6 GFRP bars (6/8 inch = 19.1 mm), and 15M steel rebars are replaced with #5 GFRP rebars (5/8 inch = 15.9 mm). These are the nominal diameters of GFRP bars according to the manufacturer.

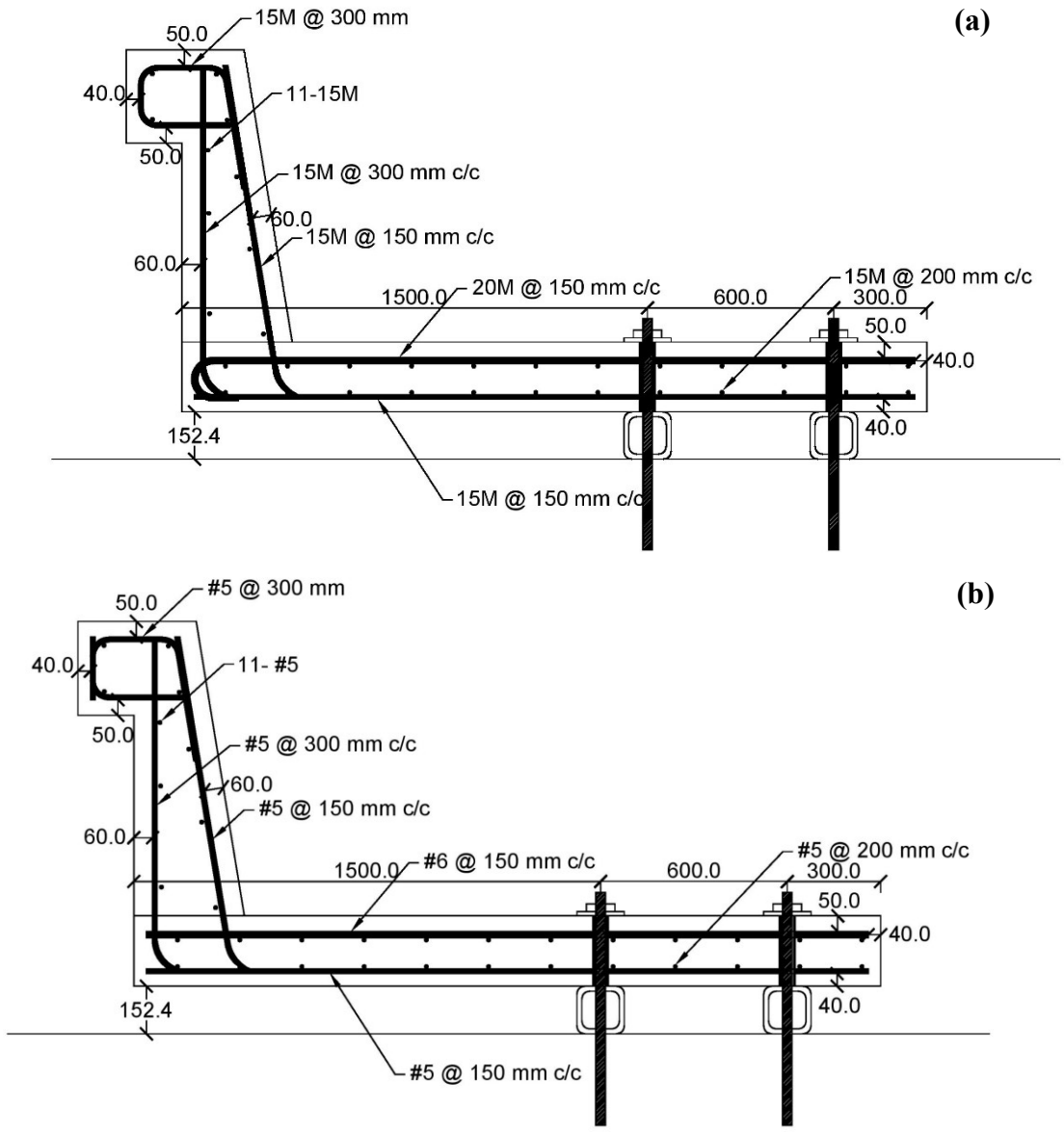

Figure 4.1: As-designed barrier test specimens (a) Specimen DS (b) Specimen DG.

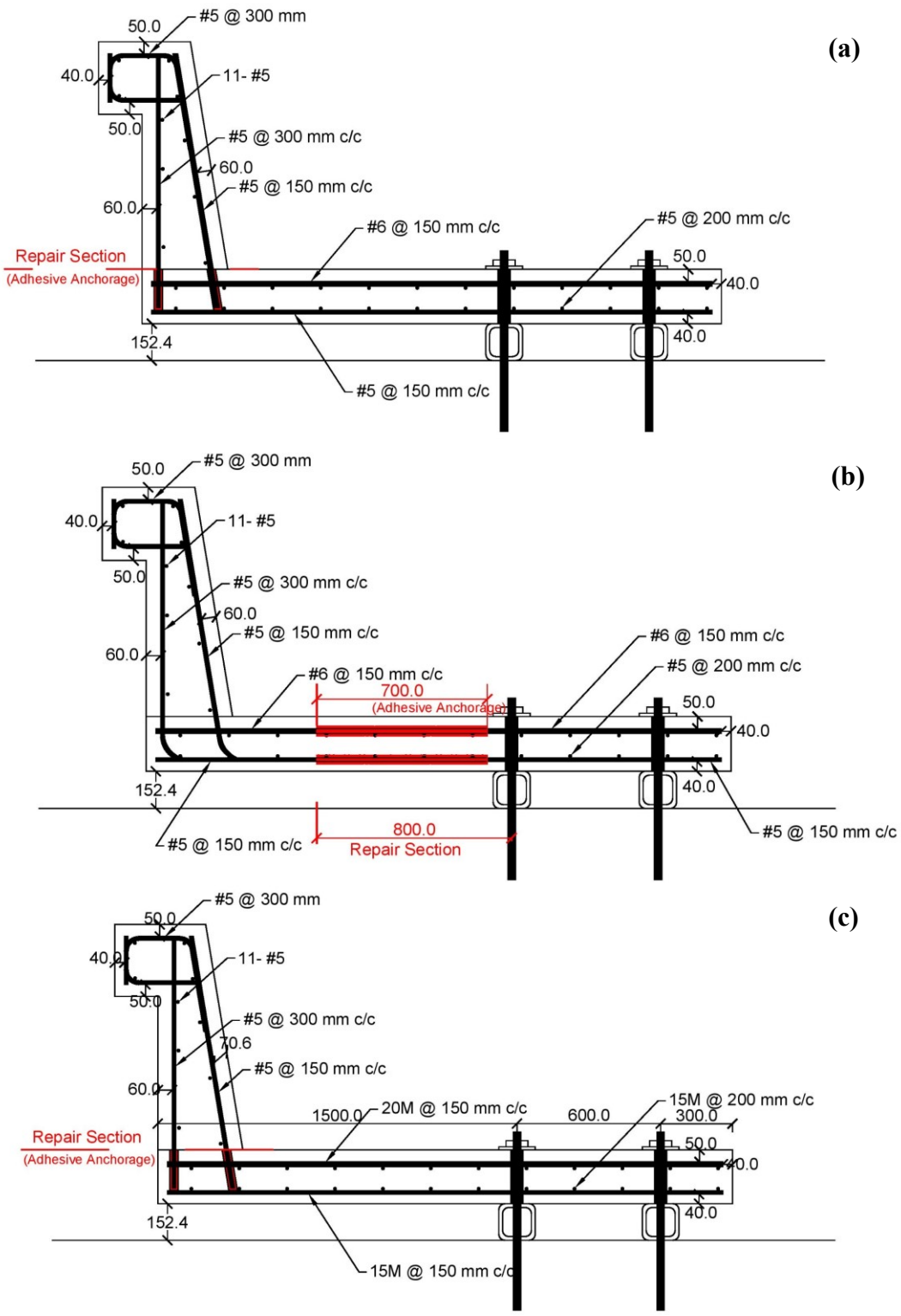

Figure 4.2: Barrier repair test specimens (a) Specimen RG-P (b) Specimen RG-D (c) Specimen RH-P.

Another GFRP reinforced barrier-deck overhang specimen (RG-P) is used to investigate a repair simulation of a damaged GFRP barrier (Figure 4.2a). Only wall damage is assumed in this case to represent damage restricted to the barrier parapet area, without extending to the deck slab.

A similar GFRP-RC barrier-deck overhang specimen (RG-D) is used to investigate a repair simulation of damaged GFRP barrier-deck overhang (Figure 4.2b). This case represents barrier damage that extends to the deck slab which requires demolition of concrete beyond the parapet level. Similar to the RG-P, damage will not be inflicted but assumed.

A fifth hybrid barrier-deck overhang specimen (RH-P) is used to assess the repair or retrofit of steel reinforced barrier-deck overhangs using GFRP reinforcement (Figure 4.2c). In this scenario, barrier damage or barrier upgrade is assumed at the parapet level. It is worth mentioning that the steel used in the transverse direction of the top mat is straight instead of hooked. This variable helps to study the influence of straight steel rebars on the performance of barrier-deck junction as opposed to using hooked rebars, as in specimen (DS).

Figure 4.3 shows the different shapes and sizes of vertical rebar used in the barrier walls of the test specimens. Figure 4.4 shows the sizes of transverse rebar used in the deck slabs of the test specimens. All GFRP and steel rebars are fabricated and procured. The bend radius of bent GFRP rebar is based on manufacturer best practice to avoid stress concentrations at the corners, and to reduce the loss in of rebar strength at the bend (bend strength).

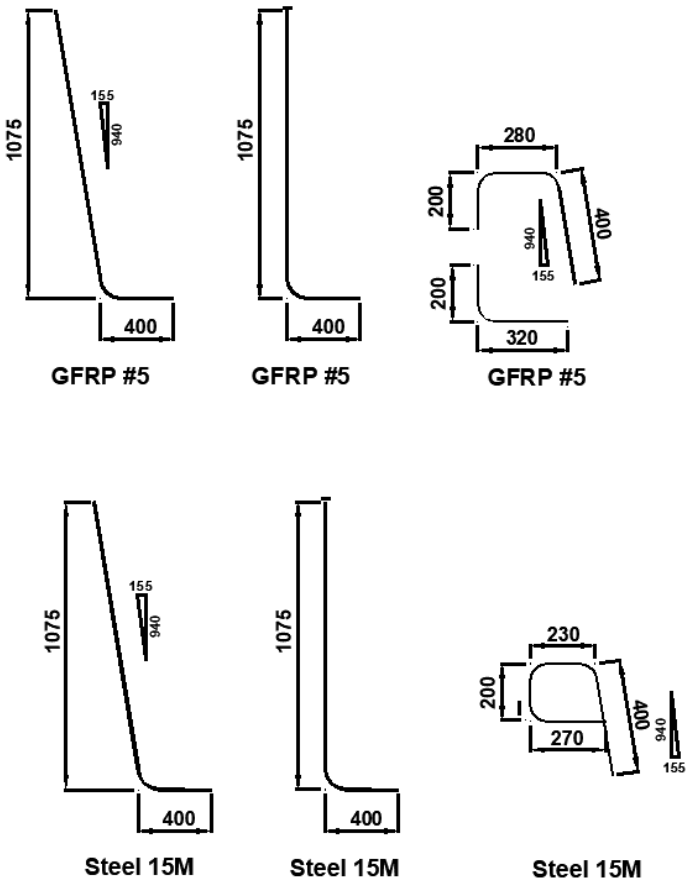

Figure 4.3: Barrier wall reinforcement layout. All dimensions in mm.

Figure 4.4: Deck slab reinforcement layout. All dimensions in mm.

4.2.3 Doweling Repair Technique

The doweling repair technique is proposed in repairing the bridge barrier specimens in this project. The specifics of this repair technique are inspired by El-Salakawy et al. 2010. There are four parameters associated with this repair method: bar hole diameter, centre-to-centre spacings of the bars, bonding agent, and embedment length. The recommended bar hole-diameter is 3-mm larger than bar diameter (23 mm for #6 GFRP bars and 19 mm for #5 GFRP bars), the recommended spacing of bars is three times the bar diameter (60 mm for #6 GFRP bars and 48 mm for #5 GFRP bars), the recommended bonding agent is Epoxy (Hilti RE 500), and the recommended embedment length is thirty-five times the bar diameter, when possible.

The general repair procedure for barriers is as follows:

- The damaged portion of the barrier/deck is cut off using a concrete saw.
- Holes are drilled into the sound concrete using a concrete drill (a rotary hammer drill in this case).
- Those holes are then cleaned off using an air blower to provide a clean surface for better bonding of doweled bars.
- The interface between the old and new concrete is chipped off using a rotary hammer with a chisel bit to roughen the interface and make it better concrete bonding.
- Epoxy adhesive is injected into the drilled holes using an injection gun, and then doweled bars are inserted into those holes.
- After doweling the repair bars, the new reinforcement is assembled and tied to those doweled bars.
- The formwork for casting the new concrete is built, and then followed by casting the repair concrete.

Repair details for each barrier repair scenario is discussed in the next section.

4.2.4 Fabrication

As-designed barriers (DS and DG) will be cast in two stages to simulate construction practice. First, formwork to mold the deck slab will be constructed, and the rebar cages put in place using chairs. To provide means of anchoring the concrete slab to the laboratory strong floor, four 50-mm diameter PVC tubes are required in the formwork to create 50-mm diameter holes through the slab thickness. When testing, Steel rods will be placed through those holes to tie the slab to the strong floor. These anchorage points are meant to simulate bridge girders. Then, a ready-mixed normal

weight concrete with a specified compressive strength of 45 MPa will be poured to cast the deck slab. This concrete specified compressive strength is a common practice in bridge decks and barriers and was recommended by Alberta transportation. All barrier-deck overhangs will be cast using the same concrete type. In stage two, formwork to cast the parapet concrete is constructed, and the rest of reinforcement tied together. Then, the parapet concrete is poured. To ensure adequate curing of concrete, thoroughly wet concrete surfaces will be covered with plastic sheets for the first seven days to reduce the loss of concrete mixing water. These sheets will be placed after the concrete has hardened enough to avoid surface damage.

Unlike as-designed barrier-deck overhangs, the full length of deck slab in the first repair prototype (RG-P) will be constructed and cast without parapet reinforcement sticking out of it to save material. After initial curing, the concrete at the deck's edge facing the future barrier wall will be roughened to simulate repair of damaged barrier wall. The concrete surface at the repair section will be roughened to around 6 mm using a chisel bit on a hammer drill, and then holes are drilled into the overhang deck slab using a rotary hammer drill to dowel in GFRP bars which will transfer forces from the barrier parapet to the deck slab. Chemical adhesive (Hilti RE 500) will be injected in the drilled holes before the GFRP bars are placed to hold them in place and transfer loads, and GFRP bars are then doweled. Then, the parapet formwork will be constructed, the rest of GFRP bars assembled, and concrete poured and cured just like the previous specimens. Due to deck slab thickness limits and requiring concrete cover, the embedment length of the embedded GFRP bars will be 185 mm which represents roughly $12d_b$.

The second repair prototype (RG-D) differs in terms of the initially poured deck slab length. The deck slab will be cast to a length of 1700 mm. After initial curing, the concrete surface, into which the rebars are doweled, will be roughened using a rotary hammer with a chisel bit to provide a better surface for concrete connection. Then, holes will be drilled and filled with epoxy (Hilti RE 500) to dowel repair reinforcement consisting of #6 and #5 GFRP bars for top and bottom transverse reinforcement, respectively. Holes to dowel the top mat of rebars are 700 mm in depth to provide embedment lengths of $35d_b$ (35 x 20 mm = 700 mm). Bottom holes are 560 mm deep (35 x 16 = 560 mm). Afterwards, the rest of the deck slab will be cast, the parapet reinforcement assembled, then parapet concrete poured and cured following the process used for prototype DG. The final repair prototype (RH-P) will be a hybrid one, with steel reinforcement as the main reinforcement in the overhang that is then retrofitted with GFRP reinforcement in the parapet.

Aside from the use of steel reinforcement in the deck, the construction process of RH-P will be essentially the same as RG-P. Finally, the parapet is poured.

Figure 4.5 shows the pouring stages of concrete in all specimens. Barrier specimens are labelled, and darker colours represent older concrete batches. For example, specimen RG-D is cast in three stages and hence the three colours.

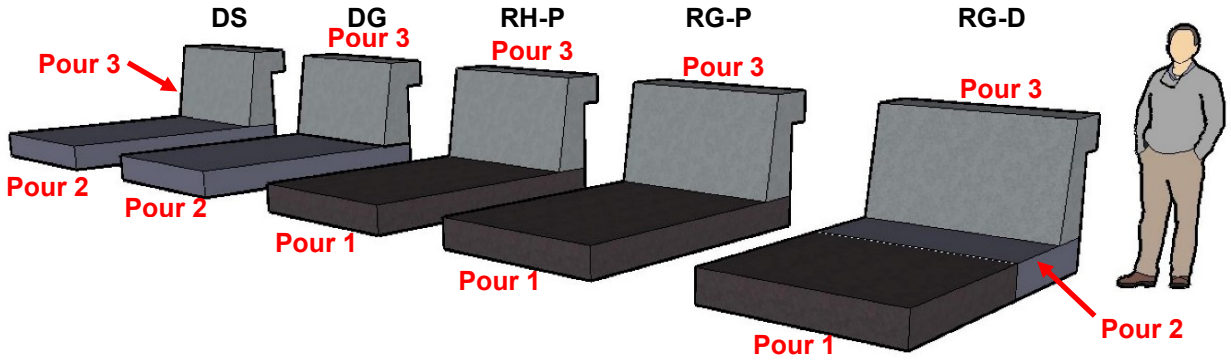

Figure 4.5: A diagram of the concrete pouring stages.

4.2.5 Materials

4.2.5.1 Concrete

Concrete properties specified for this project are reflective of common practice and represent AT requirements reported by Ahmed et al. (2010) which are reported in Table 4.2. A ready-mixed normal weight concrete of targeted compressive strength of 45 MPa will be used to cast all specimens. An average slump of around 120 mm is targeted for the concrete batches, and super-plasticizers will be added when needed. Six concrete cylinders (150×300 mm) will be taken from each concrete batch during the casting of the specimens, and they will be tested to find the average compressive strength of each concrete batch.

Table 4.2: Concrete mix ingredients per cubic metre (1 m^3) (Ahmed et al. 2010).

Ingredients		Quantity	
		(kg)	(m^3)
Aggregate 5-10 mm		346	0.130
Aggregate 20 mm		658	0.242
Sand		761	0.291
Cement - GUb-SF		383	0.126
Fly Ash		50	0.020
Water		145	0.145
Air		0	0.050
Additives	Retarder: Eucon 727	75 ml/100 kg	
	Water reducer: Eucon Dx	230 ml/100 kg	
	Superplasticizer: Eucon 37	3800 ml/m3	
	Air entraining: AIR-EXTRA	130 ml/100 kg	

4.2.5.2 GFRP

The mechanical properties of the sand-coated GFRP bars, which are composed of 80% type E-CR glass fibres and 20% vinyl-ester resin (by weight), are reported according to the manufacturer in Table 4.3 (TUF-BAR Canada 2019). Appendix 1 contains more information on the tensile testing of GFRP bars, and experimental results on the tensile properties of GFRP bars from the same manufacturer.

Table 4.3: Mechanical properties of GFRP reinforcing bars according to the manufacturer.

Bar type	Bar diameter[a] (mm)	Bar area[a] (mm2)	Modulus of elasticity (GPa)	Tensile strength (MPa)	Ultimate strain (%)	Average Bond Strength (MPa)
Number 5						
Straight	15.9	199	62.6	1150	2.1	14.6
Bent[b]			50	1000		
Number 6						
Straight	19.1	284	62.7	1150	2	14.1
Bent[b]			50	1000		

[a] Nominal bar diameter and area.

[b] Tensile properties of straight portion.

4.2.5.3 Steel

Grade 400 steel is already procured for barrier specimens. It has a specified yield strength of 400 MPa, and an elastic modulus of 200 GPa.

4.2.6 Test Setup and Instrumentation

To test the barrier-deck overhangs, a hydraulic actuator load frame with a capacity between 300 and 500 kN was designed and constructed (Figure 4.6). To simulate a deck-girder connection, test specimens will be placed on two parallel HSS steel beams spaced at 600 mm. The specimens will then be anchored to the laboratory strong floor using 31-mm diameter steel rods and nuts. A tensile force (100kN) will be applied on each rod to prevent rigid body displacement during tests. This connection will leave a clear overhang of 1.5 m from the outside face of the HSS and the edge of the barrier to simulate common practices in real bridge barrier-deck overhangs. Load will be applied using an actuator with a minimum capacity of 400 kN at a vertical distance of 700 mm from the deck slab top surface. The actuator load will be spread over a 1050 mm width using a spreader beam as per S6:19 requirements for barrier design.

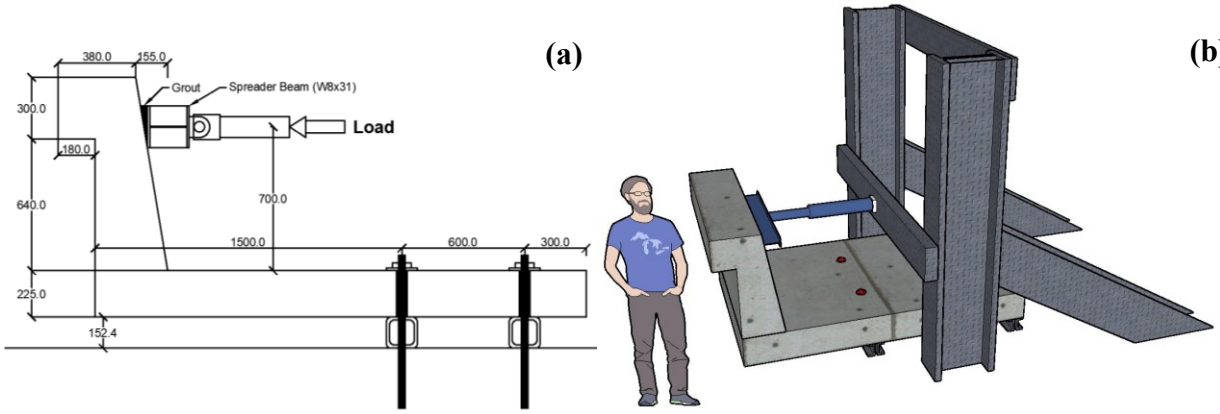

Figure 4.6: Static test setup (a) 2-D (b) 3-D. All dimensions in mm.

Each barrier-deck overhang is instrumented with twelve electrical resistance strain gauges (5 mm in gauge length and 120Ω in resistance) to measure strains in reinforcing bars (Figure 4.7). Locations of strain gauges on the vertical rebars of the barrier wall are shown in Figure 4.8. Transverse strain gauges are installed on rebars in the deck slab as shown in Figure 4.9. These locations were selected based on anticipated high stress concentration areas in rebars based on FEA models (Chapter 3) and engineering judgement. The locations of strain gauges are fixed for all specimens to collect consistent readings for comparison purposes.

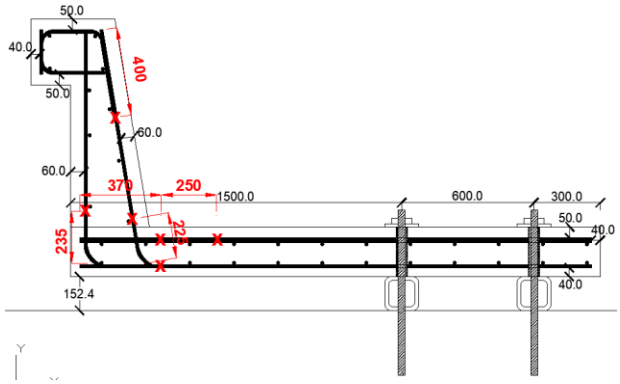

Figure 4.7: Strain gauge locations (marked with a red 'x') in barrier-deck overhangs. All dimensions in mm.

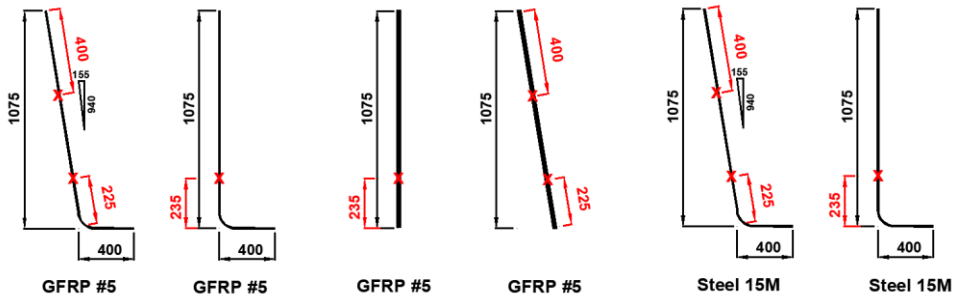

Figure 4.8: Strain gauge locations (marked with a red 'x') on vertical rebar. All dimensions in mm.

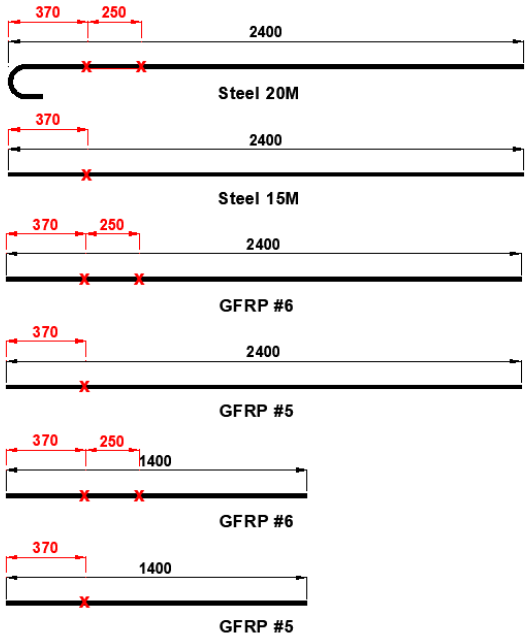

Figure 4.9: Strain gauge locations (marked with a red 'x') on transverse rebars. All dimension in mm.

Strain gauges in the deck slab are located in two transversal planes (perpendicular to the horizontal axis) to acquire average strain readings of the rebars. These horizontal planes are 900 mm apart, and at a distance of 300 mm from the sides. Figure 4.10 shows an elevation view of strain gauges locations. Figure 4.11 shows the layout of strain gauges in the barrier wall. Similarly, they are located in two transversal planes; however, they are not aligned with the strain gauges in the deck slab due to spacing discrepancy.

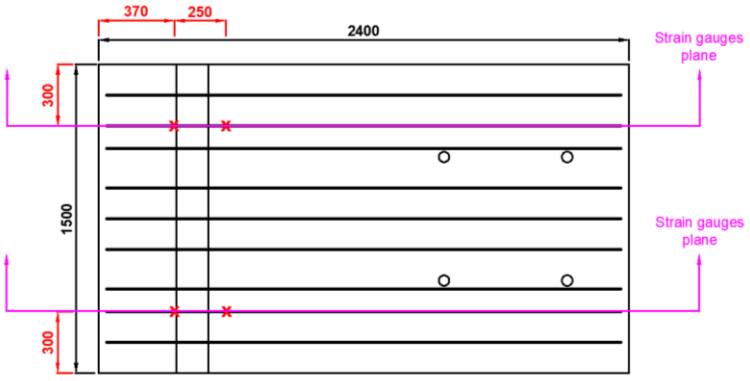

Figure 4.10: Layout of strain gauges (marked with a red 'x') in the deck slab. All dimensions in mm.

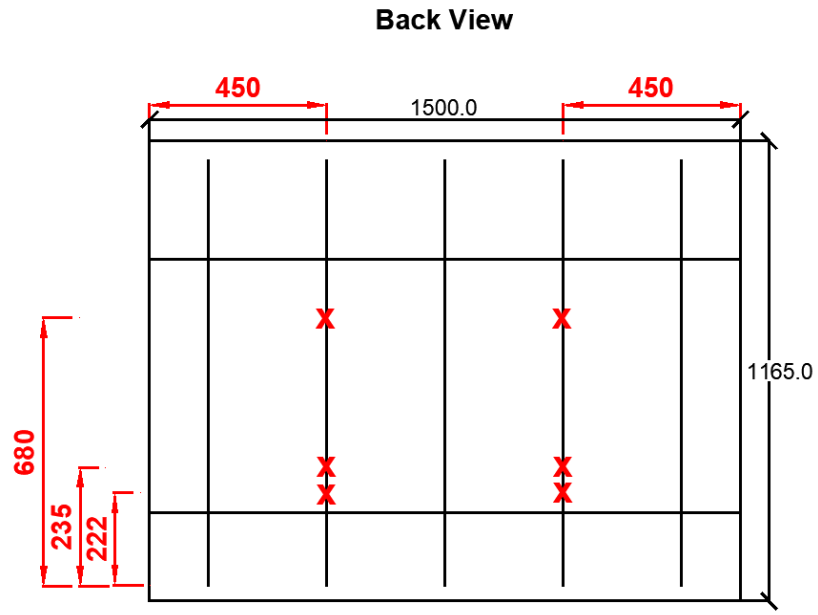

Figure 4.11: Layout of strain gauges locations (marked with a red 'x') in the barrier wall. All dimensions in mm.

Vertical and horizontal induced displacements and deflections of barrier-deck prototypes are measured using linear variable differential transducers (LVDT's). LVDT's are placed at the top of the barrier wall and at the barrier wall-slab joint (Figure 4.12) to measure the horizontal displacement and deflection of the barrier wall. Also, LVDT's are placed at the bottom of the deck slab to measure vertical deflection of the overhang. Each location will be equipped with two LVDTs to take average values and measure any differences from one side of the specimen to the other.

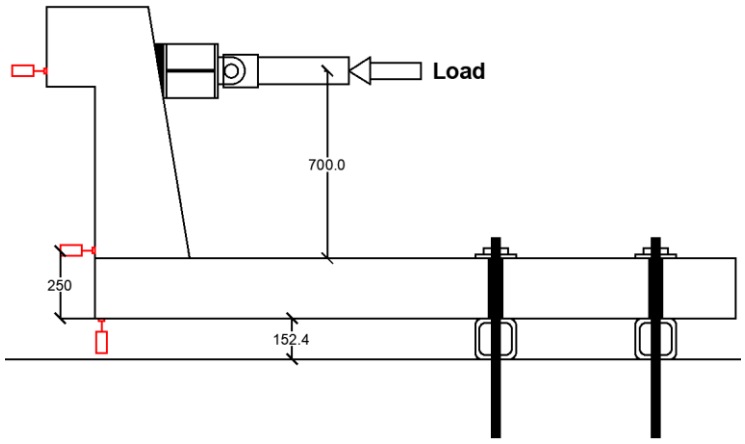

Figure 4.12: Positions of LVDT's.

4.3 Current Status of the Experimental Program

As mentioned earlier in this chapter, the test setup for testing the barriers was designed and the required parts to construct it are available and ready to be assembled. All materials and equipment needed to build and test the specimens are procured (e.g. steel bars, GFRP bars, rotary hammer drill, drill bits, plywood/timber for formwork, strain gauges, LVDTs) with the exception of concrete. The reinforcement was cut and bent according to the design drawing, instrumented with strain gauges, and wired to be hooked to the data acquisition system. The formwork design was completed and the construction process (tying of bars, cutting of formwork) began. Unfortunately, this experimental work, like other research projects on campus, was halted because of the COVID-19 pandemic and will not be able to be resumed until, ideally, 2021.

4.4 Chapter Conclusion

Five bridge barriers were proposed for experimental testing. Three of these barriers will be used to evaluate repair techniques for GFRP-RC bridge barriers by comparing their performance to two remaining reference barriers (one steel-RC and one GFRP-RC). These barriers were designed based on previous research and after consultation with Alberta Transportation and a GFRP bar producer. The proposed instrumentation will be used to assess the load-deflection response of the barriers as well as strains in critical regions as determined in previous finite element models.

Since the experimental project was halted, it was decided to evaluate the performance of the barriers proposed in this chapter numerically using finite element modelling in VecTor2. The development and results of these models as well as a parametric study on the influence of various contributing factors on GFRP-RC barrier response are presented in Chapter 5.

5 MODELING OF TEST SPECIMENS

5.1 INTRODUCTION

FRP reinforcement is a viable alternative to steel reinforcement in concrete structures and primarily used due to its superior corrosion resistance (Ahmed et al. 2011). GFRP bars are well suited for bridge decks and barriers based on its structural performance and cost-effectiveness (El-Salakawy and Islam 2014). Though GFRP-RC barriers are corrosion resistant, GFRP-RC bridge barriers are susceptible to local damage and excessive cracking caused by vehicle impact. CSA S6:19 does not provide specifications on repairing or rehabilitating concrete bridge barriers reinforced with GFRP bars; this poses concerns regarding the feasibility of repairing GFRP-RC bridge elements (El-Salakawy et al. 2010).

El-Salakawy et al. (2014) tested two repair techniques for performance level (PL-2) barriers, namely planting (doweling) and NSM techniques. Both techniques showed satisfactory structural performance. The efficiency of these repair techniques needs to be investigated in other barrier shapes with different reinforcement schemes. To investigate the feasibility of replacing steel rebar with GFRP in AT TL-4 barrier overhangs, and the efficiency of repairing GFRP-RC barriers with the doweling repair technique, five models were created and analyzed using VecTor2 (Wong et al. 2013). Parameters affecting these models were then studied to assess their influence on the barrier overhang.

5.2 METHODOLOGY

Modelling presented in this chapter is comprised of two stages. The first stage presents the results of modeling the barriers presented in Chapter 4, and the second stage explores the effect of changing parameters (e.g. deck thickness, overhang length) on the modelled barrier response.

5.2.1 Simulation of proposed barrier tests

The five AT TL-4 barrier-deck overhang designs and repair techniques presented in Chapter 4 (see Figure 4.1 and Figure 4.2) were modelled using VecTor2 software. The first model, DS, is a control that represents a typical steel-RC barrier design. The second model, DG, is reinforced with GFRP reinforcement with the same reinforcement layout as the steel-RC barrier (DS). Another two GFRP-RC models (RG-P and RG-D) simulate different repair scenarios. Model RG-P simulates the repair of a damaged barrier parapet while model RG-D simulates repair of damage that extends into the deck slab overhang. A fifth overhang model (RH-P) represents situation where an

originally steel-RC barrier-deck overhang is repaired with a new GFRP-RC barrier wall. These five models reflect the designs and repair scenarios presented in Figure 4.2.

Models were analyzed using VecTor2 using horizontal displacement-controlled loading at a height of 700 mm above the deck slab, which represent the equivalent static load proposed in Chapter 4 (see Figure 4.5). Model results were analyzed using Augustus (a VecTor2 post-processor). Due to an unanticipated and extended lab closure for the COVID-19 pandemic, the experimental program presented in Chapter 4 and verification of these models against those results will be completed in future as part of a future thesis.

5.2.2 Parametric study

The second stage of modelling is a parametric study using VecTor2 to investigate the effect of design parameters on the as-designed and repaired models previously simulated in the first stage. For the as-designed models, the investigated parameters are overhang length (OL), deck thickness (DT), rebar spacing of the top mat of the deck slab reinforcement (SDT), and rebar spacing of the front assembly of the barrier wall reinforcement (SPF). For the models that simulate different repair techniques, the effect of the aforementioned parameters were investigated in addition to the effect of doweled bar spacing of the top mat of the repaired portion of the deck slab (DSD), doweled rebar spacing of the front assembly of the repaired portion of the barrier wall (DSP), and embedment length of the doweled rebar of the repaired portion of the deck slab (EDD). Table 5.1 shows the various parameters considered and their respective values.

Table 5.1: Investigated model parameters and their respective values.

Parameter		Value 1 (mm)	Value 2 (mm)	Value 3 (mm)	Value 4 (mm)	Value 5 (mm)
Overhang length	OL	500	1000	1500	2000	2500
Deck thickness	DT	175	200	225	250	275
Spacing of deck top mat reinforcement	SDT	100	150	200	NA	NA
Spacing of parapet front bar assembly	SPF	100	150	200	NA	NA
Dowelled reinforcement spacing in deck	DSD	50	100	150	200	NA
Dowelled reinforcement spacing in parapet	DSP	50	100	150	200	NA
Embedment length of deck dowels	EDD	300	500	700	900	NA

These parameters were considered due to their influence on the barrier-deck overhang response. Barrier overhang length varies from one bridge to another and many researchers have tested shorter lengths than those seen in practice, making overhang length a factor to investigate further. CSA S6:19 specifies a minimum concrete deck thickness of 175 mm; however, the used thickness in practice is affected by many factors such as reinforcement material and design loads which makes

it another important parameter to explore. The rebar spacing of the top mat of the deck slab and the front assembly of the barrier wall reinforcement were investigated due to their role in resisting the overhang negative moment, and to find an optimal (i.e. economic) rebar spacing without compromising the required barrier strength. Finally, the effects of doweled bar spacing of the top mat of the repaired portion of the deck slab, doweled bar spacing of the front assembly of the repaired portion of the barrier wall, and embedment length of the doweled bars of the repaired portion of the deck slab were investigated to evaluate their influence on restoring the damaged barrier's strength and to help optimize repair techniques.

5.3 BRIDGE BARRIER-DECK OVERHANG BASE MODELS DETAILS AND MATERIAL PROPERTIES

Concrete was modeled using 2-D plane membrane elements (plane stress condition) with a maximum mesh size of 25 × 25 mm, and an aspect ratio of 1.5. The thickness of these elements was 1000 mm which represents the width of the barrier overhang (i.e. results are provided for a metre unit width of barrier/deck). The as-designed models are defined using three regions of concrete: One region represents the deck slab, another represents the barrier wall, and the third one represents the interface between the deck slab and the barrier wall. The deck slab and barrier walls used the same properties. While the interface region is modeled with a concrete tensile strength of 0.01 MPa to reflect the inherent tensile weakness of concrete cold joints.

All models were loaded under an increasing monotonic displacement until a specified displacement of 80 mm was reached, as described in Section 3.2.3. The support condition was taken as four pin supports in pairs at 600 mm apart, one pair of them is at 300 mm from the free end of the deck slab. This support condition is representative of the support condition proposed for lab testing which also represents the expected support conditions provided by girders in actual bridges. Figure 5.1 shows a visual of an as-designed model in VecTor2.

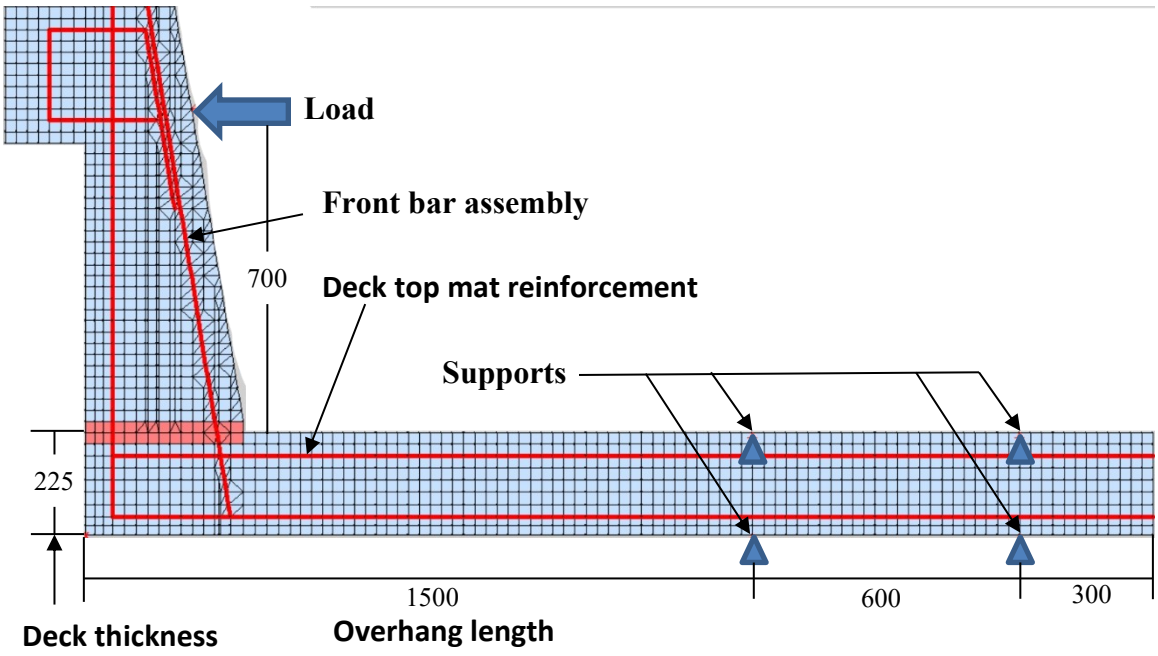

Figure 5.1: A simulated barrier-deck overhang model in VecTor2, all dimensions in mm.

All models had a top concrete cover of 50 mm, a bottom concrete cover of 40 mm for the decks, a 60 mm cover for the front and back faces of the barrier wall, a 50 mm cover for the top and bottom faces of the beam-like protrusion of the barrier wall, and 40 mm for its back face.

Concrete was modelled using the same properties as the barriers modelled in Chapter 3, specifically Section 3.2.2. The concrete compressive strength is 45 MPa and tensile strength is 2.21 MPa with a modulus of elasticity of 29200 MPa (calculated as per A23.3). The concrete is normal density (2400 kg/m^3) with a maximum aggregate size of 20 mm.

Steel reinforcement was modelled with a 400 MPa yield strength, 600 MPa ultimate strength, and a 200 GPa modulus of elasticity. The ultimate tensile strain is 10% and the strain hardening strain is 1.2%.

GFRP rebar was modelled as linear-elastic until failure with a 1165 MPa ultimate strength, 62.7 GPa modulus of elasticity, and 2% ultimate tensile strain. These GFRP properties are based on those given by manufacturers for high modulus GFRP bars.

5.3.1 Bond behaviour

In design the change in concrete strain is often assumed to be equal to the change in reinforcement strain at that level; this is referred to as ‘perfect bond’. However, under large bond stresses, bond between concrete and reinforcement weakens and results in a non-negligible differential strain

between concrete and reinforcement (i.e. 'imperfect bond'). Imperfect bond manifests itself as bond slip (relative slip) between concrete and reinforcement. Bond slip is most critical in areas like anchorage zones where large bond stresses are expected due to the high stress gradients in the reinforcement. Proper detailing of RC members prevents bond failure (i.e. bar pull-out) and allows designers to assume perfect bond in modelling such members while still maintaining reasonable accuracy. However, assuming perfect bond may underestimate deflections and capacities of RC structures, particularly those like bridge barriers and decks with large bond stresses at the deck/barrier joint. To investigate the viability of using the perfect bond assumption in modelling barrier-deck overhangs, ten GFRP-RC barrier models were run that represent the GFRP as-designed barrier and two repair scenarios.

Models RG-P1-PB and RG-P1-IB represent repair scenarios in which the front bar layer of the barrier wall is embedded 100 mm into the deck slab, and models RG-P2-PB and RG-P2-IB represent a repair scenario in which the front bar layer of the barrier wall is embedded 185 mm into the deck slab. RG-D1-PB and RG- D1-IB represent a repair scenario in which the transverse reinforcement of the top mat of the deck slab rebar is embedded 300 mm into the deck slab at the repair section (700 mm away from the cantilevered end of the deck), and models RG-D2-PB and RG-D2-IB simulate an embedment of 700 mm in the repair section.

Models denoted with 'PB' were modelled assuming perfect bond. This means that the concrete elements and discrete reinforcement elements are defined by common nodes and undergo a compatible displacement. Models denoted with 'IB' were modelled with bond-slip elements (link elements) which serve as deformable interfaces between concrete elements and discrete reinforcement elements. These link elements allow for relative displacement between concrete elements and discrete reinforcement elements. The bond-slip behaviour of link elements for GFRP rebar was obtained from Ahmed et al. (2008) and modeled according to the Eligehausen model for the confined and unconfined bond stress-slip behaviours.

Figure 5.2a shows the effect of perfect/imperfect bond assumptions on barrier walls. The load capacities in Figure 5.2 onwards are expressed per metre width of barrier. Bond slip (for 'IB' models) is more pronounced with longer embedment lengths where pull-out failure modes take more force to develop. The perfect bond assumption has a small influence over pull-out failure modes of shorter embedment lengths since the small strains of the perfect bond assumption are acting along shorter lengths relative to longer embedment lengths with the same small strains of

the perfect bond assumption. The strength reduction from imperfect bond at an embedment depth of 100 mm is 16.7% whereas a reduction of 27.7 % is experienced at an embedment depth of 185 mm. The reduction in horizontal deflection (at the load point) at failure due to bond slip is 23.3% at an embedment depth of 100 mm, and 23.5% at an embedment depth of 185 mm. The perfect bond assumption does not change the pull-out mode of failure for relatively short embedment lengths. However, at some point with the increase in embedment length, assuming perfect bond may alter the predicted failure mode.

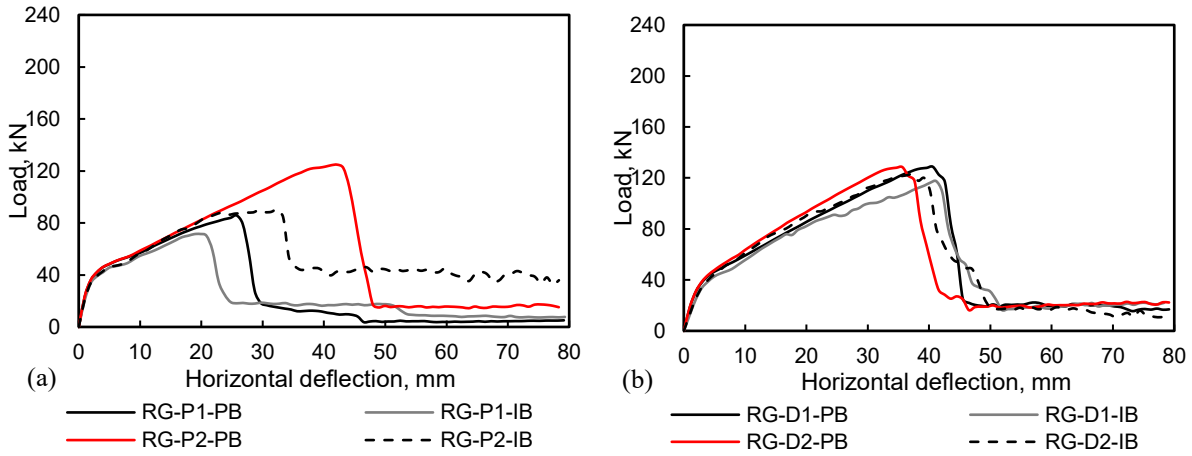

Figure 5.2: Effect of bond behaviour on (a) barrier wall repair scenario (b) barrier-deck overhang repair scenario.

Figure 5.2b shows the effect of bond behaviour on the barrier-deck overhang repair scenario. The assumption of perfect bond has little effect on barrier strength in this scenario. At an embedment length of 300 mm, there is an 8.9% reduction in strength due to bond slip. The effect of bond slip drops at a higher embedment of 700 mm with a 4.5% reduction in strength. The increase in horizontal deflection (at the load point) at failure from bond slip is 1.5% at an embedment depth of 300 mm, and 4.3% at an embedment depth of 700 mm.

Assuming perfect bond action in as-designed models, where proper anchorage is provided, is a valid assumption. Model DG-IB had a similar stiffness to model DG-PB up until a load of 90 kN, as seen in Figure 5.3. However, DG-PB failed at a higher load of 128.8 kN compared to DG-IB which failed at a peak load of 116 kN. Perfect bond assumption overestimates the load capacity by 10%, and the horizontal deflection (at the load point) at failure by 4.7%.

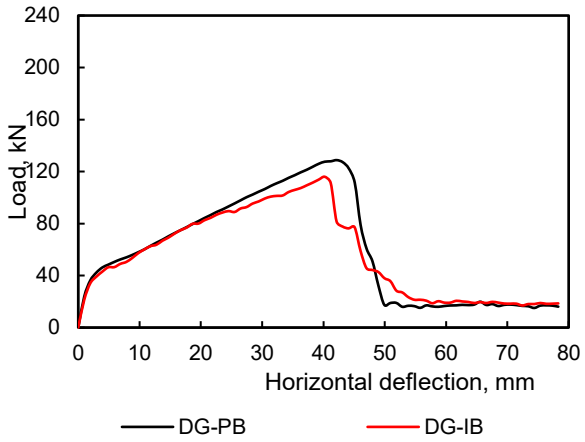

Figure 5.3: Effect of bond behaviour on the as-designed GFRP reinforced model.

The perfect bond assumption is sensitive to embedment length, reinforcement anchorage, bond stresses and strains, and failure modes. For instance, assuming perfect bond has limited effect on the 100 mm embedment depth but significant effect on a 185 mm embedment depth. This adverse effect diminishes with the increase in embedment length to 300 mm. In the case of as-designed models, perfect bond assumption has a small influence over the barrier capacity and behaviour. For most of the following models, the perfect bond assumption was used as it made analyzing the models computationally efficient, and also provides a reasonable estimation of load capacity and deflection at failure for most cases.

5.3.2 Bond-slip modeling

Bond slip behaviour can be modeled in different ways in VecTor 2. Discrete reinforcement elements (truss bar elements) are attached to RC elements using bond-slip elements (link elements). Link elements are two-noded, nondimensional elements defined by two different nodes and have four degrees of freedom in total.

Reinforcement anchored to concrete may be assumed to be areas of perfect bond behaviour where the strains of reinforcement elements equal to the strains experienced by RC elements. These assumptions make modeling RC more computationally efficient. Thus, VecTor 2 allows modeling discrete reinforcement elements with ‘mixed’ bond action in which some ends are modeled as perfectly bonded ends with others being imperfectly bonded. These mixed situations may represent, for example, single-headed GFRP bars and reinforcement in areas of high confinement pressure.

Five barrier parapet repair models were used to study the effect of bond assumptions. One model (RG-P2-PB) was built assuming perfect bond in all elements. RG-P2-IB was modeled assuming imperfect bond of reinforcement elements in the barrier-deck joint, and perfect bond at the other ends of reinforcement elements. Considering bond stress distribution, this model is most representative of real barrier overhangs. A third model (RG-P2-HR1) was built assuming that single-headed reinforcement is used in the deck slab at the barrier-deck joint. These headed bars were assumed to provide a perfect bond to the surrounding concrete but allowed for some degree of imperfect bond along the bar between the two ends. A fourth model (RG-P2-HR2) was modeled similarly to (RG-P2-HR1) but assuming that the barrier wall was repaired with embedded single-headed GFRP bar as the vertical reinforcement in the front assembly of the parapet reinforcement. This rebar has two end points of perfect bond, and a middle point of imperfect bond. A fifth model (RG-P2-EIB) was built assuming entirely imperfectly bonded reinforcement elements.

Figure 5.4 shows the load-horizontal deflection curves of the investigated models. These models showed similar stiffnesses up to a load of 75 kN. Model RG-P2-PB has a higher load capacity (124.8 kN) due to the perfect bond assumption which overestimates the barrier overhang capacity and deflection at failure. Models RG-P2-IB and RG-P2-EIB have similar capacities (89.1 kN and 90.2 kN, respectively) which supports assuming a perfect bond action in areas of low bond stresses to simplify modelling. Assuming perfect bond overestimates this barrier overhang capacity by a ratio of 1.4. Using single-headed GFRP reinforcing bars at the barrier-deck joint to repair the barrier overhang could increase the barrier overhang strength by a ratio of 1.33 as in RG-P2-HR2, and by a ratio of 1.16 as in RG-P2-HR1.

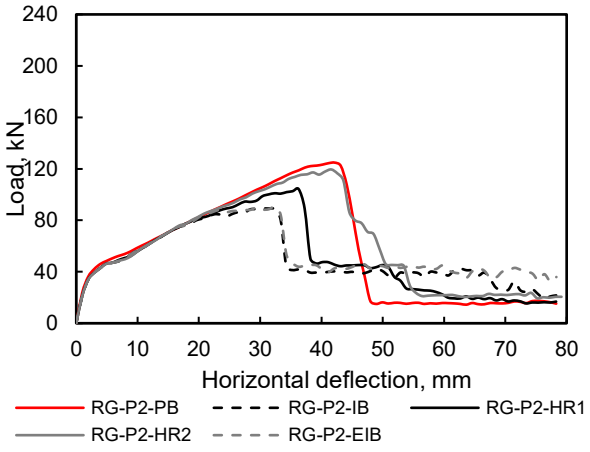

Figure 5.4: Effect of bond action assumptions on the barrier parapet repair models.

5.4 BASE MODELS RESULTS AND DISCUSSION

The load capacities in Figure 5.6 onwards are expressed per metre width of barrier. Though the minimum barrier width to develop realistic two-way action is three metres, due to software limitations (VecTor2 is a two-dimension FEA software) and to reflect proposed lab testing conditions, the models are analyzed in one-way action. The factored transverse design load for TL-4 bridge barriers specified by CSA S6:19 is 170 kN applied over a 1050 mm length. This load is applied across a 1.5 m wide barrier segment, to simulate lab testing, and then results are normalized to those a 1.0 m barrier segment. The normalized load required by CSA S6:19 for a one-metre-wide section of barrier, assuming a one-way load distribution, is 113.3 kN.

To approximate the required barrier-deck overhang width to allow for the efficient load distribution and transfer from the barrier wall to the deck slab, a previous version of the CHBDC commentary suggests the use of dispersal angles (CSA 2006). When a barrier wall is subjected to a transverse load, the effect of this load is distributed to the barrier wall and the deck slab with dispersal angles as shown in Figure 5.5, and results in the design forces (Table 5.2) for the inner (Figure 5.5a) and end portions (Figure 5.5b) of the barrier-deck overhang (Azimi et al. 2014, CSA 2006). The real angles of load dispersion and the associated forces depend on the geometry and stiffness of the barrier-deck overhang, and the location of load application relative to supporting elements (CSA 2006). Assuming the most critical case for moments in the deck a PL-2 (TL-4) barrier which is moment in the end portion of the deck, an angle of load dispersion of (55°) is used to find the minimum width of barrier-deck overhang that is required to achieve an efficient load transfer from the barrier to the slab. This width is 2050 mm, and it results in a normalized factored transverse load capacity limit of 82.9 kN/m.

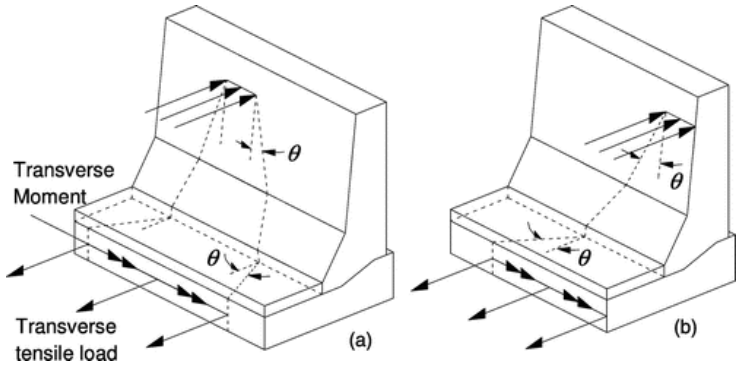

Figure 5.5: Transverse load dispersion at the (a) inner portion and (b) end portion of the barrier-deck overhang (Azimi et al. 2014).

Table 5.2: Design Forces for Barrier-deck overhang due to transverse load (reproduced from CSA 2006).

Model ID	Dispersal angle for barrier	Dispersal angle for deck	PL-2
Factored transverse load, kN (Clause 3.8.8.1)	-	-	170
Length of load application, mm (Clause 12.5.2.4)	-	-	1,050
Height of load application above deck, mm (Clause 12.5.2.4)	-	-	790
Moments in inner portion of deck, kN·m/m	56	55	38
Tensile force in inner portion of deck, kN/m	25	20	100
Moments in end portion of deck, kN·m/m	55	55	52
Tensile force in end portion of deck, kN/m	8	8	142

5.4.1 As-designed barrier-deck overhang models

General results for the as-designed and repaired models are shown in Table 5.3. The ultimate load capacity of GFRP-RC bridge overhangs is more influenced by the stiffness of the reinforcing bars than their ultimate tensile strength. Figure 5.6a presents the load-horizontal deflection curves of the as-designed models. The steel-reinforced model (DS) and the GFRP-reinforced model (DG) start with similar stiffness until concrete cracks. The stiffness of model DG then drops relative to model DS because of the lower elastic modulus of GFRP. DS had a 43% higher ultimate capacity (183.7 kN) than DG (128.8 kN) though DS failed at a lower deflection compared to DG. Load stopped increasing and DS reached a peak load once steel reinforcement yielded, and the barrier failed very soon after. Yielding of the steel reinforcement of the top mat of the deck was followed by concrete splitting in the deck caused by the tensile stresses developed at the barrier-deck junction. The barrier wall did not show significant transverse cracks and failure was governed by the diagonal shear failure in the deck.

Table 5.3: Key results from as-designed and repaired models.

Model ID	Peak load, kN	Deflection at failure, mm	Energy absorbed before failure, kN.mm	Failure mode
DS	183.7	23.8	2863	Yield-concrete splitting
DG	129.3	43.6	3826	Concrete splitting
RG-P	124.7	42.6	3665	Concrete splitting
RG-D	128.8	35.7	3129	Concrete splitting
RH-P	149.3	35.6	4118	Two-Phased

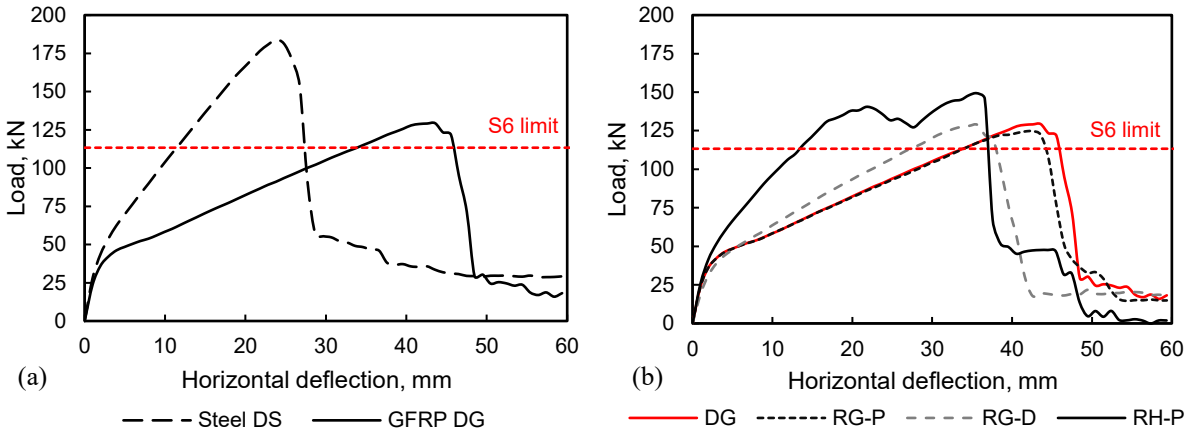

Figure 5.6: Load-horizontal deflection (at the load point) curves (a) for Steel and GFRP reinforced models (b) the proposed repair scenarios models.

DG's reinforcement did not develop its full tensile strength. This is commonly seen in FRP-RC since it is often designed to be over-reinforced. Model DG failed with a maximum developed tensile stress around 25% of the tensile strength of GFRP bars. Similar to DS, DG's failed by the splitting of concrete in the deck slab at the barrier-deck junction due to diagonal shear. However, failure was initiated due to loss of cohesion caused by excessive crack widths (4.4 mm) in the concrete at the peak load.

Although the CHBDC does not specify limits for the horizontal deflection of barrier walls, excessive vertical deflections of barrier-deck overhangs may cause serviceability concerns. Model DS failed at a lower vertical deflection (20.6 mm), measured from the bottom corner of the barrier-deck joint, as shown in Figure 5.7a than DG. This is attributed to the higher stiffness of steel rebar compared to GFRP. Similar to the horizontal deflection curves, both models have similar stiffness up to first cracking then diverge once the reinforcement carries the majority of tensile stresses. Both models had load capacities exceeding the factored design load specified by S6:19 (113.3 kN). Once models DS and DG hit the peak load, the vertical deflection decreased (Figure 5.7a). The concrete splitting at the barrier-deck joint leads to separation between the barrier wall and the deck slab which relieves the deck from the loads and allows it to partially return to its original place.

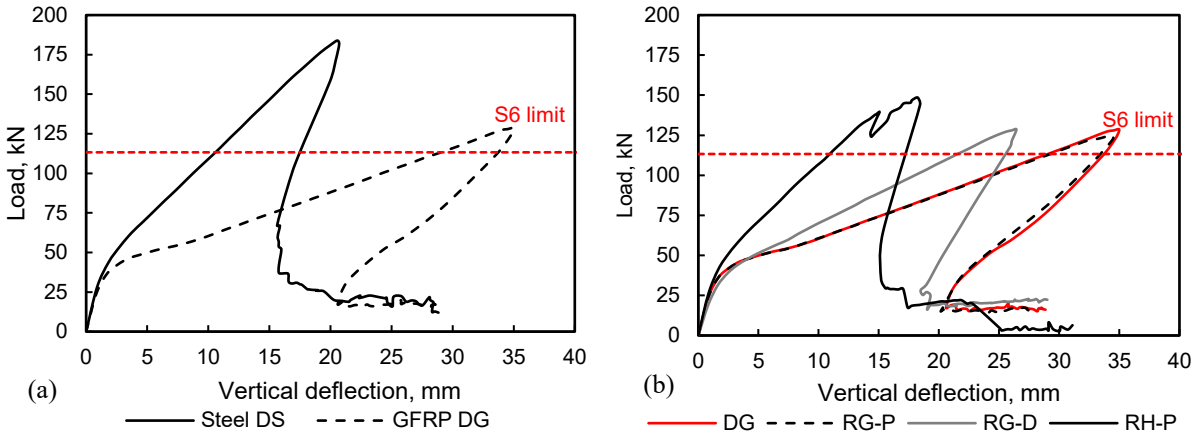

Figure 5.7: Load-Vertical deflection (at the bottom corner of the barrier-deck joint) curves (a) for Steel and GFRP reinforced models (b) proposed repair scenarios models.

5.4.2 Repaired barrier-deck overhang models

Figure 5.6b presents load-horizontal deflection curves of the models simulating repaired barrier-deck overhangs. The repair models had similar stiffnesses to as-designed models (DS and DG) until first cracking. Then, the difference in stiffness between those models becomes more pronounced. Model RH-P, reinforced with a hybrid reinforcement system (Steel RC decks repaired with doweled GFRP bars), has higher stiffness compared to the other repair systems techniques and falls between the two as-designed models (DS and DG) due to the interaction of the higher modulus of steel in the deck and the lower modulus of GFRP in the barrier. This difference in materials between the barrier and the deck leads to the two-phased failure mode. First, a crack develops between the barrier wall and the deck, and this crack becomes 2 mm wide at a horizontal load of 70 kN. This crack continues to widen and deepen as the tensile stresses in bars at the face of the barrier wall bars increase. Increased tension in the GFRP results in development of bond cracks along the barrier face and partial separation of concrete cover of the barrier. This causes the stiffness of the system to drop after reaching a 140 kN load. More shear cracks in the deck develop and load drops until it reaches a low point of 126 kN. At this point, steel reinforcement in the deck becomes more involved in resisting the load and leads to the increase in stiffness of the overhang which results in a second peak in at 149 kN. It should be noted that reinforcement in this model is assumed to be perfectly bonded which may overshadow the possible pull out failure of the barrier wall reinforcement. Nevertheless, the influence of the perfect bond assumption on the ultimate strength of the barrier models varies as discussed earlier in Section 5.3.1 and diminishes with longer reinforcement embedment lengths of and proper anchorage (e.g. using headed GFRP bars).

Model RG-P had similar load deflection responses to the base model DG with a slightly lower peak load of 125 kN. This could mean one of two things: the straight doweled repair bars in the barrier of model (RG-P) were embedded enough into the deck to mobilize similar capacity to their bent counterparts in the original design (DG), or the perfect bond between the reinforcement and the concrete slightly influences the model strength and overall behaviour. The observed failure mode of repair model RG-P was similar to the as-designed model DG, namely splitting of concrete in the deck at the barrier-deck junction due to diagonal shear. Load-deflection responses show reduced deflection after reaching the peak load due to diagonal shear cracks in the deck causing separation of the barrier wall from the deck.

Model RG-D, which simulates repair in the deck slab, initially had a lower stiffness compared to the design barrier DG. This is attributed to the presence of the two concrete joints which present areas of weakness: one at the repair section in the deck slab, and the other at the barrier-deck interface. However, after concrete cracks, the top deck reinforcement in the repaired section becomes involved in carrying loads which makes the stiffness of the overhang system of model RG-D larger than that of DG after concrete cracking. The engagement of the top mat of bars of the deck slab in carrying loads at an early stage reduces tensile stresses in the front assembly of rebar in the barrier wall at the barrier-deck interface which results in the higher stiffness of model RG-D (Figure 5.6b and Figure 5.7b). Although model RG-D developed cracks across the deck slab at the repaired section near the peak load (129 kN), failure was a result of concrete splitting due to shear in the barrier-deck joint.

All repair scenarios were successful (i.e. satisfy the 113.3 kN factored design load of the CHBDC) in restoring barrier-deck overhang strength. Repair of steel-RC barrier overhangs with GFRP bars in model RH-P restored 80% of the capacity of model DS. Models RG-D and RG-P, which simulates repair of damaged GFRP-RC barriers or decks, both almost restored the full capacity of model DG.

5.4.3 Failure Modes

Three predominant failure modes are observed in barrier overhang models: Concrete splitting, yield-concrete splitting, and two-phased modes of failure. Figure 5.8a shows the cracking pattern of a concrete splitting mode of failure at the peak load for the base model DG. Figure 5.8b shows the stresses in the reinforcement of DG at the same load.

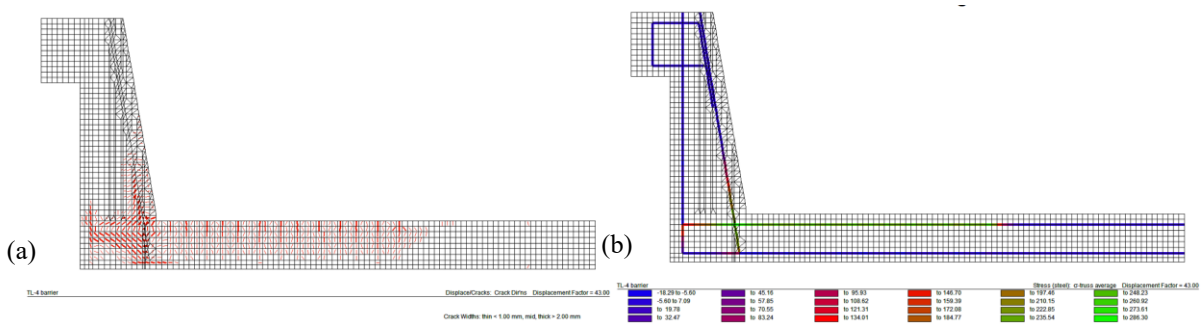

Figure 5.8: Concrete splitting failure mode of model DG (a) cracking pattern at peak load (b) stresses in the reinforcement at peak load.

Figure 5.9a shows the cracking pattern of a yield-concrete splitting mode of failure at the peak load for the base model DS. Figure 5.9b shows the stresses in the reinforcement at the same load.

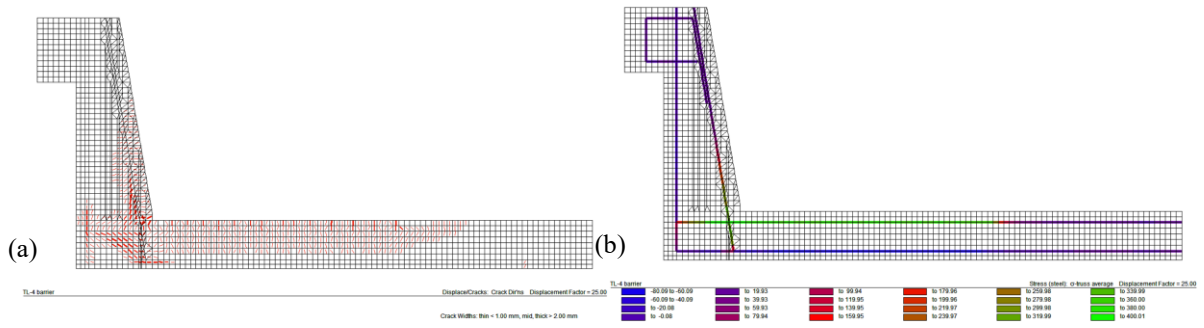

Figure 5.9: Yield-concrete splitting failure mode of model DS (a) cracking pattern at peak load (b) stresses in the reinforcement at peak load.

Figure 5.10a shows the cracking pattern of a two-phased mode of failure at the first peak load of the base model RH-P, and Figure 5.10b shows the cracking pattern of the same model at the second and maximum peak load. Figure 5.10c shows the stresses in the reinforcement of RH-P at the first peak load, and Figure 5.10d at the maximum peak load.

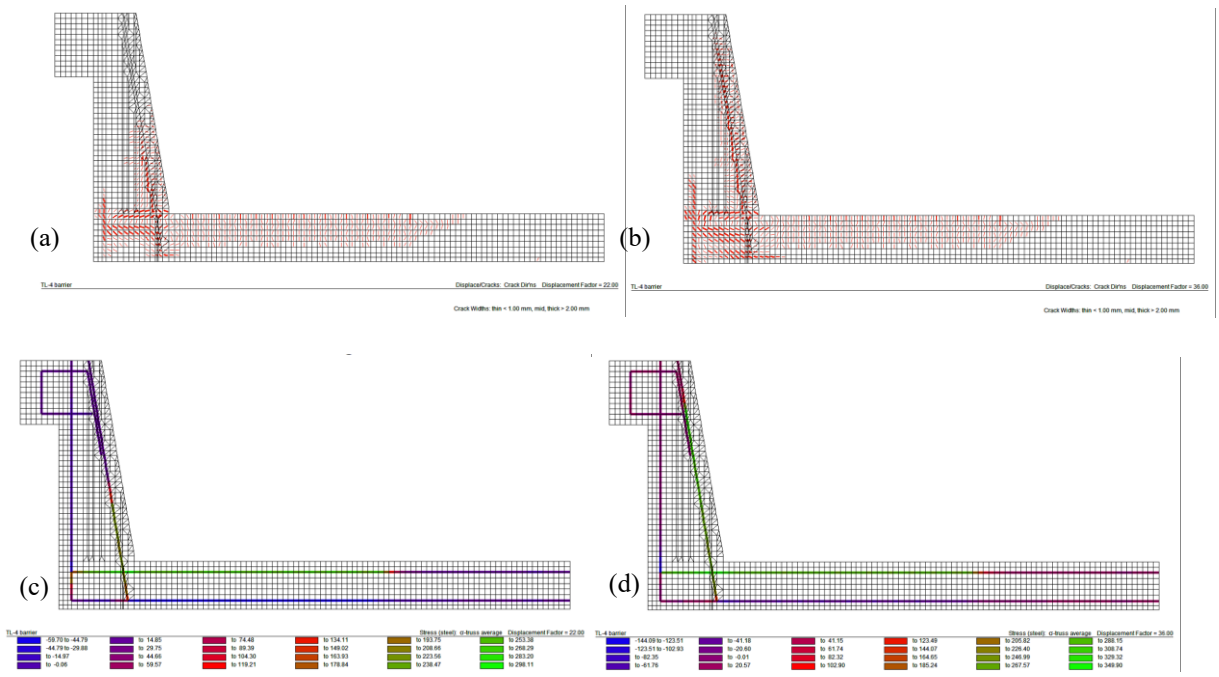

Figure 5.10: Two-phased failure mode of model RH-P (a) cracking pattern at first peak load (b) cracking pattern at second peak load (c) stresses in the reinforcement at first peak load (d) stresses in the reinforcement at second peak load.

5.4.4 Parametric study on barrier models

5.4.4.1 Overhang length effect

The effect of overhang length on the overall behaviour of the five base barrier models was investigated. Five realistic overhang lengths were chosen (500 mm, 1000 mm, 1500 mm, 2000 mm, and 2500 mm). In general, stiffness decreased with the increase in the overhang length, as shown in Figure 5.12 and Figure 5.13. This stiffness reduction is attributed to the fact that flexural stiffness is inversely proportional to length. However, changing the overhang length did not have much influence on the ultimate load capacity of the barriers, as seen in Figure 5.11a. Table 5.4 presents peak loads, horizontal deflections (at the load point) at peak loads, energy absorbed before failure, and the failure mode of barrier models with varying overhang lengths. The increased horizontal deflection at peak loads with the increase in overhang length results in higher energy absorption as presented in Table 5.4. The restored vertical deflection after reaching the peak load is increased with overhang length, as shown in Figure 5.13.

Models DS-OL1 through DS-OL5 had similar failure modes where the steel reinforcement yields at peak load. After yielding, there is an increase in steel rebar elongation rate in the region

that yielded which then leads to concrete splitting and diagonal shear failure in the barrier-deck joint.

DG models with different overhang lengths had diagonal shear failures before the development of the ultimate strength of GFRP rebar. A consistent 25% utilization of the GFRP rebar strength was observed across different overhang lengths at peak load capacity.

Barrier wall repair models RG-P-OL1 through RG-P-OL5 had concrete splitting failure modes as a result of the diagonal shear developed in the barrier-deck joint. Deck repair models RG-D-OL3 through RG-D-OL5 had similar behaviour and failure modes. Overhang lengths less than 1500 mm were not modeled for deck repair models since there was inadequate overhang length to embed the repair reinforcement 700 mm into the deck slab.

A two-phased failure mode is observed in all overhang lengths of RH-P hybrid repair system where the barrier wall partially gives in by excessive cracking and partial concrete cover separation and then the system finally fails due to concrete splitting caused by the diagonal shear developed in the barrier-deck joint.

Table 5.4: Key results from models investigating varying overhang lengths.

Model ID	Peak load, kN	Deflection at failure, mm	Energy absorbed before failure, kN.mm	Failure mode
DS-OL1	184.2	9.79	1359	Yield-concrete splitting
DS-OL2	183.4	16.66	2104	Yield-concrete splitting
DS-OL3	183.9	23.53	2835	Yield-concrete splitting
DS-OL4	183.6	31.37	3740	Yield-concrete splitting
DS-OL5	183.2	38.24	4470	Yield-concrete splitting
DG-OL1	127.6	17.6	1704	Concrete splitting
DG-OL2	126.7	24.4	2617	Concrete splitting
DG-OL3	128.8	42.2	3662	Concrete splitting
DG-OL4	125.8	54	4544	Concrete splitting
DG-OL5	125.2	66.7	5558	Concrete splitting
RG-P-OL1	125.7	17.6	1701	Concrete splitting
RG-P-OL2	124.9	29.4	2603	Concrete splitting
RG-P-OL3	124.8	42.2	3628	Concrete splitting
RG-P-OL4	124.6	54	4528	Concrete splitting
RG-P-OL5	124.6	65.7	5435	Concrete splitting
RG-D-OL3	128.5	36.7	3127	Concrete splitting
RG-D-OL4	128.8	48.1	4124	Concrete splitting
RG-D-OL5	125.6	58.9	4895	Concrete splitting
RH-P-OL1	144	24.4	3038	Two-phased
RH-P-OL2	144.1	29.3	3446	Two-phased
RH-P-OL3	148.5	35.2	4044	Two-phased
RH-P-OL4	146.4	40.1	4446	Two-phased
RH-P-OL5	146.7	45	4856	Two-phased

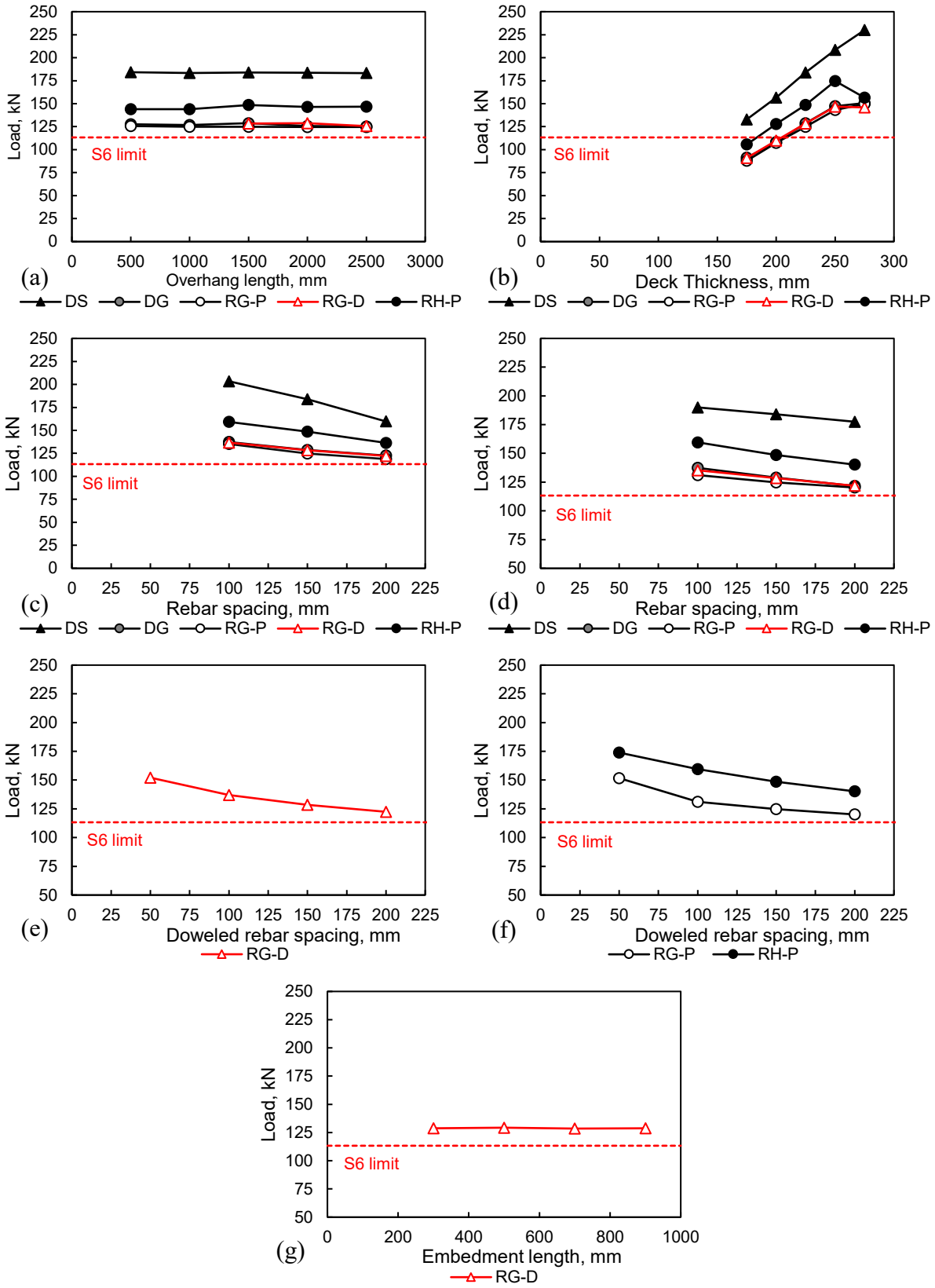

Figure 5.11: Effect of (a) OL b) DT (c) SDT (d) SPF (e) DSD (f) DSP (g) EDD on barrier peak load for (DS) model, (DG) model, (RG-P) model, (RG-D) model, and (RH-P) model.

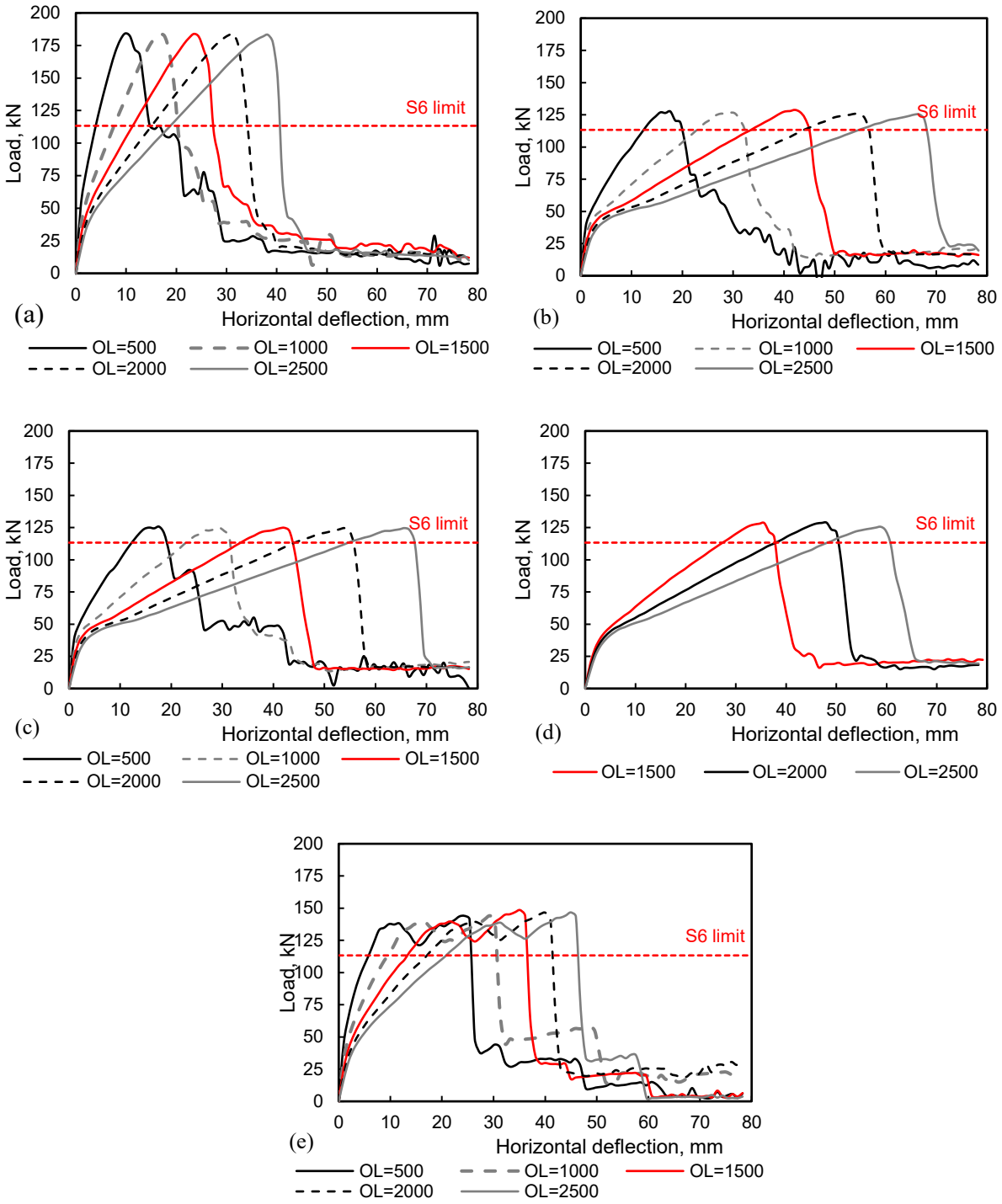

Figure 5.12: Load-horizontal deflection (at the load point) curves for multiple overhang lengths of (a) steel barrier (DS) model (b) GFRP barrier (DG) model (c) GFRP barrier repair (RG-P) model (d) GFRP barrier repair (RG-D) model (e) hybrid barrier repair (RH-P) models.

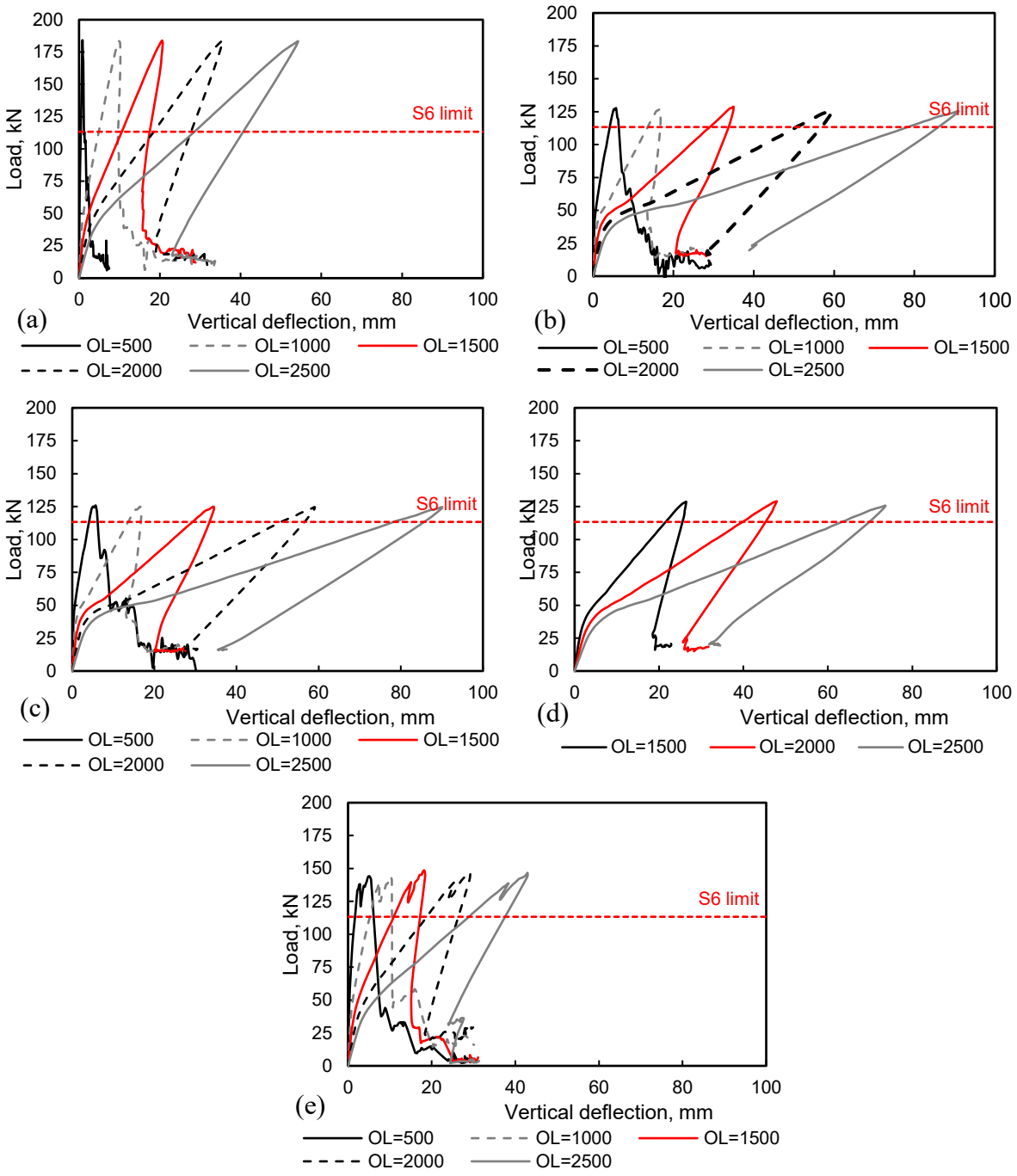

Figure 5.13: Load-vertical deflection (at the bottom corner of the barrier-deck joint) curves for multiple overhang lengths of (a) steel barrier (DS) model (b) GFRP barrier (DG) model (c) GFRP barrier repair (RG-P) model (d) GFRP barrier repair (RG-D) model (e) hybrid barrier repair (RH-P) models.

5.4.4.2 Deck thickness effect

The effect of the deck thickness on the overall behaviour of the five base barriers was investigated. Five realistic deck thicknesses were chosen (175 mm, 200 mm, 225 mm, 250 mm, and 275 mm) with the minimum deck thickness (175 mm) being the minimum deck thickness allowed by S6:19. Results of these models are summarized in Table 5.5.

DS models show increasing strength and stiffness with an increase in deck thickness as shown in Figure 5.11b, Figure 5.14a and Figure 5.14b. Although horizontal deflection in models DS-DT1 through DS-DT5 decrease with increasing deck thickness, the energy absorbed before failure increased due to the large increase in strength (Table 5.5). All of these models failed by steel yielding followed by concrete splitting, and all models achieved strengths exceeding the S6:19 limit of 113.3 kN (Figure 5.11b).

Models DG-DT1 through DG-DT4 showed similar behaviours and trends. With the increase in deck thickness, models exhibited increase in stiffness, strength (Figure 5.14b) and energy absorption before failure (Table 5.5). However, horizontal (Figure 5.14b) and vertical (Figure 5.15b) deflections decreased with the increase in deck thickness due to the increased stiffness. These models failed by concrete splitting due to diagonal shear. Model DS-DT5 exhibited a different response as shown in Figure 5.14b and Figure 5.15b with a relatively low increase in strength with the increase in deck thickness (Table 5.5). Although DS-DT5 has similar stiffness to DS-DT4, it failed at a higher horizontal deflection; this is attributed to the two-phased failure mode in which the barrier wall fails first, evident by excessive cracking and partial concrete cover separation, and then the system fails due to concrete splitting caused by the diagonal shear developed in the barrier-deck joint.

Repair models RG-P-DT1 through RG-P-DT5 and RG-D-DT1 through RG-D-DT5 had a similar behaviour to models DG-DT1 through DG-DT5 (Figures 5.14b, 5.14c, 5.14d, 5.15b, 5.15c, and 5.15d) with the exception that model RG-D-DT5 reached its peak capacity in the first phase of the two-phased failure mode. This is attributed to the inherent weakness in the concrete cold joint at the repair section in the deck slab. For these models, deck thicknesses of 175 mm and 200 mm are insufficient to develop the required strength (113.3 kN) as shown in Figure 5.11b.

Repair models of the hybrid steel-GFRP system exhibited different load-deflection responses both in the horizontal (Figure 5.14e) and vertical (Figure 5.15e) directions. Increasing the deck thickness for RH-P models from 175 mm to 250 mm increased stiffness (Figure 5.14e),

energy absorption before failure, and peak load (Table 5.5). However, increasing deck thickness beyond 250 mm adversely affects the peak load (Figure 5.11b). Models RH-P-DT1 and RH-P-DT2 showed a typical concrete splitting failure caused by diagonal shear in the barrier-deck joint. Unlike DS models, the steel reinforcement in the deck slab did not yield prior to failure. The lower stiffness of the vertical GFRP rebar in the barrier-deck junction caused this type of failure to occur and reduction in strength in comparison to DS counterpart models. RH-P-DT3 and RH-P-DT4 experienced the two-phased failure mode with the maximum capacity reached in the second phase. The failure mode change is attributed to the increase in diagonal shear capacity due to the increase in deck thickness. Nonetheless, increasing deck thickness to 275 mm (RH-P-DT5) prevents development of diagonal shear failure and increases the stiffness of the deck slab compared to the barrier wall. This stiffness discrepancy prevents efficient distribution of moment between the deck and the barrier wall and leads to a barrier wall failure due to excessive cracking at the barrier-deck junction and partial concrete cover separation of the front face of the wall. The vertical deflection of RH-P-DT5 after reaching the peak load is compromised due the concrete cover separation of the back face of the barrier wall at the bottom corner of the barrier-deck joint (Figure 5.15e).

Table 5.5: Key results from models investigating varying deck thicknesses.

Model ID	Peak load, kN	Deflection at failure, mm	Energy absorbed before failure, kN.mm	Failure mode
DS-DT1	132.9	31.7	2638	Yield-concrete splitting
DS-DT2	156.6	26.7	2705	Yield-concrete splitting
DS-DT3	183.9	23.5	2835	Yield-concrete splitting
DS-DT4	208.5	23.5	3380	Yield-concrete splitting
DS-DT5	230	22.2	3563	Yield-concrete splitting
DG-DT1	91.3	52.5	3138	Concrete splitting
DG-DT2	108.3	46.5	3385	Concrete splitting
DG-DT3	128.8	42.2	3662	Concrete splitting
DG-DT4	147.2	42.2	4279	Concrete splitting
DG-DT5	150.6	48.5	5572	Two-phased
RG-P-DT1	87.9	50.5	2950	Concrete splitting
RG-P-DT2	107.4	45.6	3270	Concrete splitting
RG-P-DT3	124.8	42.2	3628	Concrete splitting
RG-P-DT4	143.1	41.6	4167	Concrete splitting
RG-P-DT5	149.6	47.5	5435	Two-phased
RG-D-DT1	91	42.6	2541	Concrete splitting
RG-D-DT2	109.7	37.6	2731	Concrete splitting
RG-D-DT3	128.5	35.7	3127	Concrete splitting
RG-D-DT4	146.8	34.3	3465	Concrete splitting
RG-D-DT5	146	29.3	3088	Two-phased
RH-P-DT1	105.6	26.7	1872	Concrete splitting
RH-P-DT2	127.9	24.8	2181	Concrete splitting
RH-P-DT3	148.5	35.2	4044	Two-phased
RH-P-DT4	174.6	30.3	3945	Two-phased
RH-P-DT5	156.6	17.2	2038	Barrier wall failure

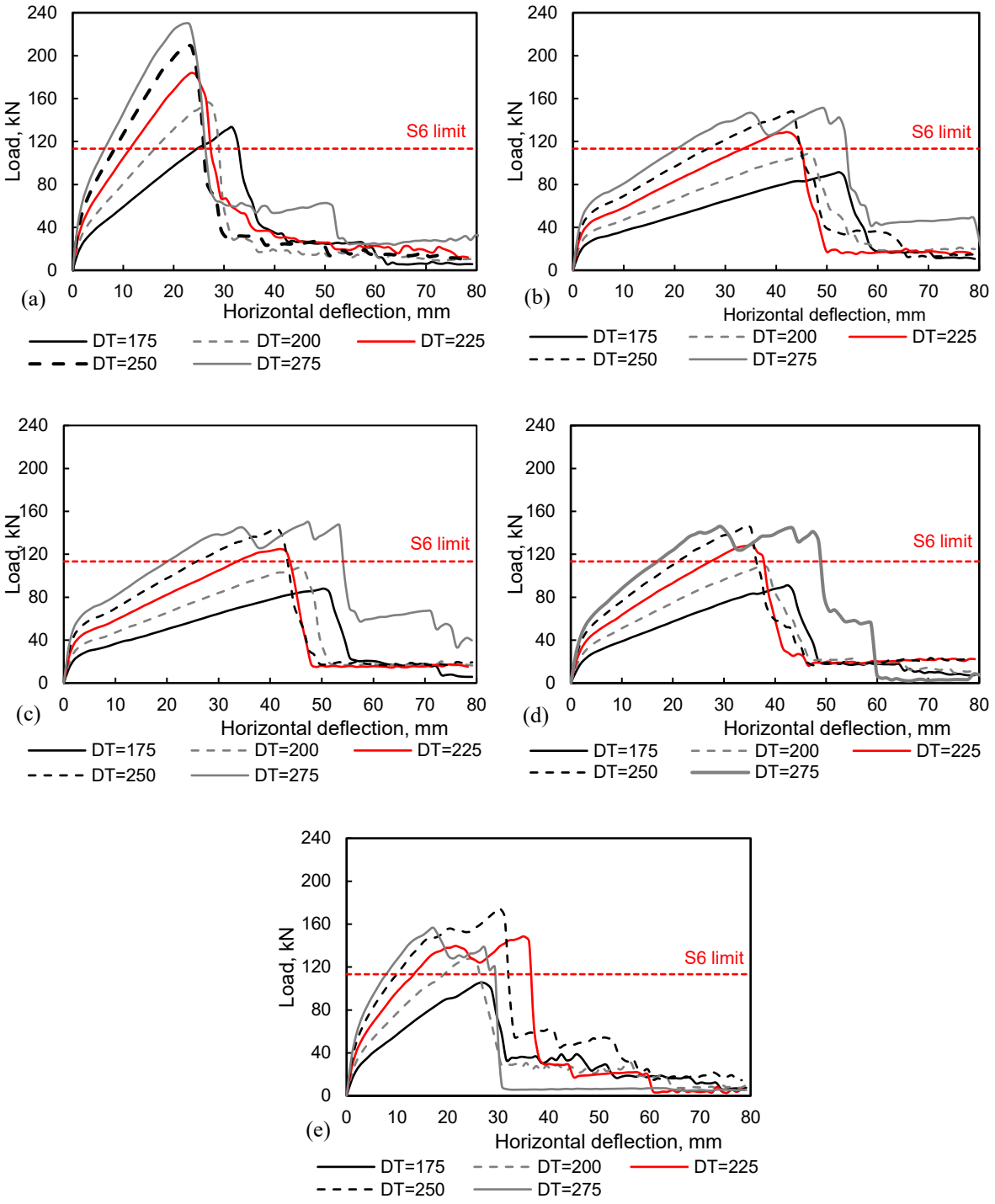

Figure 5.14: Load-horizontal deflection at the load point curves for multiple deck thicknesses of (a) steel barrier (DS) model (b) GFRP barrier (DG) model (c) GFRP barrier repair (RG-P) model (d) GFRP barrier repair (RG-D) model (e) hybrid barrier repair (RH-P) models.

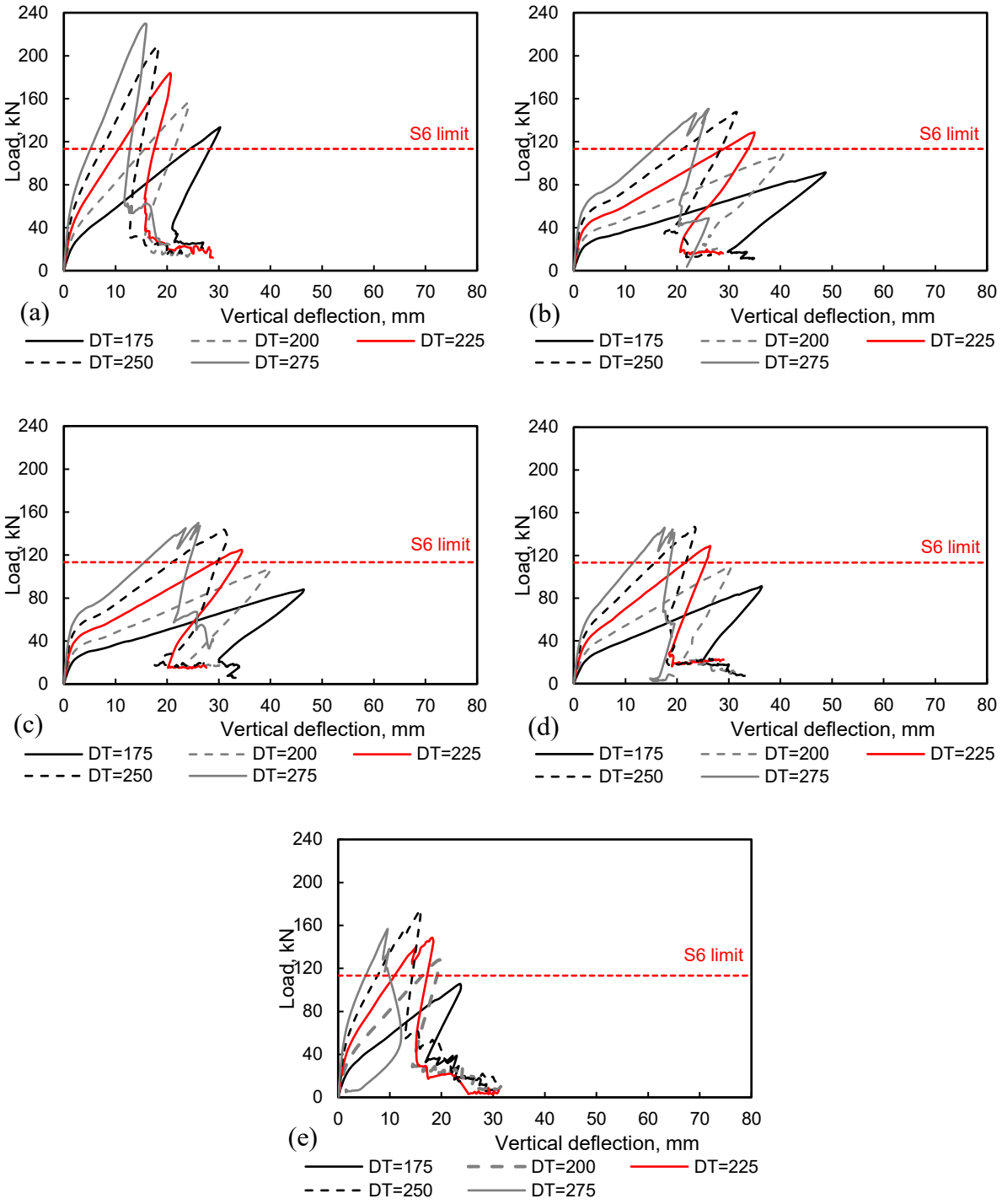

Figure 5.15: Load-vertical deflection (at the bottom corner of the barrier-deck joint) curves for multiple deck thicknesses of (a) steel barrier (DS) model (b) GFRP barrier (DG) model (c) GFRP barrier repair (RG-P) model (d) GFRP barrier repair (RG-D) model (e) hybrid barrier repair models (RH-P) models.

5.4.4.3 Effect of rebar spacing of the top mat of the deck slab reinforcement

The effect of deck thickness on the overall behaviour of the five base barrier models was investigated. Three practical rebar spacing of the top mat of the deck slab were chosen (100 mm, 150 mm, and 200 mm). Table 5.6 presents peak loads, horizontal deflections (at the load point) at peak loads, energy absorbed before failure, and modes of failure of barrier models with varying rebar spacing of the top mat of the deck slab. In general, barrier models deflect more with the increase in rebar spacing of the transverse reinforcement of the top mat of the deck slab, and this leads to increased energy absorption before failure. The stiffness of barrier overhangs is increased with the reduction of rebar spacing as shown in Figure 5.16. The load carrying capacity of barriers is decreased with increase in rebar spacing of the top mat (Figure 5.11c). A 200 mm rebar spacing is sufficient to achieve a barrier strength higher than the minimum required strength (113.3 kN), assuming perfect bond behaviour.

Models DS-SDT1 and DS-SDT2 display similar load-displacement response in the horizontal (Figure 5.16a) and vertical (Figure 5.17a) directions. They failed due to concrete splitting right after the transverse rebar of the top mat of the deck slab yielded. DS-SDT3, however, had slightly different behaviour. After the reinforcement yielded at a load of 155 kN, the barrier continued to resist the load with reduced stiffness until it failed at a peak load of 160 kN due to concrete splitting. This load represents the diagonal shear capacity of the overhang.

Models DG-SDT1 through DG-SDT3, and their repaired counterparts RG-P-SDT1 through RG-D-SDT3 had similar behaviours and trends with the increase in the rebar spacing of the transverse reinforcement of the top mat of the deck slab in both the horizontal (Figure 5.16b, 5.16c, and 5.16d) and vertical (Figure 5.17a, 5.17b, and 5.17c) directions.

Repair models RH-P-SDT1 through RH-P-SDT3 displayed two-phased modes of failure with different load-deflection behaviours. RH-P-SDT1 was stiffer in the horizontal (Figure 5.16e) and vertical (Figure 5.17e) directions than the other two models due to the increased reinforcement ratio. It reached a first peak load of 148 kN where the barrier wall gave in due to excessive bond cracks development and partial concrete cover separation along its front face. A second and higher peak load of 159.2 kN is reached and then the whole system failed due to concrete splitting caused by diagonal shear. RH-P-SDT2 underwent a similar failure process with a lower peak load at failure. The reduced stiffness in RH-P-DST3 altered the behaviour of the model slightly. RH-P-DST3 reached a capacity of 136.4 kN at the first peak where the barrier wall started to fail. Then,

the steel yielded at the second peak and led to concrete splitting due to excessive tensile stresses caused by diagonal shear. The reduced rebar led to the reduction of diagonal shear resistance in the overhang joint.

Table 5.6: Key results from models investigating bar spacing in the top mat of the deck.

Model ID	Peak load, kN	Deflection at failure, mm	Energy absorbed before failure, kN.mm	Failure mode
DS-SDT1	203.4	20.6	2810	Concrete splitting
DS-SDT2	183.9	23.5	2835	Yield-concrete splitting
DS-SDT3	159.7	35.3	4346	Yield-concrete splitting
DG-SDT1	137.3	35.3	3428	Concrete splitting
DG-SDT2	128.8	42.2	3662	Concrete splitting
DG-SDT3	122.6	49.1	4042	Concrete splitting
RG-P-SDT1	135.2	32.4	3007	Concrete splitting
RG-P-SDT2	124.8	42.2	3628	Concrete splitting
RG-P-SDT3	118.8	48.1	3880	Concrete splitting
RG-D-SDT1	136.7	26.5	2453	Concrete splitting
RG-D-SDT2	128.5	35.7	3127	Concrete splitting
RG-D-SDT3	122.2	40.2	3347	Concrete splitting
RH-P-SDT1	159.2	33.2	4101	Two-phased
RH-P-SDT2	148.5	35.2	4044	Two-phased
RH-P-SDT3	136.4	24.5	2391	Two-phased

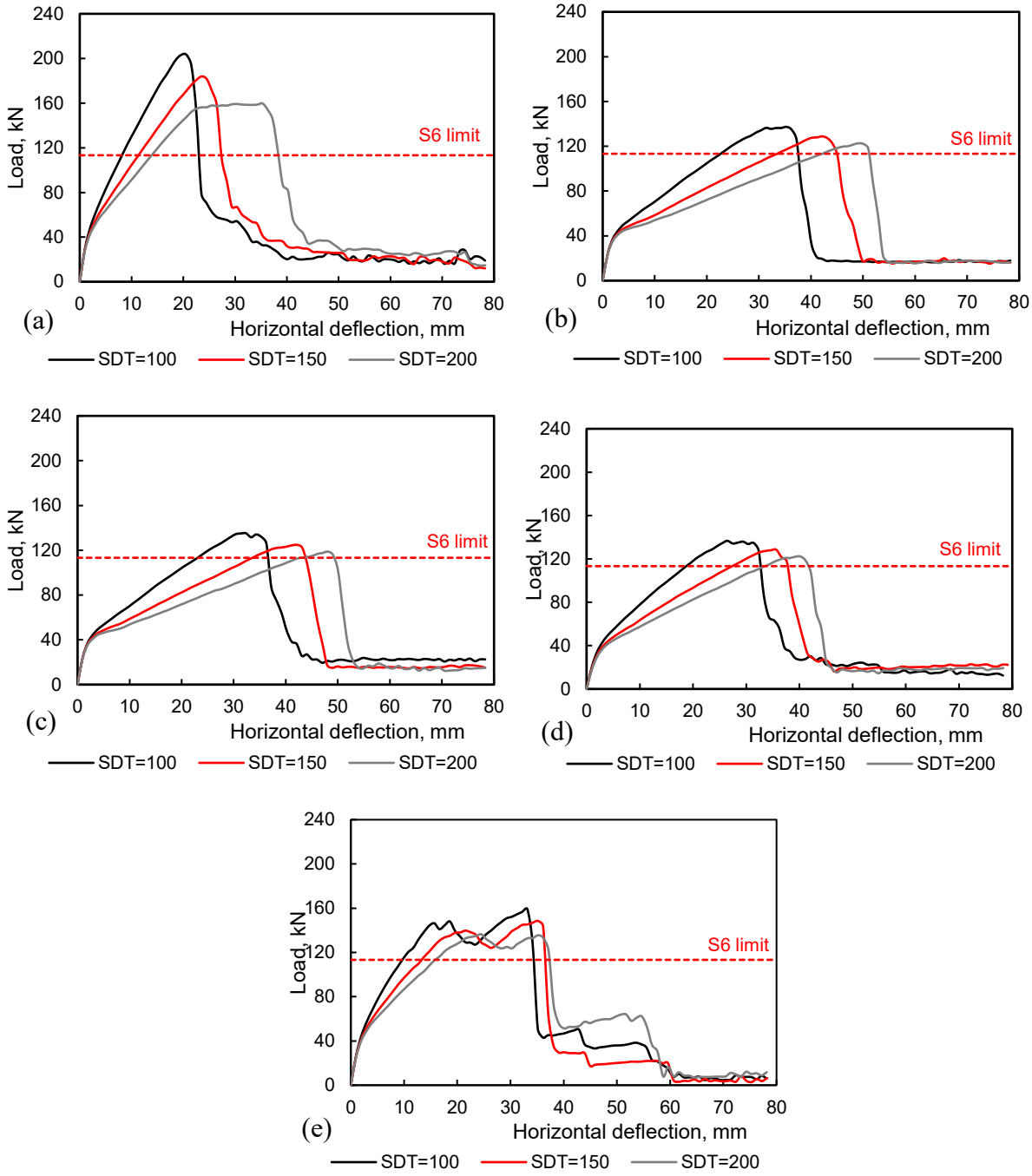

Figure 5.16: Load-horizontal deflection (at the load point) curves for rebar spacing of the top mat of the deck slab of (a) steel barrier (DS) model (b) GFRP barrier (DG) model (c) GFRP barrier repair (RG-P) model (d) GFRP barrier repair (RG-D) model (e) hybrid barrier repair (RH-P) models.

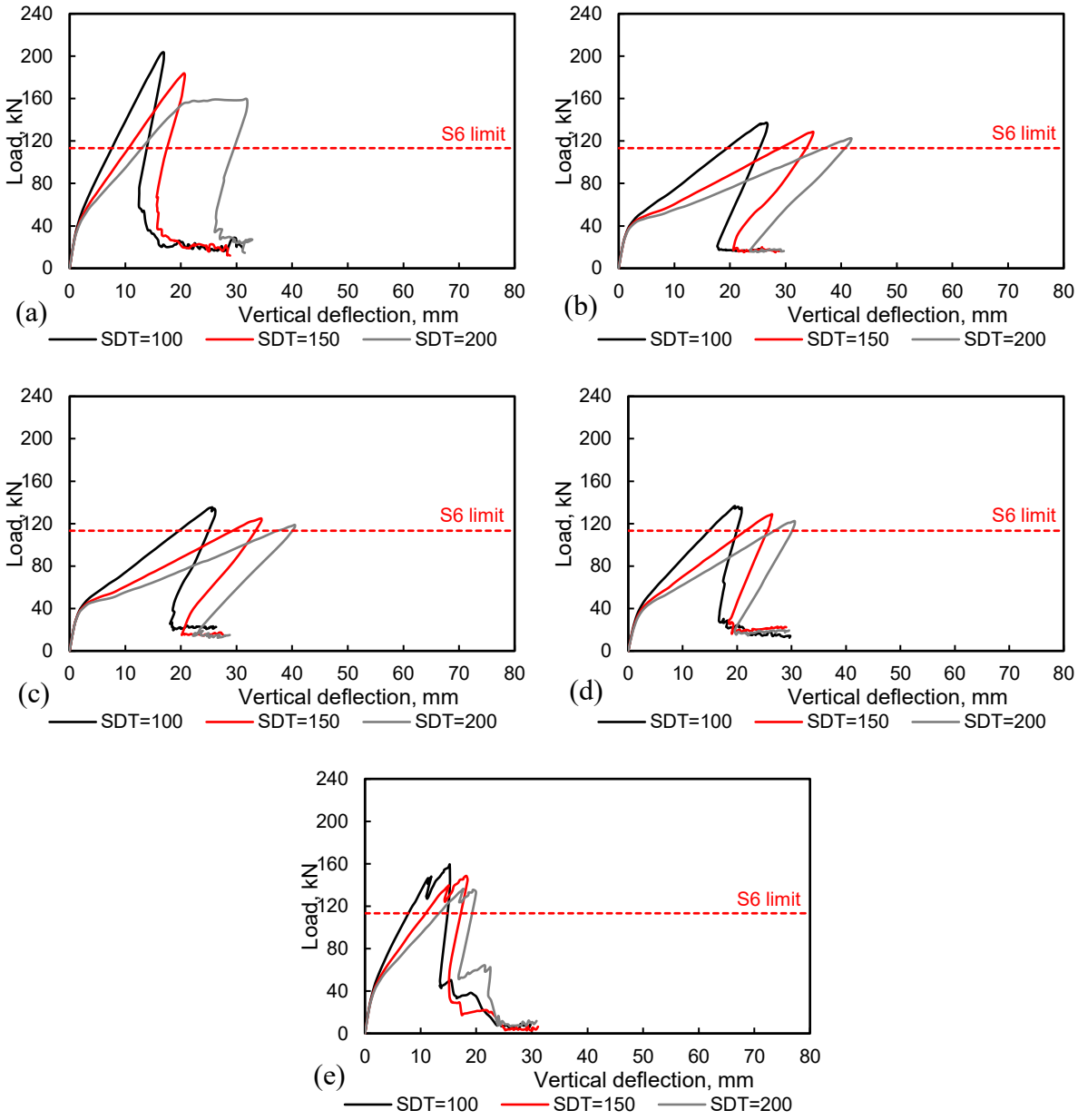

Figure 5.17: Load-vertical deflection (at the bottom corner of the barrier-deck joint) curves for multiple rebar spacing of the top mat of the deck slab of (a) steel barrier (DS) model (b) GFRP barrier (DG) model (c) GFRP barrier repair (RG-P) model (d) GFRP barrier repair (RG-D) model € hybrid barrier repair (RH-P) model.

5.4.4.4 Effect of rebar spacing of the front assembly of the parapet reinforcement

A set of practical bar spacings (100 mm, 150 mm, and 200 mm) of the front assembly of the parapet were considered with key results shown in Table 5.7. Generally, peak load drops with increasing bar spacing, and this reduction varies based on reinforcement type and barrier system. Horizontal deflection at failure is not heavily influenced by the bar spacing of the front assembly of the parapet

reinforcement in comparison to the bar spacing of the top mat of the deck slab reinforcement (Table 5.7). The strength of overhangs decreased with the increase in bar spacing as shown in Figure 5.11d. The bar spacing of the front assembly of barrier vertical reinforcement marginally affect the overhangs stiffness as shown in Figure 5.18 and Figure 5.19. A 200 mm bar spacing is sufficient to achieve the minimum required strength (113.3 kN), assuming perfect bond behaviour.

Models DS-SPF1 and DS-SPF3 exhibited similar load-displacement responses in the horizontal (Figure 5.18a) and vertical (Figure 5.19a) directions. All models failed due to concrete splitting right after the transverse bars of the top mat of the deck slab yielded. Models DG- SPF1 through DG-SPF3, and their repaired counterparts RG-P-SPF1 through RG-D-SPF3 showed similar behaviours and trends with the increase in the bar spacing in the front assembly of the barrier parapet in both the horizontal (Figure 5.18, 5.18c, and 5.18d) and vertical (Figure 5.19b, 5.19c, and 5.19d) directions. A concrete splitting failure mode was observed in these models. The energy absorption reduced with the increase in bar spacing (Table 5.7).

The tighter vertical spacing in the front assembly of the parapet of model RH-P-SPF1 prevented the first phase of the two-phased failure mode. Hence, RH-P-SPF1 had a single peak (Figure 5.18e and Figure 5.19e) and failed due to concrete splitting in the barrier-deck joint. However, RH-P-SPF2 and RH-P-SPF2 displayed two-phased failure modes with similar behaviours in the horizontal (Figure 5.18e) and vertical (Figure 5.19e) directions. The reduced ratio of vertical reinforcement led to reduction of diagonal shear resistance in the overhang joint.

Table 5.7: Key results from models investigating varying bar spacing of the front assembly of the parapet reinforcement.

Model ID	Peak load, kN	Deflection at failure, mm	Energy absorbed before failure, kN.mm	Failure mode
DS-SPF1	190	23.8	2928.6	Yield-concrete splitting
DS-SPF2	183.9	23.5	2835.9	Yield-concrete splitting
DS-SPF3	177.5	23.8	2805.8	Yield-concrete splitting
DG-SPF1	137.4	44.6	4063.9	Concrete splitting
DG-SPF2	128.8	42.2	3662.4	Concrete splitting
DG-SPF3	121.6	39.6	3263.1	Concrete splitting
RG-P-SPF1	131.1	42.6	3760.9	Concrete splitting
RG-P-SPF2	124.8	42.2	3628.7	Concrete splitting
RG-P-SPF3	120.3	39.6	3248.9	Concrete splitting
RG-D-SPF1	135.3	35.7	3231.4	Concrete splitting
RG-D-SPF2	128.5	35.7	3127.3	Concrete splitting
RG-D-SPF3	121.8	32.7	2693.5	Concrete splitting
RH-P-SPF1	159.6	23.5	2618	Concrete splitting
RH-P-SPF2	148.5	35.2	4044.4	Two-phased
RH-P-SPF3	140.2	36.1	3943.7	Two-phased

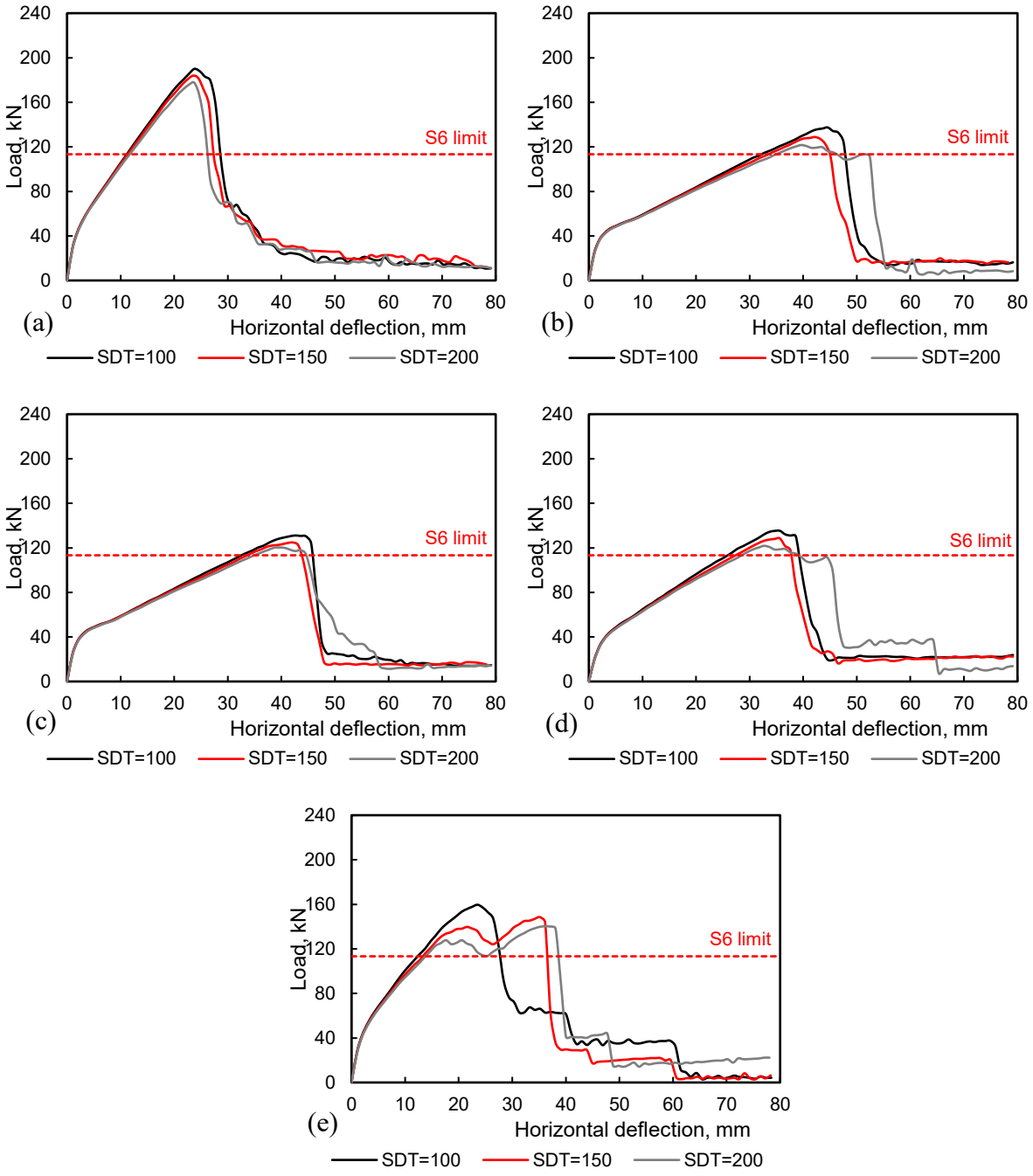

Figure 5.18: Load-horizontal deflection (at the load point) curves for rebar spacing of the front assembly of the parapet reinforcement of (a) steel barrier (DS) model (b) GFRP barrier (DG) model (c) GFRP barrier repair (RG-P) model (d) GFRP barrier repair (RG-D) model (e) hybrid barrier repair (RH-P) model.

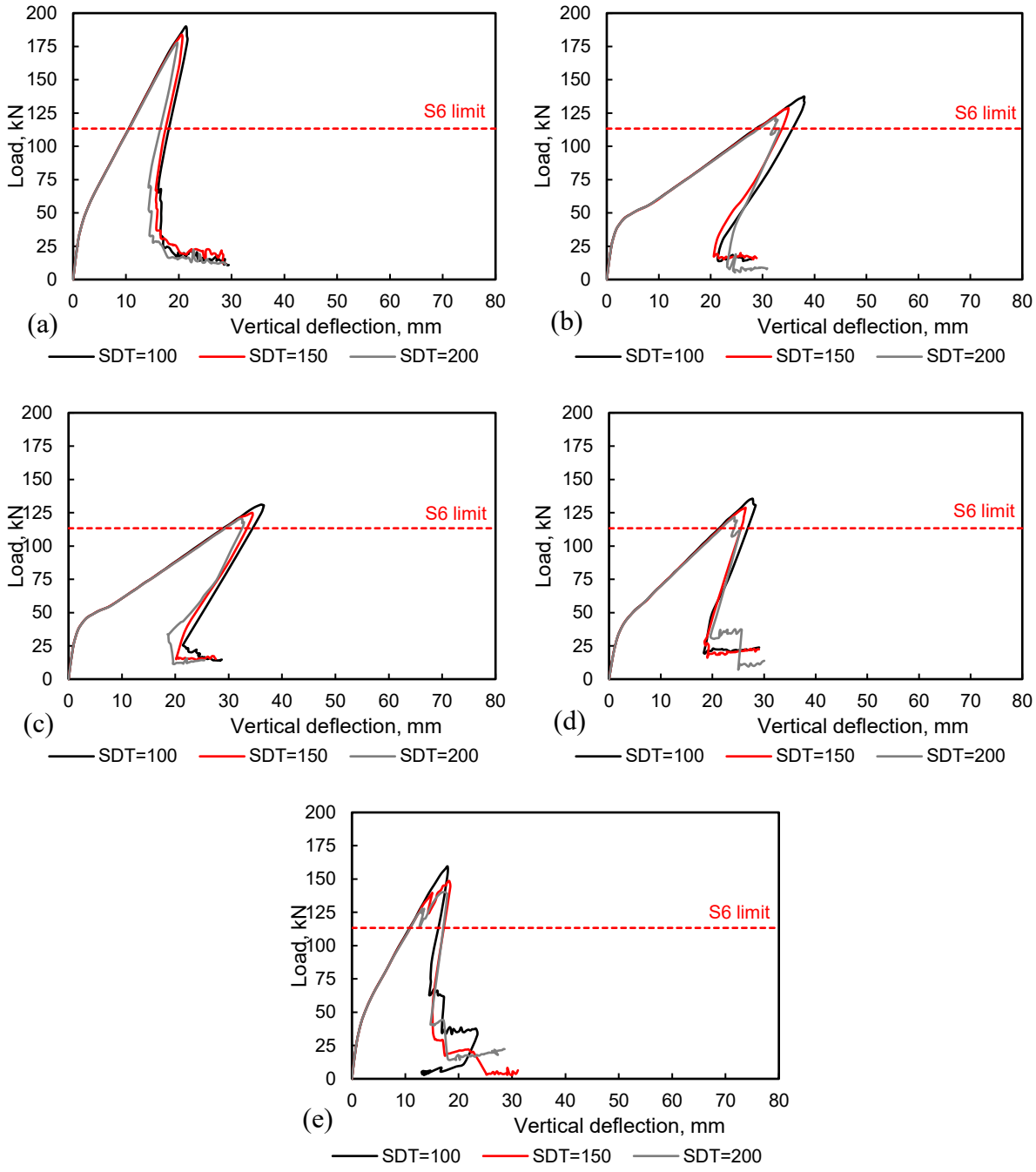

Figure 5.19: Load-vertical deflection (at the bottom corner of the barrier-deck joint) curves for multiple rebar spacing of the front assembly of the parapet reinforcement of (a) steel barrier (DS) model (b) GFRP barrier (DG) model (c) GFRP barrier repair (RG-P) model (d) GFRP barrier repair (RG-D) model (e) hybrid barrier repair (RH-P) model.

5.4.4.5 Effect of doweled rebar spacing of the top mat of the deck slab reinforcement

Four centre-to-centre bar spacings (50 mm, 100 mm, 150 mm, and 200 mm) were studied to examine the effect of doweled bar spacing of the top mat of the deck reinforcement on the repair

efficiency and overall behaviour of barrier overhangs, four practical centre-to-centre bar spacings were studied with key results summarized in Table 5.8.

Horizontal deflection at failure increases with increased doweled bar spacing due to the reduced stiffness of the section. The stiffness of overhangs increases for tighter bar spacings (Figure 5.20 and Figure 5.21). Models RG-D-DSD2 through RG-D-DSD4 had similar load-deflection responses and failed due to concrete splitting in the barrier-deck joint. RG-D-DSD1, however, behaved differently and failed at barrier-deck interface. First, at a peak load of 152 kN barrier cracks widened at the deck interface, and the concrete cover on the front face separates. Then, the barrier failed due to concrete splitting in the barrier-deck joint.

Table 5.8: Key results from models with varying doweled rebar spacing of the top mat of the deck slab reinforcement.

Model ID	Peak load, kN	Deflection at failure, mm	Energy absorbed before failure, kN.mm	Failure mode
RG-D-DSD1	152.1	26.7	2860.9	Two-phased
RG-D-DSD2	137.1	29.7	2752.5	Concrete splitting
RG-D-DSD3	128.5	35.7	3127.3	Concrete splitting
RG-D-DSD4	122.4	37.6	3115	Concrete splitting

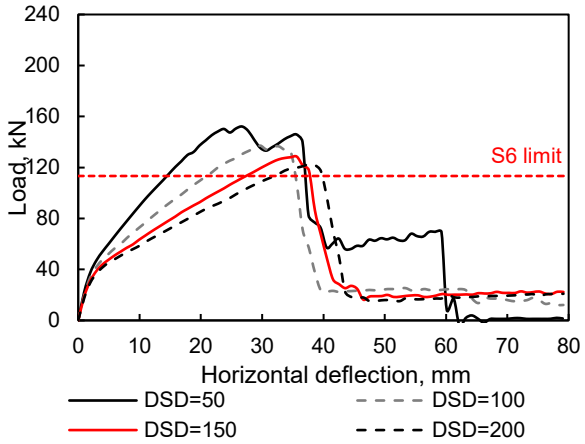

Figure 5.20: Load-horizontal deflection (at the load point) curves for doweled rebar spacing of the top mat of the deck slab reinforcement of GFRP barrier repair (RG-D) model.

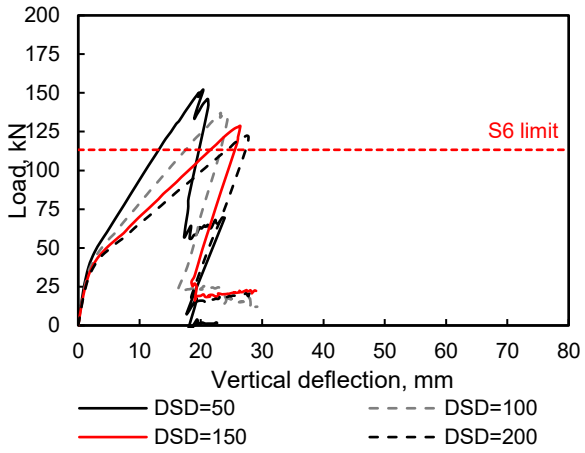

Figure 5.21: Load-vertical deflection (at the bottom corner of the barrier-deck joint) curves for multiple doweled rebar spacing of the top mat of the deck slab reinforcement of GFRP barrier repair (RG-D) model.

5.4.4.6 Effect of doweled bar spacing of the front assembly of the barrier reinforcement

The effect of vertical doweled rebar spacing of the front assembly of the parapet reinforcement on the repair efficiency and overall behaviour of barrier overhangs was studied using four practical bar spacings (50 mm, 100 mm, 150 mm, and 200 mm). Key results from these models are shown in Table 5.9.

The horizontal deflection at failure decreased with an increase in doweled bar spacing. However, trend was not consistent in hybrid barrier overhangs due to the change in behaviour and failure mode beyond a 100 mm spacing (Figure 5.22b and Figure 5.23b)

Models RG-P-DSP2 through RG-P-DSP4 simulating repair of damaged GFRP-RC barriers and showed consistent behaviours and reduction of peak capacity with the increase in the doweled bar spacing of the vertical reinforcement of the front assembly of the barrier parapet in both the horizontal (Figure 5.22a) and vertical (Figure 5.23a) directions. However, RG-P-DSP1 had a larger increase in strength and stiffness for decreased bar spacings relative to the other models. A concrete splitting failure were observed in all of these models.

Models RH-P-DSP1 and RH-P-DSP2 failed due to concrete splitting caused by diagonal shear stresses. The top mat of transverse steel reinforcement in the deck yielded right before barrier failure in RH-P-DSP1. The increased number of doweled bars improved diagonal shear capacity; decreasing doweled bar spacing reduces shear capacity and leads to the two-phased failure mode as seen in RH-P-DSP3 and RH-P-DSP4 (Figure 5.23b). These models failed because of the

excessive bond cracks and partial concrete cover separation of the parapet front face in the first phase, and then eventually collapsed due concrete splitting in the barrier-deck joint.

Table 5.9: Key results from barrier models with varying doweled rebar spacing of the front assembly of the parapet reinforcement.

Model ID	Peak load, kN	Deflection at failure, mm	Energy absorbed before failure, kN.mm	Failure mode
RG-P-DSP1	151.7	48.1	4725.9	Yield-concrete splitting
RG-P-DSP2	131	42.2	3723.1	Concrete splitting
RG-P-DSP3	124.8	42.2	3628.7	Concrete splitting
RG-P-DSP4	120.1	40.2	3333	Concrete splitting
RH-P-DSP1	173.9	23.5	2778.9	Yield-concrete splitting
RH-P-DSP2	159.6	23.5	2618	Concrete splitting
RH-P-DSP3	148.5	35.2	4044.4	Two-phased
RH-P-DSP4	140.2	36.1	3943.7	Two-phased

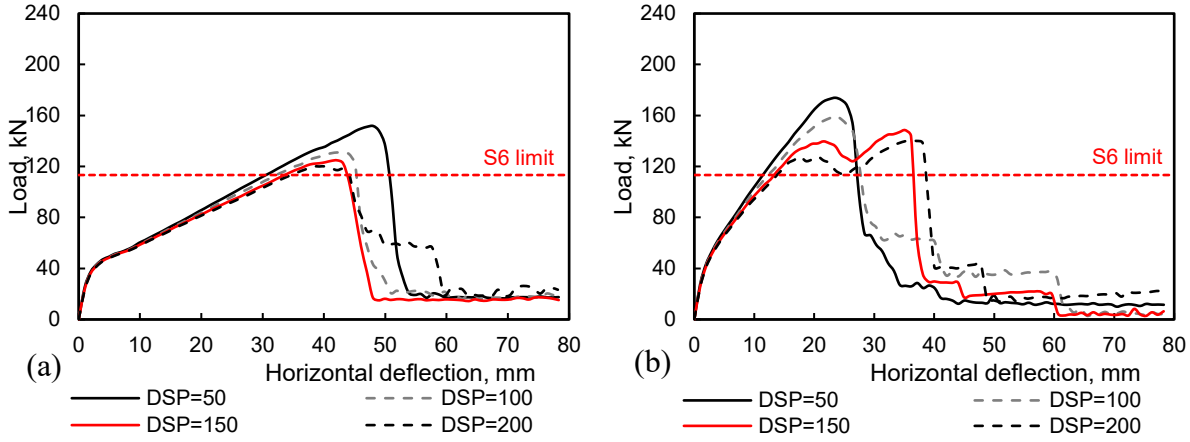

Figure 5.22: Load-horizontal deflection (at the load point) curves for doweled rebar spacing of the front assembly of the parapet reinforcement of (a) GFRP barrier repair (RG-P) model (b) hybrid barrier repair (RH-P) models.

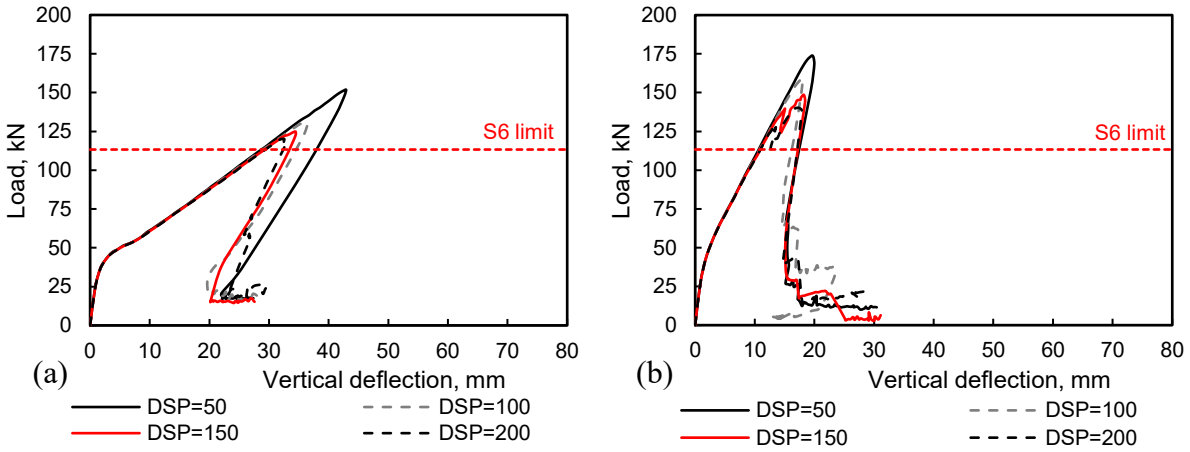

Figure 5.23: Load-vertical deflection (at the bottom corner of the barrier-deck joint) curves for multiple doweled rebar spacing of the front assembly of the parapet reinforcement of (a) GFRP barrier repair (RG-P) model (b) hybrid barrier repair (RH-P) models.

5.4.4.7 Effect of embedment length of doweled bars in the top mat of the deck slab

To investigate the effect of embedment length of the doweled bars in the top mat of the deck reinforcement on the repair efficiency and overall behaviour of overhangs, four bar embedment depths were studied (300 mm, 500 mm, 700 mm, and 900 mm). Table 5.10 presents general results from these models.

The horizontal deflection at failure decreases with increases in the embedment length of doweled bars. At first glance, the embedment length of doweled bars in the deck does not appear to have a notable effect on barrier strength (Figure 5.11g). However, the perfect bond assumption in modeling eclipses the influence of embedment length on the barrier repair efficiency. Models RG-D-EDD1 through RG-D-EDD4 failed due to concrete splitting caused by diagonal shear stresses with a recruitment of around 25% of the ultimate GFRP strength at failure. The stiffness of barrier models increased with the increase of embedment length of the doweled bars as shown in Figure 5.24 and Figure 5.25.

Table 5.10: Key results from barrier models with varying embedment length of doweled rebar in the top mat of the deck slab.

Model ID	Peak load, kN	Deflection at failure, mm	Energy absorbed before failure, kN.mm	Failure mode
RG-D-EDD1	128.8	40.6	3525.7	Concrete splitting
RG-D-EDD2	129.3	37.6	3264.1	Concrete splitting
RG-D-EDD3	128.5	35.7	3127.3	Concrete splitting
RG-D-EDD4	128.8	33.7	2952	Concrete splitting

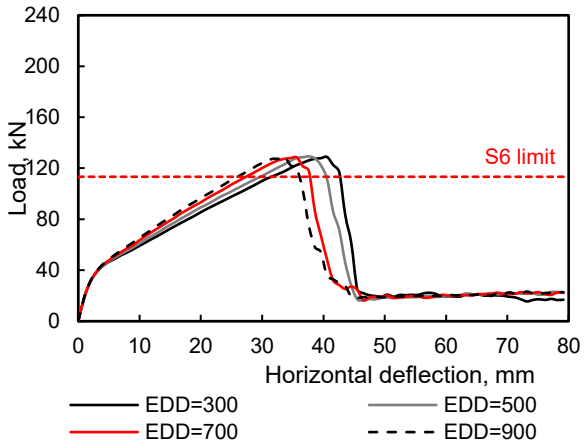

Figure 5.24: Load-horizontal deflection (at the load point) curves for different embedment lengths of the doweled rebar of the top mat of the deck slab reinforcement of GFRP barrier repair (RG-D) model.

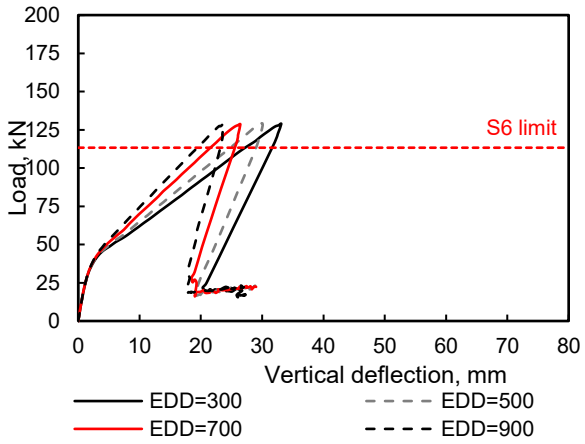

Figure 5.25: Load-vertical deflection (at the bottom corner of the barrier-deck joint) curves for multiple embedment lengths of the doweled rebar of the top mat of the deck slab reinforcement of GFRP barrier repair (RG-D) model.

5.5 CHAPTER SUMMARY AND CONCLUSION

This chapter discussed VecTor 2 simulations of 85 single-slope AT TL-4 barrier overhangs. The first part of the chapter addressed the results of modeling the five barriers presented in Chapter 4 while the second part discussed the effect of changing the overhang length, deck thickness, spacing of the deck top mat reinforcement, spacing of the parapet front vertical bar assembly, top dowelled reinforcement spacing in the deck, front dowelled reinforcement spacing in the parapet, and embedment length of the deck dowels on the modelled barrier response. The following was observed from these models:

1. Assuming perfect bond in modeling the bridge barrier overhangs overestimates their deflections at failure and the system capacity due to neglecting the large bond stresses at the barrier-deck joint. This influence is sensitive to embedment length and reinforcement anchorage (e.g. straight or headed bars). For the majority of models in this chapter, assuming perfect bond gave reasonable estimates of peak load and deflection at failure. However, simulations of doweled reinforcement of barrier parapets may not be as accurate as the other simulations due to the possible change of failure mode with the change in embedment length. Using additional anchorage (e.g. reinforcement hooks, headed bars) is expected to provide a bond-slip responses similar to perfect bond conditions.
2. Reinforcing single-slope AT TL-4 bridge barriers with GFRP reinforcement of the same ratio of its steel reinforced counterpart is a viable option. The GFRP-RC barrier overhang achieved 70.1% of the ultimate load capacity of its steel counterpart and exceeded the S6:19 strength limit by a ratio of 1.14.

3. Both repair scenarios for GFRP reinforced barrier overhangs were effective in restoring the original design capacity. In the case of repairing a damaged barrier wall, the restored capacity was 97% of the original, and in the case of repairing a damage that extends to the deck slab, full capacity was restored. However, it should be noted that the assumption of perfect bond may overshadow a small percentage of the lost capacity.
4. Repairing damaged wall of steel RC barrier overhangs with GFRP bars is feasible and may restore up to 80% of the barrier capacity.
5. Increasing the overhang length has little influence on the barrier overhang capacity but it reduces the stiffness and increases deflections.
6. Increasing the deck thickness of barrier overhangs increases the capacity and stiffnes. However, increasing the deck thickness beyond 250 mm for GFRP and hybrid barrier overhang adversely affects load capacity and alters the failure mode.
7. Peak load and stiffness reduce with the increase in the vertical bar spacing of the front assembly of the barrier wall reinforcement and the transverse bar spacing of the top mat of the deck slab reinforcement. Of these two situations, the effect of the deck slab bar spacing is more pronounced.
8. Increasing the number of doweled bars of the top mat in a repaired deck slab increases the capacity and stiffness of repaired barrier overhangs. Increasing the number of doweled bars of the front assembly in a repaired barrier wall has the same effect.
9. The embedment length of doweled bars in the top mat of the deck does not appear to have a notable effect on barrier overhang strength and because of the perfect bond assumption which eclipses the influence of embedment length on the repair efficiency.

5.6 CHAPTER RECOMMENDATIONS

Several recommendations are concluded based on the results presented in this chapter:

1. Remodeling the presented models in this chapter with the inclusion of bond-slip behaviour ‘imperfect bond’ to study this effect on some of the parameters, and to what extent does the bond-slip response affects capacity and stiffness of barrier overhangs.
2. Carry on the testing described in Chapter 4 to validate the base models, and to assess the accuracy of the simulation assumptions and results of the parametric study.
3. Build 3D models of the barrier overhang to simulate the realistic two-way behaviour of barrier walls, and to compare those models to the models presented in this chapter.

6 SUMMARY AND CONCLUSIONS

This chapter provides a summary, conclusions, and recommendations from the analytical investigation of GFRP-RC bridge barriers, and their repair scenarios and techniques.

6.1 SUMMARY

Chapter 2 presented a literature review of GFRP-RC bridge barriers and their repair techniques. Chapter 3 discussed the replacement of steel reinforcement in bridge barriers, and two proposed repair techniques on GFRP-RC bridge barriers. Different designs were simulated and analyzed in VecTor2 to study the response of steel-RC barriers, GFRP-RC barriers, and barriers simulating the proposed repair techniques. A parametric study was carried out to investigate the effect of some parameters on the effectiveness of one of the proposed repair techniques. Chapter 4 discussed preparations for a future static test program that investigates the structural performance of GFRP-RC barriers and the effectiveness of repairing them using the doweling repair technique. Chapter 5 focused on modeling the barrier overhangs presented in Chapter 4 with the inclusion of a parametric study on to assess the influence of designs (e.g. deck thickness, dowelled bar spacing) on barrier overhangs, and to find optimal design values.

6.2 CONCLUSIONS

The following conclusions are drawn from the thesis:

1. A literature review on the state of GFRP reinforcement, RC bridge barriers and decks, and previous experimentation on GFRP-RC bridge barriers and their repair was provided in Chapter 2. This completes Task 1 of the research objective.
2. The first part of Chapter 3 provided an analytical investigation on evaluating the feasibility of replacing steel reinforcement with GFRP reinforcement in bridge barriers. Reinforcing bridge barriers with 20M (#6) GFRP rebar achieved 92% of the ultimate load capacity of its counterpart model reinforced with 15M steel bars. This addressed parts of Task 2, 3 and 4 of the research objective.
3. The second part of Chapter 3 investigated the efficiency of two proposed repair techniques in restoring GFRP-RC barriers. The two proposed doweling repair techniques for GFRP-RC barriers, namely single-headed GFRP-FRC repair and single-headed GFRP-RC repair, proved to be effective in restoring the barrier capacity, and they achieved ultimate load capacities of 93.7 kN and 88.8 kN, respectively, which represent 101.8% and 96.4%, respectively, of the

as-designed barrier model strength. Repairing bridge barriers with FRC and a single assembly of GFRP bars (GFRP-FRC repair) is more efficient in restoring the undamaged GFRP barrier capacity. This fulfils Task 5 of the research objective.

4. An experimental testing proposal of five bridge barrier overhangs was planned to be carried out in the lab. Material (e.g. formwork, GFRP bars) to build these five specimens were procured. The fabrication of these specimens is discussed in more detail in Chapter 4. Reinforcing bars were instrumented with strain gauges based on anticipated high stress concentration areas in rebars according to the FEA presented in Chapter 3 and engineering judgement. The component of the load frame for the static testing of barriers was designed and procured. Other materials and equipment to build and repair the barrier were procured, such as chemical adhesive (epoxy), a hammer drill, and drill bits. Static testing was prevented by a complete shutdown of the University of Alberta's structural testing facilities for over seven months due to the COVID-19 pandemic. This addresses parts of Task 2, 3, 4 and 6 of the research objective.
5. Assuming perfect bond behaviour in barrier overhang models overestimates their deflections at failure and load capacities, in general, due to the negligence of large bond stresses in critical areas. However, this influence is small in cases where the embedment length of bars is not a concern. Reinforcing single-slope AT TL-4 bridge barriers with equivalent reinforcement ratio as its steel reinforced counterpart is a feasible option. The GFRP-RC barrier overhang achieved 70% of the ultimate load capacity of its steel counterpart and exceeds the S6:19 strength limit by a ratio of 1.14 This fulfills the analytical part of Tasks 2, 3, and 4 of the research objectives.
6. Both repair scenarios for GFRP reinforced barrier overhangs presented in Chapter 5 were effective in restoring the capacity of the original design. However, the load capacity of the simulated barrier overhangs is influenced by the perfect bond assumption. Repairing damaged walls of steel RC barrier overhangs with GFRP bars is feasible and may restore 80% of the steel barrier capacity depending on embedment depth and doweled bar spacing. This accomplished Task 6 of the research objective.

Overall, this thesis evaluated the replacement of steel rebar with GFRP bars in bridge barrier-deck overhangs, the feasibility of repairing damaged GFRP-RC barrier-deck overhangs using the doweling repair technique, and the feasibility of two proposed repair techniques for GFRP-RC

barriers. An equivalent reinforcement ratio design of GFRP-RC barriers to their steel counterpart is viable; however, it is more advantageous to use larger GFRP bars to account for the smaller stiffness of GFRP relative to steel, as seen in Chapter 3. All repair techniques and scenarios were successful in restoring a large part of the original barrier capacity.

6.3 RECOMMENDATION FOR FUTURE WORK

This analytical program studied the structural performance of steel and GFRP-RC bridge barriers, their repair techniques and scenarios. As it is the initial work of more studies to come, there are several recommendations for future work based on the outcomes of this thesis.

1. Evaluating all of the presented models in Chapter 3 and 5 using 'imperfect bond' models to study the effect of bond-slip on design/repair parameters, and to study the extent bond-slip affects the load capacity and stiffness of barrier overhangs.
2. Full scale static testing of as-built prototypes of bridge barriers as well as the repaired ones to verify the feasibility of the proposed repair techniques and scenarios for GFRP-RC bridge barriers presented in Chapter 3 and 5.
3. Carry on the testing described in Chapter 4 to validate the base models, and to assess the accuracy of the simulation assumptions and results of the parametric study.
4. Running 3D models of the barrier overhangs that simulate realistic two-way behaviours of barrier walls, then comparing results from those models to the one-way models presented in this chapter.
5. Full scale static testing of bridge barriers with widths exceeding three metres is recommended to capture the two-way behaviour of barriers and its contribution to the ultimate load carrying capacity of bridge barriers.
6. Full scale dynamic testing (crash testing) should be performed to prove the crashworthiness of the proposed GFRP-RC bridge barrier repair techniques proposed in Chapter 4.

REFERENCES

AASHTO. 1989. *AASHTO Guide Specifications for Bridge Railings*, American Association of State Highway and Transportation Officials, Washington, D.C., USA.

AASHTO. 1994. Guide Specifications for the Distribution of Loads on Highway Bridges, American Association of State of Highway and Transportation Officials, Washington, DC,

AASHTO. 2007. *AASHTO LRFD Bridge Design Specification. 4th Edition*, American Association of State Highway and Transportation Officials, Washington, D.C., USA.

ACI 440.1R. 2015. "Guide for the Design and Construction of Structural Concrete Reinforced Fiber-Reinforced Polymer (FRP) Bars," American Concrete Institute, Farmington Hills, MI, USA.

ACI 440R-07. 2007. Report on fiber-reinforced plastic (FRP) reinforcement for concrete structures. ACI Committee 440, Farmington Hills, MI.

ACI Committee 355. 2001, “Evaluating the Performance of Post-Installed Mechanical Anchors in Concrete (ACI 355.2-01) .” American Concrete Institute, Farmington Hills, MI, 29 p.

ACI Committee 408. 2003. “Bond and development of straight reinforcing bars in tension (ACI 408R-03)”. American Concrete Institute, Farmington Hills, MI, 49 pp.

ACI Committee 440. 2008. Specification for carbon and glass fiber-reinforced polymer bar materials for concrete reinforcement, ACI 440.6-08. American Concrete Institute, Farmington Hills, MI.

Ahmed, E. and Benmokrane, B. 2011. Static Testing of Full-Scale Concrete Bridge Barriers Reinforced with GFRP Bars. American Concrete Institute, 275, 1-20.

Ahmed, E., Dulude, C. and Benmokrane, B. 2010. Static Testing of Alberta Transportation Concrete Bridge Barrier Walls of Type PL-2 Reinforced with GFRP and Steel Bars. Government of Alberta Transportation, Edmonton, Alberta, Canada.

Ahmed, E., Dulude, C. and Benmokrane, B. 2013. “Concrete Bridge Barriers Reinforced with Glass Fibre-Reinforced Polymer: Static Tests and Pendulum Impacts.” Canadian Journal of Civil Engineering 40, no. 11: 1050–59. https://doi.org/10.1139/cjce-2013-0019.

Ahmed, E., El-Salakawy, E, Benmokrane, B. 2008. Bond stress-slip relationship and development length of FRP bars embedded in concrete. Housing and Building National Research Center Journal، Vol. 4, no. 3, pp.79-95.

Ahmed, E., Matta, F. and Benmokrane, B. 2013. Steel post-and-beam barrier with GFRP-reinforced concrete curb and bridge deck connection. *Journal of Bridge Engineering*, 18(11), 1189-1197.

Alberson, D.C., Williams, W.F., Menges, W.L. and Haug, R.R. 2004. "Testing and Evaluation of The Florida Jersey Safety Shaped Bridge Rail," Report No. 9-8132-1, February, Texas Transportation Institute (TTI), The Texas A&M University System, College Station, Texas.

Alberta Transportation. 2017. *TL-4 Single Slope Concrete Bridge Barrier Details*, *Standard Drawings and Typical Detail Drawings, Drawing No. S-1650-17*, Alberta Transportation, Edmonton, Alberta, Canada.

Al-Dulaijan, S. U., Nanni, A., Al-Zahrani, M. M. and Bakis, C. E. 1996. Bond Evaluation of Environmentally Conditioned GFRP/Concrete System. *Proceedings of the Second International Conference on Advanced Composite Materials in Bridges and Structures (ACMBS-2)*, M. M. El- Badry, ed., Canadian Society for Civil Engineering, Montreal, Quebec, pp. 845-852.

Aperador, W., Bautista-Ruiz, J. and Chunga, K. 2015. Determination of the efficiency of cathodic protection applied to alternative concrete subjected to carbonation and chloride attack. Int. J. Electrochem. Sci. 10, 7073–7082.

Asplund, S.O. 1949. "Strengthening Bridge Slabs with Grouted Reinforcement", Journal of the American Concrete Institute, Vol. 20, No. 6, January, pp. 397-406.

ASTM A123-28T. 1928. Tentative Specification for Zinc (Hot-Galvanized) Coatings on Structural Steel Shapes, Plates and Bars and Their Products, ASTM International, Philadelphia, PA.

ASTM. A276/A276M. 2017. Standard Specification for Stainless Steel Bars and Shapes.

Azimi, H., Sennah, K., Tropynina, E., Goremykin, S., Lucic, S. and Lam, M. 2014. Anchorage Capacity of Concrete Bridge Barriers Reinforced with GFRP Bars with Headed Ends. *Journal of Bridge Engineering*, 9(19), 04014030.

Banthia, N., Al-Asaly, M., and Ma, S. 1995. "Behavior of Concrete Slabs Reinforced with Fiber-Reinforced Plastic Grid," ASCE Journal of Materials in Civil Engineering, 7 (4), 643–652.

Barker, Richard M., and Puckett, Jay A. 2007. Design of Highway Bridges an LRFD Approach. 2nd Edition. Wiley John Wiley & Sons, Inc, Hoboken, NJ, USA.

Benmokrane, B., El-Salakawy, E., El-Gamal, S. and Goulet, S. 2007. Construction and Testing of an Innovative Concrete Bridge Deck Totally Reinforced with Glass FRP Bars: Val-Alain Bridge on Highway 20 East. Journal of Bridge Engineering, 12(5), 632-645. doi:10.1061/(asce)1084-0702(2007)12:5(632)

Benmokrane, B., El-Salakawy, E., El-Ragaby, A. and El-Gamal, S. 2011. Performance evaluation of innovative concrete bridge deck slabs reinforced with fibre- reinforced-polymer bars. Canadian Journal of Civil Engineering. 34. 298-310. 10.1139/l06-173.

Benmokrane, B., Tighiouart, B., and Chaallal, O. 1996. "Bond strength and load distribution of composite GFRP reinforcing bars in concrete." ACI Mat. J., 93(3).

Bentur, Arnon, Diamond, Sidney, and Berke, Neal S. 1997. *Steel Corrosion in Concrete,* E and FN Spon, New York, NY, 201 pp.

Berke, N. 2012. Reinforcing Steel Comparative Durability Assessment and 100 year Service Life Cost Analysis Report, Tourney Consulting Group, May 2012.

Broomfield, J.P. 2006. Corrosion of Steel in Concrete: Understanding, Investigation and Repair, 2nd edn. Taylor and Francis, London.

Buth C., William W., Bligh R., Menges W., and Haug R. 2003. "Performance of the txdot t202 (mod) bridge rail reinforced with fiber reinforced polymer bars." Report No. FHWA/TX-03/0-4138-3, November, Texas Transportation Institute (TTI), The Texas A&M University System, College Station, Texas. 98 pages.

CAN/CSA S806, 2012. "Design and Construction of Building Structures with Fibre-Reinforced Polymers," Canadian Standards Association, Mississauga, Ontario, Canada.

Canadian Standard Association (CSA). (2006). *Canadian Highway Bridge Design Code*, CAN/CSA S6-06, Rexdale, Ontario, Canada.

Canadian Standard Association (CSA). (2014a). *Canadian Highway Bridge Design Code*, CAN/CSA S6-14, Rexdale, Ontario, Canada.

Canadian Standards Association (CSA). (2014b). Commentary on CAN/CSA-S6-14, Canadian Highway Bridge Design Code, CAN/CSA S6.1-14, Rexdale, ON, Canada.

Canadian Standard Association (CSA). (2019). *Canadian Highway Bridge Design Code*, CAN/CSA S6:19, Rexdale, Ontario, Canada.

Chen, Wai-Fah, and Duan, Lian. 2000. Bridge Engineering Handbook. CRC Press, Boca Raton, FL, USA.

Chess, P. 1998. *Cathodic Protection of Steel in Concrete*. New York, NY, 187 pp.

Ehsani, M. R. 1993. "Glass-Fiber Reinforcing Bars," Alternative Materials for the Reinforcement and Prestressing of Concrete, J. L. Clarke, Blackie Academic & Professional, London, pp. 35-54.

Ehsani, M. R., Saadatmanesh, H. and Tao, S. 1995. "Bond of Hooked GFRP Rebars to Concrete", ACI Materials Journal (in press).

Ehsani, M. R., Saadatmanesh, H., and Tao, S. 1996. "Design Recommendation for Bond of GFRP Rebars to Concrete," Journal of Structural Engineering, V. 122, No. 3, pp. 247-254.

El-Salakawy, E. and Islam, M. 2014. Repair of GFRP-reinforced concrete bridge barriers. *ASCE Journal of Bridge Engineering,* 19(6), 04014016.

El-Salakawy, E., Benmokrane, B., Masmoudi, R., Brière, F. and Breaumier, E. 2003. Concrete Bridge Barriers Reinforced With Glass Fiber-Reinforced Polymer Composite Bars. ACI Struct. J., 100(6) 815–82.

El-Salakawy, E., Masmoudi, R., Benmokrane, B., Brière, F. and Desgagné, G. 2004. "Pendulum Impacts into Concrete Bridge Barriers Reinforced with Glass Fibre Reinforced Polymer Composite Bars". Canadian Journal of Civil Engineering. 31(4): 539-552. https://doi.org/10.1139/l04-006

El-Salakawy, E., Mufti, A. and Elragaby, A. 2010. "Laboratory Investigations on the Repair of GFRP-Reinforced Concrete Bridge Deck Slabs," Recent Advances in Maintenance and Repair of Concrete Bridges, ACI, SP-235, 20 p.

Fam, A. and Rizkalla, S. 2001. Behavior of axially loaded concrete-filled circular fiber-reinforced polymer tubes. ACI Struct J 2001;98(3): 280–9.

FHWA. 2009. Manual for Assessing Safety Hardware, (MASH 2009), Federal Highway Administration, Washington, DC.

Frosch, R. J., Labi, S. and Sim, C. 2014. Increasing bridge deck service life: Volume I—Technical evaluation (Joint Transportation Research Program Publication No. FHWA/IN/JTRP-2014/16). West Lafayette, IN: Purdue University. https://doi.org/10.5703/1288284315516.

Hassan, T., Rizkalla, S., Abdelrahman, A. and Tadros, G. 2000. "Fiber Reinforced Polymer Reinforcing Bars for Bridge Decks." Canadian Journal of Civil Engineering, 27, 839–849.

Hellriegel, E.J. 1968. Development of The Narrow Median Concrete Barrier In New Jersey, Presented at the 38th Annual Meeting of Institute of Traffic Engineers, August, 1968.

Jones, Denny A. 1996. *Principles and Prevention of Corrosion*, Second Edition, Prentice Hall, Upper Saddle River, New Jersey, 572 pp.

Khanna, O., Mufti, A., and Bakht B. 2000. "Experimental Investigation of the Role of Reinforcement in the Strength of Concrete Deck Slabs." Canadian Journal of Civil Engineering, 27, 475–480.

Khorramian, K. and Sadeghian, P. 2019. "Material Characterization of GFRP Bars in Compression Using a New Test Method." Journal of Testing and Evaluation 49, no. 2: 20180873.

Lorenzis, D. and Nanni, A. 2002 "Bond Between Near Surface Mounted FRP Rods and Concrete in Structural Strengthening," ACI Structures Journal, V. 99, No. 2, pp. 123-133.

Mallick, P. K. 1988. Fiber Reinforced Composites, Materials, Manufacturing, and Design, Marcell Dekker, Inc., New York, 469 pp.

Manning, David G. 1996. "Corrosion Performance of Epoxy-Coated Reinforcing Steel: North American Experience," *Construction and Building Materials*, Vol. 10, No. 5, Jul. pp. 349-365.

Masoudi, R. 2013. Adhesion of Epoxy Coating to Steel Reinforcement under Alkaline Conditions (Masters dissertation). Toronto, Ontario, University of Toronto. Retrieved July 22, 2020, fromhttps://tspace.library.utoronto.ca/bitstream/1807/43192/3/Masoudi_Rana_201311_MASc_thesis.pdf

Matta, F., Nanni, A., and Bank, L. C. 2007. Prefabricated FRP Reinforcement for Concrete Bridge Deck and Railing: Design, Laboratory Validation, and Field Implementation, Asia-Pacific Conference on FRP in Structures (APFIS 2007), S.T. Smith, 2007 International Institute for FRP in Construction.

McCrum, L. and Arnold, C. J. 1993. "Evaluation of Simulated Bridge Deck Slabs Using Uncoated, Galvanized, and Epoxy Coated Reinforcing Steel," *Research Report* No.R-1320, Michigan Department of Transportation, Lansing, MI.

McDonald, D. B., Pfeifer, D. W., and Sherman, M. R. 1998. "Corrosion Evaluation of Epoxy-Coated, Metallic Clad and Solid Metallic Reinforcing Bars in Concrete," *Publication* No. FHWA-RD-98-153, US Department of Transportation Federal Highway Administration.

Mitchell, G. 2005. "Pendulum Simulation of Vehicular Impact on Retrofit Bridge Barriers," M.S. Thesis, Department of Civil, Architectural and Environmental Engineering, The University of Texas at Austin, May 2005.

Mitchell, G., Tolnai, M., Gokani, V., Picon, R., Yang, S., Klingner, R.E. and Williamson, E.B. 2006. "Design of Retrofit Vehicular Barriers Using Mechanical Anchors," Report No. 0-4823-CT-1, October, Centre for Transportation Research (CRT), The University of Texas at Austin, Red River, Austin.

MMFX Steel, Material Properties and Design Considerations, MMFX2 (ASTM A1035/AASHTO MP18), 2011.

Nanni, A., Rizkalla, S., Bakis, C. E., Conrad, J. O. and Abdelrahman, A. A. 1998. Characterization of GFRP Ribbed Rod Used for Reinforced Concrete Construction. *Proceedings of the International Composites Exhibition (ICE-98)*, Nashville, Tenn., pp. 16A/1-6.

National Cooperative Highway Research Program NCHRP Report 350 Safety Performance Evaluation (NCHRP Report 350), 1993.

Nürnberger, U. 1996. "Stainless Steel in Concrete- State of the Art Report", European Federation of Corrosion Publications, No. 18.

Platt, S. and Harries, K. A. 2019. Proposed design methodology for titanium reinforcing bars in concrete. Engineering Structures, 178, 543-553. doi:10.1016/j.engstruct.2018.10.064

Pour-Ali, S., Dehghanian, C. and Kosari, A. 2015. Corrosion protection of the reinforcing steels in chloride-laden concrete environment through epoxy/polyaniline–camphorsulfonate nanocomposite coating. Corros. Sci. 90, 239–247.

Pyc, Wioleta, Weyers, R.E., Sprinkel, Michael M, Weyerw, R.M., Mokarem, D.W. and Dillard, J.G. 2000. "Performance of Epoxy-Coated Reinforcing Steel," *Concrete International,* Vol. 22, No. 2, Feb., pp. 57-62.

Rizkalla, S. and Tadros, G. 2003. FRP for prestressing of concrete bridges in Canada. ACI Special Publications, SP- 215, 75-90.

Rosenbaugh, S. K. 2007. Development of A TL-5 Vertical Faced Concrete Median Barrier Incorporating Head Ejection Criteria, University of Nebraska-Lincoln 527 Nebraska Hall, December 10, 2007.

Schell, H., Pianca, F., Wojick, C., Raven, R. and Berszakiewicz, B. 2005. The Performance of Epoxy-Coated Reinforcement- Experience of the Ontario Ministry of Transporation (MERO009). Toronto, Ontario, Ontario Ministry of Transportation Concrete Section.

Seible, F. 1996. "Advanced Composite Materials for Bridges in the 21 st Century." Proc., of the Advanced Composite Materials in Bridges and Structures, M. EI-Badry, editor, published by CSCE, Montreal, 1996, pp.17-30.

Sennah, K., Juette, B., Weber, W. and Witt, C. 2011. vehicle crash testing of a GFRP-reinforced PL-3 concrete bridge barrier. Proceedings of the 4th International Conference on Durability & Sustainability of Fibre Reinforced Polymer Composites for Construction and Rehabilitation, Québec City, Que. pp. 417–424.

Sennah, K., Tropynina, E., Goremykin, S., Lam, M., and Lucic, S. 2010. Concrete Bridge Barriers Reinforced with GFRP Bars with Headed Ends. Proceedings of the 8th Short and Medium Span Bridge Conference, Niagara Falls, Canada, 10p.

Shipilov, S. 2009. "What Corrosion Costs Canada; Or, Can We Afford to Ignore Corrosion?," In: C. Barry and P. Wanjara (Eds.), Materials Development and Performance of Sulphur Capture Plants, CIM, Montreal, Quebec, 2009, pp. 55-76.

Singh, S. 2015. Analysis and Design Of FRP Reinforced Concrete Structures. 3rd ed., Mcgraw-Hill Education, 2015.

Smith, J. and Virmani, Y. 1996. "Performance of Epoxy-Coated Rebars in Bridge Decks," *Report* No. FHWA-RD-96-092, Federal Highway Administration, Washington, D.C.

Tighiouart, B., Benmokrane, B. and Gao, D. 1998. "Investigation of bond in concrete member with fibre reinforced polymer (FRP) bars." Construction and Building Materials, V. 12, pp. 453-462.

Trejo, D., Aguiniga, F., Buth, E. C., James, R. W., and Keating, P. B. 2000. "Performance of the txdot t202 (mod) bridge rail reinforced with fiber reinforced polymer bars." Report No. FHWA-0111520-1, December, Texas Transportation Institute (TTI), The Texas A&M University System, College Station, Texas.

Van Dyke, Chris, Bobby Meade, Danny Wells, Sudhir Palle, and Theodore Hopwood II. 2017. "Long- Term Corrosion Protection of Bridge Element Reinforcing Materials in Concrete." Lexington, KY, 2017.

Virmani, Y. and Clemena, G. 1998. "Corrosion Protection- Concrete Bridges," *Report* No. FHWA-RD-98-088, Federal Highway Administration, Washington, D.C.

Virmani, Y., Clear, K. and Pasko, T. 1983. "Time-to-Corrosion of Reinforcing Steel in Concretes, Vol.5: Calcium Nitrite Admixture or Epoxy-Coated Reinforcing Bars as Corrosion

Protection Systems." Report No. FHWA/RD-83/012, Federal Highway Administration, Washington, D. C., 1983.

Wight, James K., and James G. MacGregor. 2012. Reinforced Concrete: Mechanics and Design. 6th ed. Boston, MA: Pearson Education, 2012.

Wong, P., Vecchio, F. and Trommels, H. 2013. *VECTOR2 & FORMWORKS USER'S MANUAL. Second Edition*, VecTor Analysis Group, Toronto, Ontario, Canada.

Wu, W. P. 1990. Thermomechanical Properties of Fiber Reinforced Plastic (FRP) Bars. PhD dissertation, West Virginia University, Morgantown, W.Va., 292 pp.

Xie, Y., Hill, C. A., Xiao, Z., Militz, H. and Mai, C. 2010. "Silane coupling agents used for natural fiber/polymer composites: a review," Composites Part A: Applied Science and Manufacturing, vol. 41, no. 7, pp. 806–819.

TUF-BAR. 2019. *Product technical specifications*, TUF-BAR INC, Edmonton, Alberta, Canada. https://www.tuf-bar.com/products/tuf-bar/ (2020)

https://www.vrodcanada.com/sites/default/files/pdfs-uploaded/Spec%20sheet%20CFRP%20-%20March%202011.pdf (2020)

Appendix 1: GFRP Rebars Tensile Strength

ASTM D7205 (ASTM International, 2016) describes the standard longitudinal tensile strength test method and elongation properties (ex. elastic modulus) of FRP bars. Unlike traditional steel, FRP bars have low shear strength which means that they cannot be gripped directly during testing without significantly damaging fibres. Therefore, FRP test specimens need to be prepared differently to account for this weakness. Anchors are used to attach the specimen to the testing machine to allow for the development of the full strength of FRP bars and for the specimens to fail away from the testing machine grips. This appendix details the testing procedure, preparation of specimens for tensile strength testing, and the tensile strength test results.

1. Load Frame

To determine the tensile strength and modulus of elasticity of GFRP rebars, an MTS load frame with a maximum capacity of 6100 kN was used. The MTS has a hydraulic power unit that controls an actuator through hydraulic pressure, and this actuator drives the grips that apply the load to the test specimens. An MTS controller was used to control the application of the load/displacement and a data acquisition system to collect raw data (load and stroke) from the MTS. To calculate strains values, an extensometer, comprised of a cable transducer, was used to measure localized displacement data. Figure A1.1a shows the MTS load frame, and Figure A1.1b shows a close-up of the test specimen.

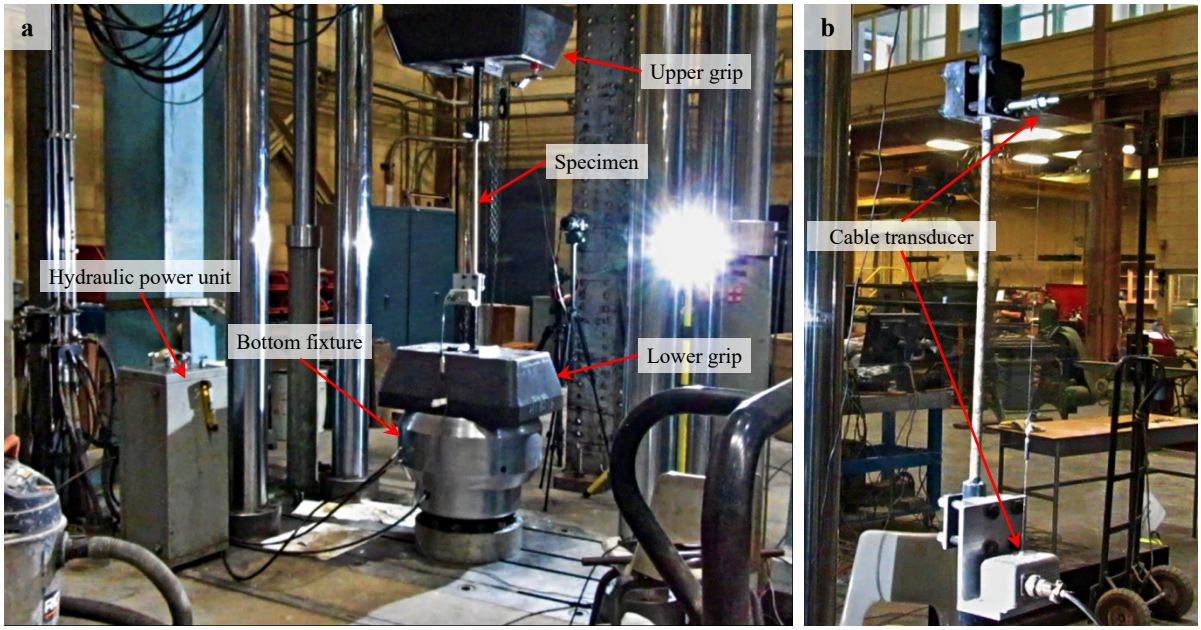

Figure A1.1: Bars testing set-up (a) MTS load frame (b) a close-up of the specimen.

2. Test Fixture for GFRP Tensile Test

The transverse strength of GFRP bars is much weaker than in the longitudinal one because of the orientation of fibres (i.e. almost all aligned longitudinally with the exception of helical wrapping on the bar exterior). To account for this anisotropic nature and to prevent transverse fibre damage induced by the clamping mechanism of the MTS machine, the GFRP bars are encased by anchors (steel tubes filled with expansive grout) at both ends of the tension test specimen, to facilitate gripping them, as shown in Figure 1.2a and Figure 1.2b. This allows for stress distribution over larger area and ultimately reduces the transverse forces on the specimens. The measurements of these tubes are mainly dependent on the rebar size and prescribed in ASTM D7205, which provides specifications on testing GFP bars for tensile properties. For example, for a #5 GFRP bar, steel tubes with an outer diameter of 42 mm, a wall thickness of 4.8 mm, and a minimal length (L_a) of 380 mm are required. The minimum free length between anchors must not be less than 380 mm or 40 times the effective bar diameter (40 x 15 = 600 mm). FRP bars have to be aligned properly through the anchors to prevent eccentric loading (ASTM International, 2016).

Figure A1.2: Anchored test specimen (a) photo (b) figure (ASTM International, 2016).

3. Tensile properties test procedure

After preparing the GFRP test specimens, the MTS machine was initialized, and its grips were aligned and adjusted to mount the test specimens. First, the lower end of the anchored test specimen was clamped with a pressure into the lower grip of the MTS machine. Afterwards, the upper grip of the MTS machine was adjusted to insert the upper end of the test specimen and then pressure was applied by the grip to clamp it. The MTS machine grips were adjusted to ensure the vertical alignment of the test specimen. An initial load was applied to the test specimen and then the extensometer was clamped on the GFRP bar in the middle of the free length of the test specimen. The loading was performed in a displacement control mode with a displacement rate that achieves a failure time between 60 seconds (1 min) and 600 seconds (10 min), as defined by ASTM D7205 (ASTM International, 2016). When the loading started, the force versus displacement data was continuously collected by the controlling computer. The tensile chord modulus of elasticity is calculated from the strain range of the lower half of the stress-strain curve with a starting point of

0.1% strain and an ending point 0.3% strain, according to ASTM D7205 (ASTM International, 2016).

4. Tensile properties results

The tensile behaviour of three GFRP rebar sizes was measured through a load cell, and a cable transducer. Five bars of each rebar size were tested to obtain average values and account for statistical variations in material properties, test preparations, and setup. The tensile behaviour of each rebar specimen was plotted in graphs that display the measured load along the vertical y-axis and the longitudinal strain on the x-axis. As per ASTM D7205 (ASTM International, 2016), the elastic moduli of the tested GFRP bars are calculated from the initial 0.3% of the strain range.

There are three possible modes of failure For GFRP rebar tested in tension: tensile rupture of the rebar, rebar slippage out of the anchor, and anchor slippage out of the testing machine grips. Rebar slippage and anchor slippage failure modes are due to inadequate preparation of specimens or deficient test machine setup. Rebar slippage may result from rebar-grout bond failure or rebar crushing inside the anchor due to high machine grip pressure. Anchor slippage, on the other hand, is caused by insufficient machine gripping pressure. The results from these two types of specimen failure do not represent actual material performance, and hence, they are not acceptable to be accurate. The only accepted results are the ones obtained from specimens that have failed in tensile rupture of rebars within their free length (L). These specimens show a clear brush-like failure pattern and fibres delamination along the free length of the specimen. The fibres of helical wraps on the rebar surface fail and delaminate significantly before the longitudinal fibres. Nevertheless, this early failure of the helical wrap fibres does not influence the load-displacement behaviour of rebars.

4.1. GFRP #3 Specimens results

Figure A1.3 shows the complete tensile stress-strain behaviour of five specimens of GFRP #3 bars (nominal area as reported by the manufacturer = 71 mm^2). Specimen G3-1 was tested under a slow displacement rate of 0.05 mm/min at first. Then, the displacement rate was increased during testing to 0.5 mm/min to achieve the 10 minutes testing time specified by ASTM D7205 (ASTM International, 2016); however, the test took longer than 10 minutes. This specimen had a kink at the junction of the anchor with the rebar at the top end which is indicative of poor bar alignment with the anchors. Hence, the specimen was slanted off the vertical axis when it was placed in the testing machine. This specimen failed prematurely because of the failure of fibres inside the

anchors due to grip-induced damage which has led to a pullout like failure. All in all, this specimen failed at a failure stress (1314 MPa) higher than the average ultimate tensile strength reported by the manufacturer (1000 MPa), and had a higher modulus of elasticity (68.7 GPa) than the minimum elastic modulus guaranteed by the manufacturer (49.1 GPa). The strain at the ultimate stress level was 2.34%.

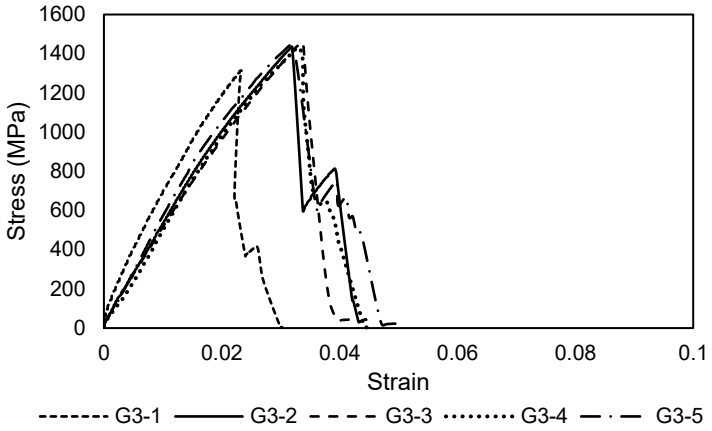

Figure A1.3: The tensile stress-strain behaviour of GFRP #3 specimens.

Specimen G3-2 was tested under a higher displacement rate of 1 mm/min. This test specimen was also slanted off axis due to anchor alignment issues. A similar mode of failure was observed where fibres inside the anchor were damaged due to high gripping pressure. The ultimate tensile strength, tensile chord modulus of elasticity, and strain at the ultimate tensile strength are reported in Table A1.1. This specimen achieved the guaranteed tensile strength and modulus of elasticity values reported by the manufacturer. High speed cameras were used to track failure modes of the bars specimens.

Table A1.1: Tensile properties test results of GFRP #3 bars

Specimen	Tensile strength, MPa	Tensile modulus of elasticity, GPa	Elongation at ultimate stress, %	Mode of failure[a]
G3-1	1314	68.7	2.34	RS
G3-2	1436	55.7	3.19	RS
G3-3	1458	49.5	3.38	RS
G3-4	1430	38.2	3.28	TR
G3-5	1453	49.6	3.19	RS

[a] TR = tensile rupture of the rebar, RS = rebar slippage out of the anchor

Specimens G3-3 through G3-5 were tested under a displacement rate of 2 mm/min. The increased displacement rate could affect the tensile strength and elastic modulus. All three specimens were slanted off axis due to anchor alignment issues. Nevertheless, they all achieved the minimum

tensile strength and elastic modulus guaranteed by the manufacturer except for one specimen, G3-4, which fell short from achieving the minimum guaranteed chord modulus of elasticity. Both specimens G3-3 and G3-5 failed due to fibre damage inside the anchors. However, specimen G3-4 failed in the free length between the anchors.

4.2. GFRP #4 Specimens results

The complete tensile stress-strain behaviour of five specimens of GFRP #4 bars (nominal area as reported by the manufacturer = 129 mm^2) is shown in Figure A1.4. The ultimate tensile strength and elastic modulus guaranteed by the manufacturer for these type of #4 GFRP bars were 850 MPa and 45.6 GPa, respectively. Specimens were tested under a displacement rate of 3 mm/min. All specimens were slanted off axis when they were positioned in the testing machine.

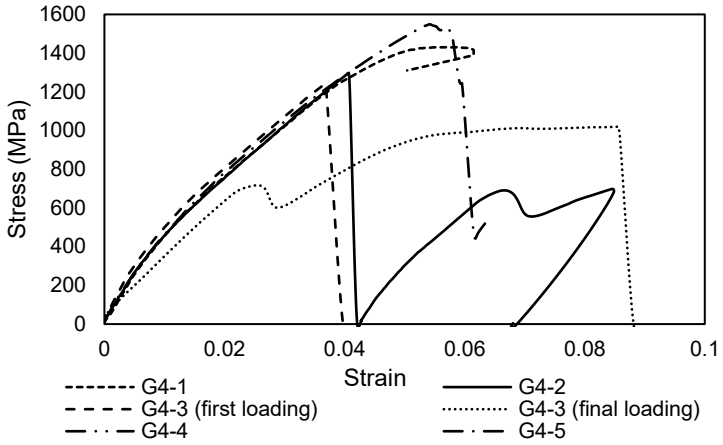

Figure A1.4: The tensile stress-strain behaviour of GFRP #4 specimens.

Specimen G4-1 was the only specimen from this set of GFRP #4 bars that failed in the free length between anchors. It achieved ultimate tensile strength and modulus of elasticity values higher than guaranteed by the manufacturer (Table A1.2).

Table A1.2: Tensile properties test results of GFRP #4 bars

Specimen	Tensile strength, MPa	Tensile modulus of elasticity, GPa	Elongation at ultimate stress, %	Mode of failure[a]
G4-1	1430	52.6	5.84	TR
G4-2	1298	48.7	4.07	RS
G4-3[b]	1242	58.3	3.68	RS
G4-3[c]	1020	32.5	8.56	RS
G4-4	14312	47.5	4.76	RS
G4-5	1549	50.8	5.42	RS

[a] TR = tensile rupture of the rebar, RS = rebar slippage out of the anchor
[b] Initial loading
[c] Final loading

Specimen G4-2 failed at a stress level higher than guaranteed by the manufacturer and had an elastic modulus above the minimum reported by the manufacturer. It failed due to rebar slippage caused by the high gripping pressure. So, the gripping pressure was reduced after reaching the ultimate stress to check if the anchors would slip out of the MTS. No anchor slippage was observed.

Specimen G4-3 was initially loaded with the reduced gripping pressure to avoid damaging the fibres in the anchored part, but to no effect. The test was stopped at a stress of 1200 MPa when the rebar started slipping out of the anchor, which was indicative of imminent rebar slippage failure. At that point, the specimen had already exceeded the minimum guaranteed tensile strength and tensile modulus of elasticity reported by the manufacturer. Then, the gripping pressure was reduced after unloading the specimen, and then it was reloaded to check if the anchors would slip out of the machine grip under the reduced pressure.

Specimens G4-4 and G4-5 failed at higher ultimate tensile stresses and with higher tensile moduli of elasticity than the minimum guaranteed values reported by the manufacturer.

4.3. GFRP #5 Specimens results

Figure A1.5 shows the complete tensile stress-strain behaviour of five specimens of GFRP #5 bars. The ultimate tensile strength and elastic modulus guaranteed by the manufacturer for this type of #5 GFRP rebars were 925 MPa and 48.8 GPa, respectively. Specimens were tested under a displacement rate of 3 mm/min. All specimens were slanted off axis when they were positioned in the testing machine.

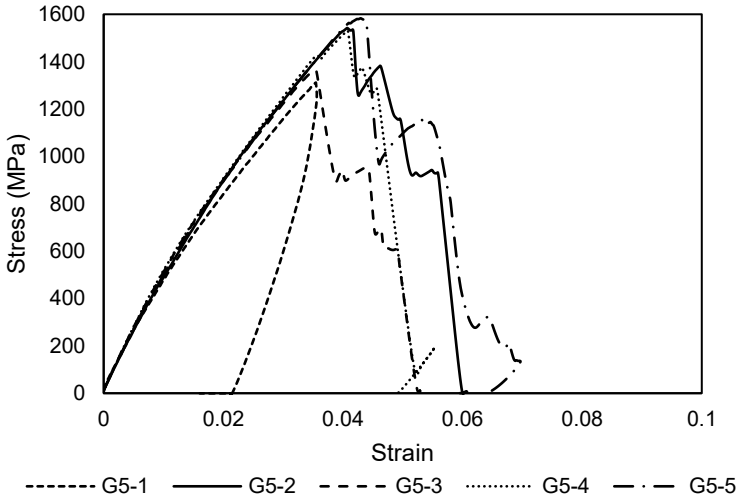

Figure A1.5: The tensile stress-strain behaviour of GFRP #5 specimens.

Specimens G5-1 and G5-5 failed due to fibre damage inside the anchors due to grip-induced damage which led to rebar slippage followed by buckling of the rebar. Nevertheless, both specimens achieved higher tensile strength with higher tensile moduli of elasticity than the minimum guaranteed values reported by the manufacturer, as shown in Table A1.3.

Table A1.3: Tensile properties test results of GFRP #5 bars

Specimen	Tensile strength, MPa	Tensile modulus of elasticity, GPa	Elongation at ultimate stress, %	Mode of failure[a]
G5-1	1312	75.5	3.55	RS
G5-2	1542	50.6	4.07	TR
G5-3	1365	54.3	3.54	TR
G5-4	1530	54.4	4.08	TR
G5-5	1583	51.8	4.3	RS

[a] TR = tensile rupture of the rebar, RS = rebar slippage out of the anchor

Failure of bars in the free length between the anchors was observed in specimens G5-2, G5-3, and G5-4. This mode of failure is more representative of the actual tensile properties of rebars, and the accepted mode of failure according to ASTM D7205 (ASTM International, 2016). Those specimens achieved the minimum guaranteed tensile strength and moduli of elasticity as reported by the manufacturer.

Appendix References

ASTM International 2016. Standard Test Method for Tensile Properties of Fiber Reinforced Polymer Matrix Composite Bars, (D7205). ASTM International, West Conshohocken, PA.